

**Measurement of the top quark mass using lepton  
transverse momenta with the ATLAS detector at  
 $\sqrt{s} = 8 \text{ TeV}$**



DISSERTATION DER FAKULTÄT FÜR PHYSIK  
DER  
LUDWIG-MAXIMILIANS-UNIVERSITÄT MÜNCHEN

VORGELEGT VON

**Michael Bender**

GEBOREN IN ROSENHEIM

MÜNCHEN, DEN 11.01.2017



Erstgutachter: Prof. Dr. Otmar Biebel  
Zweitgutachter: Prof. Dr. Thomas Kuhr  
Tag der mündlichen Prüfung: 06.03.2017



„Wo aber die Menschheit etwas Neues  
erkennt, will sie es benennen.“

*Stefan Zweig*

Amerigo



## Zusammenfassung

Aus Proton-Proton Kollisionen, die vom ATLAS Experiment bei 8 TeV Kollisionsenergie am LHC aufgezeichnet wurden, wird die Masse des top-Quarks im  $t\bar{t}$  Lepton+Jets Kanal bestimmt. Die erzeugten top-Quarkpaare zerfallen jeweils fast ausschließlich in ein bottom-Quark und ein  $W$ -Boson. Als Lepton+Jets Kanal wird hierbei derjenige Zerfall bezeichnet, bei dem eines der beiden  $W$ -Bosonen hadronisch und das andere leptonisch zerfällt. Im Gegensatz zu anderen Massebestimmungen wird in dieser Messung der transversale Impuls des Leptons zur Bestimmung der top-Quarkmasse verwendet. Hierbei gilt, je größer die Masse des top-Quarks, desto höher der transversale Impuls des Leptons aus dem Zerfall des zugehörigen  $W$ -Bosons. Aus der gemessenen Verteilung der Lepton-Impulse kann daher die top-Quarkmasse bestimmt werden. Die vorgestellte Methode, die erstmals auf 8 TeV ATLAS Daten angewendet wird, ergänzt hierbei andere Messungen auf Grund ihrer unterschiedlichen Sensitivität auf systematische Fehlerquellen. Um die top-Quarkmasse zu bestimmen, wird die Parametrisierung der Lepton-Transversalimpulse mittels MC Simulation kalibriert und auf die gemessenen Verteilungen in Daten angewendet. Die so bestimmte top-Quarkmasse ist  $m_{\text{top}} = 167.6 \pm 0.9 (\text{stat}) \pm 2.1 (\text{syst}) \text{ GeV}$ . Die Gesamtunsicherheit beträgt 2.4 GeV und resultiert aus der Untersuchung verschiedener Beiträge.

Da die Messung auf Grund Ihrer Abhängigkeit von der Modellierung des transversalen top-Quarkimpulses sensitiv auf Korrekturen höherer Ordnung ist, wird der Einfluss solcher Korrekturen durch die Umgewichtung der NLO MC Vorhersage auf NNLO Berechnungen abgeschätzt. Diese Umgewichtung führt zu einer Verschiebung der gemessenen top-Quarkmasse um  $-1.0 \pm 0.5 \text{ GeV}$  und zeigt somit, dass Korrekturen höherer Ordnung einen signifikanten Einfluss auf die aus den transversalen Leptonimpulsen gemessene top-Quarkmasse haben.



## Abstract

The mass of the top quark is determined in proton-proton collisions at a centre-of-mass energy of 8 TeV, recorded by the ATLAS experiment at the LHC. For the measurement,  $t\bar{t}$  events with lepton+jets final states are used. A top quark decays almost exclusively in a bottom quark and a  $W$  boson, therefore the lepton+jets channel represents the decay in which one  $W$  boson decays hadronically and the other one leptonically. In contrast to other measurements, this analysis is designed to exploit the dependence of the lepton kinematics on the top quark mass, by parameterising the lepton's transverse momentum distribution with MC simulations. Applied for the first time on 8 TeV ATLAS data, this method can complement other  $m_{\text{top}}$  measurements, because of its different sensitivity to systematic uncertainties. With this approach, the top quark mass is measured to be  $167.6 \pm 0.9$  (stat)  $\pm 2.1$  (syst) GeV. The total uncertainty of 2.4 GeV results from a careful evaluation of various systematic sources.

Since the result depends on the modelling of the top quark transverse momentum, it is sensitive to higher order corrections. The influence of such corrections is estimated by reweighting the NLO MC prediction to NNLO calculations. This results in a shift in the measured top quark mass of  $-1.0 \pm 0.5$  GeV and therefore shows that higher order corrections can have a significant influence in the determination of  $m_{\text{top}}$  with the lepton  $p_T$ .



# Contents

<b>1</b>	<b>Introduction</b>	<b>1</b>
<b>2</b>	<b>Theory</b>	<b>3</b>
2.1	The Standard Model	3
2.1.1	Gauge invariance and renormalisation	5
2.1.2	Quantum chromodynamics	7
2.1.3	The electroweak theory	9
2.2	The top quark	12
2.2.1	The CKM matrix	12
2.2.2	The parton distribution function	13
2.2.3	Top quark production	13
2.2.4	Top quark decay	18
2.2.5	The top quark mass	20
<b>3</b>	<b>Experimental setup</b>	<b>21</b>
3.1	The LHC accelerator	21
3.2	The ATLAS experiment	23
3.2.1	The ATLAS coordinate system	23
3.2.2	The magnet system	24
3.2.3	The inner detector	24
3.2.4	The calorimeter system	26
3.2.5	The muon spectrometer	27
3.2.6	Data processing	28
3.3	Top quark production at LHC	29
3.4	Monte Carlo event generation	30
<b>4</b>	<b>Data and Monte Carlo Samples</b>	<b>33</b>
<b>5</b>	<b>Event reconstruction and selection</b>	<b>35</b>
5.1	Physics objects	35
5.2	Event selection	37
5.3	Data and MC distributions	38
<b>6</b>	<b>Template fit</b>	<b>45</b>
<b>7</b>	<b>Uncertainty estimation</b>	<b>51</b>
7.1	Statistics and method calibration	51
7.2	Modelling uncertainties	53

7.3	Non $t\bar{t}$ contributions	54
7.4	Detector modelling	54
<b>8</b>	<b>Modelling of the transverse momentum of the top quark</b>	<b>57</b>
<b>9</b>	<b>Results</b>	<b>59</b>
<b>10</b>	<b>Conclusion</b>	<b>61</b>
<b>A</b>	<b>List of data and MC datasets</b>	<b>63</b>
<b>B</b>	<b>Data and MC distributions for <math>m_{\text{top}} = 167.5</math> GeV</b>	<b>67</b>
<b>C</b>	<b>Additional information concerning the template fit</b>	<b>71</b>
<b>D</b>	<b>Split-up of lepton and jet related uncertainties</b>	<b>79</b>
<b>E</b>	<b>Influence of cuts on <math>\Delta R_{jj}</math> and the jet multiplicity on the uncertainties</b>	<b>81</b>
<b>F</b>	<b>Top quark transverse momentum reweighting</b>	<b>83</b>
<b>G</b>	<b>Investigations due to the comparatively small top quark mass value</b>	<b>85</b>
	<b>Bibliography</b>	<b>93</b>
	<b>List of Figures</b>	<b>93</b>
	<b>List of Tables</b>	<b>95</b>
	<b>Acknowledgement</b>	<b>97</b>

# 1. Introduction

Modern physics is built on two main theories. On the one hand there is the theory of general relativity [1], which is extremely successful in describing large scale phenomena in the universe. Its latest success was the confirmation of the existence of gravitational waves [2], exactly 100 years after its theoretical prediction. On the other hand, there is the theory of the Standard Model of Particle Physics, which describes the smallest scales, namely the interaction of fundamental particles, remarkably well. In contrast to general relativity, which has been devised by a single person, the Standard Model is the creation of many physicists. Its foundations were laid in the 1960's and 1970's with the pioneering works covering quantum chromodynamics and the electroweak theory. Within the Standard Model the top quark is the heaviest fundamental particle known. Its existence has been predicted already in 1972 by Kobayashi and Maskawa [3], but it took over 20 years until it was finally discovered by the Tevatron experiments CDF and DØ in 1995 [4, 5]. Since then, its characteristics have been studied in great detail, also by the LHC experiments ATLAS and CMS. A top quark property of particular interest is its mass  $m_{\text{top}}$ . As the top quark mass is a free parameter of the Standard Model, the precise determination of  $m_{\text{top}}$  is crucial for consistency checks [6] and may play an essential role e.g. in deciding on vacuum stability [7].

ATLAS and CMS have presented highly accurate measurements of  $m_{\text{top}}$  in different decay topologies (cf. [8–12]), with the most precise results obtained in the  $t\bar{t}$  lepton+jets channel<sup>(1)</sup>. In this channel one of the  $W$  bosons, originating from the  $t\bar{t}$  system, decays into a lepton and neutrino, while the other  $W$  boson decays hadronically. In addition to the separate measurements by each experiment, a combination of measurements of all four experiments, ATLAS, CDF, CMS and DØ was performed, resulting in a top quark mass of  $m_{\text{top}} = 173.34 \pm 0.27$  (stat)  $\pm 0.71$  (syst) GeV<sup>(2)</sup> [14]. Complementary to Ref. [8–12], the analysis presented in this thesis adopts an approach originally used in Ref. [15] to determine the top quark mass. Instead of studying an observable which is directly related to the invariant mass of the reconstructed top quark, the mass is inferred from the lepton transverse momentum. Due to energy and momentum conservation the mass of the top quark translates into high momenta of its decay products. Therefore, in the lepton+jets channel, the information of the top quark mass is imprinted on the transverse momentum of the lepton. This complementary approach with its different sensitivity to systematic uncertainties, may help to further increase the precision on the top quark mass in future combinations. This analysis uses proton-proton collisions recorded at a centre-of-mass energy of 8 TeV with the ATLAS detector in 2012. Final states with  $t\bar{t}$  lepton+jets characteristics are selected, in order to extract  $m_{\text{top}}$  from the lepton  $p_{\text{T}}$  distribution with a template technique.

---

<sup>(1)</sup>An overview of recent top quark mass measurements performed by the ATLAS experiment is given in Ref. [13].

<sup>(2)</sup>In this theses, natural units, with  $c = 1$  and  $\hbar = 1$ , are used. Therefore energies, momenta and masses are measured in GeV.



## 2. Theory

This chapter summarises the basic ideas of the Standard Model of particle physics (SM) and briefly describes the field of top quark physics within this theory.

### 2.1. The Standard Model

The Standard Model of Particle Physics is the cornerstone of present-day high energy physics. It was developed mainly in the 1960s and 1970s and since then, it has been extremely successful in describing fundamental particles and their interactions. Despite its limitations, like the inability of describing the force of gravity or the lack of insight in the origin of the asymmetry between matter and anti-matter, the Standard Model has, within the field of particle physics, met every experimental test to highest precision. In addition, it has predicted unknown characteristics of nature, which by now have all been experimentally verified. Its maybe greatest success was the discovery of the Higgs boson by the LHC experiments ATLAS and CMS [16, 17], which had been theoretically predicted half a century ago. According to the Standard Model, elementary particles are grouped in two categories: particles with half-integer spin, so-called fermions, which are the fundamental building blocks of matter and particles with integer spin named gauge bosons, which mediate the fundamental forces. The interactions described by the Standard Model, are the electromagnetic, the weak and the strong force. The electromagnetic force is mediated by the photon ( $\gamma$ ) and is the source of electricity and magnetism. The weak interaction is accountable for radioactive  $\beta$  decays and is carried by the  $W$  and  $Z$  bosons. The strong force is mediated by gluons ( $g$ ) and is responsible for the binding of protons and neutrons inside the nucleus. Within the Standard Model, the fermions can be split in two categories, particles, which interact with gluons, named quarks, and particles, which do not participate in the strong force, so-called leptons. A striking characteristic of the Standard Model is its periodic structure, which means that fermions can be sorted in generations. A total of three generations exist and each generation consists of an up- and down-type quark, a lepton and the corresponding lepton neutrino. An overview of the particle content of the Standard Model is given in Table 2.1.

The Standard Model is formulated in terms of a quantum field theory. In classical mechanics the dynamics of a system can be described by its Lagrangian  $L$ , which is a function of coordinates and velocities, by solving the Euler Lagrange equation. In quantum field theories, however, the system no longer comprises discrete particles but fields, therefore the Lagrangian is replaced by a Lagrangian density  $\mathcal{L}$

$$L = \int \mathcal{L}(\Phi, \partial_\mu \Phi, x^\mu) \cdot d^3x \quad (2.1)$$

which is now described by fields  $\Phi$ , their derivatives  $\partial_\mu \Phi$  and the space-time coordinates  $x^\mu$ . The Euler-Lagrange equation can then be written as

$$\partial_\mu \left( \frac{\partial \mathcal{L}}{\partial (\partial_\mu \Phi)} \right) - \frac{\partial \mathcal{L}}{\partial \Phi} = 0 \quad (2.2)$$

<b>Fermions</b>					
First generation	Name	Symbol	Colour	Charge [e]	Mass [MeV]
	Up quark	$u$	yes	$+2/3$	$2.3^{+0.7}_{-0.5}$
	Down quark	$d$	yes	$-1/3$	$4.8^{+0.5}_{-0.3}$
	Electron	$e$	no	-1	0.511
	Electron neutrino	$\nu_e$	no	0	$< 0.002$
Second generation	Name	Symbol	Colour	Charge [e]	Mass [MeV]
	Charm quark	$c$	yes	$+2/3$	$1275 \pm 25$
	Strange quark	$s$	yes	$-1/3$	$95 \pm 5$
	Muon	$\mu$	no	-1	105.7
	Muon neutrino	$\nu_\mu$	no	0	$< 0.19$
Third generation	Name	Symbol	Colour	Charge [e]	Mass [GeV]
	Top quark	$t$	yes	$+2/3$	$173.21 \pm 0.87$
	Bottom quark	$b$	yes	$-1/3$	$4.18 \pm 0.03$
	Tau	$\tau$	no	-1	1.78
	Tau neutrino	$\nu_\tau$	no	0	$< 0.02$
<b>Bosons</b>					
Name	Force mediated	Symbol	Colour	Charge [e]	Mass [GeV]
Photon	electromagnetic	$\gamma$	no	0	0 (theory)
Gluon	strong	$g$	yes	0	0 (theory)
$W^\pm$ boson	weak	$W^\pm$	no	$\pm 1$	$80.385 \pm 0.015$
$Z$ boson	weak	$Z$	no	0	$91.188 \pm 0.002$
Higgs boson	Higgs field	$H$	no	0	$125.7 \pm 0.4$

Table 2.1.: The fundamental particles of the Standard Model. For each particle also an anti-particle with opposite charge-like quantum numbers exists. The stated mass values are taken from Ref. [18]. In cases where no uncertainty on the measured mass is quoted, the experimental uncertainty is more precise than the number of significant digits given in the table. The upper limits from direct observation for the electron- and tau neutrino masses are given at 95% CL, while the limit on the muon neutrino mass is given at 90% CL.

The complete Lagrangian of the Standard Model  $\mathcal{L}_{\text{SM}}$  consists of three parts

$$\mathcal{L}_{\text{SM}} = \mathcal{L}_{\text{QCD}} + \mathcal{L}_{\text{EW}} + \mathcal{L}_{\text{Higgs}} \quad (2.3)$$

where  $\mathcal{L}_{\text{QCD}}$  describes quantum chromodynamics (QCD), the theory of the strong force and  $\mathcal{L}_{\text{EW}}$  represents the electroweak theory, the theoretical foundation of the electromagnetic and weak forces. The last term  $\mathcal{L}_{\text{Higgs}}$  is connected to the Higgs-mechanism, which is responsible for electroweak symmetry breaking, which in turn gives rise to particle masses.

(This section is based on Ref. [19, 20].)

### 2.1.1. Gauge invariance and renormalisation

The basic principles of quantum field theories are gauge invariance and renormalisability. Gauge invariance denotes the fact, that physics processes, therefore the underlying equations, should not change under a given transformation. This can be illustrated easiest in the case of quantum electrodynamics (QED), the theory describing electromagnetic interactions. To outline the principle of gauge invariance one can begin with the Dirac Lagrangian, which is given by

$$\mathcal{L}_{\text{Dirac}} = i\bar{\psi}\not{\partial}\psi - m\bar{\psi}\psi(x) \quad (2.4)$$

where the Feynman slash notation is used<sup>(1)</sup>. Inserting equation 2.4 in 2.2 yields the Dirac equation

$$(i\not{\partial} - m)\psi(x) = 0 \quad (2.5)$$

describing the motion of a spin  $\frac{1}{2}$  particle, like an electron, with mass  $m$ . The Dirac equation is invariant under global gauge transformations<sup>(2)</sup> which can be written as

$$\psi(x) \rightarrow \psi'(x) = e^{i\alpha}\psi(x) \quad (2.6)$$

where  $\alpha$  is a real number. Since the Dirac equation is invariant under such a transformation, the physical results are unchanged. However, Eq. 2.5 is not invariant under a local gauge transformation

$$\psi(x) \rightarrow \psi'(x) = e^{i\alpha(x)}\psi(x) \quad (2.7)$$

where  $\alpha$  is a function of space-time. This can be seen by explicitly inserting  $\psi'$  in the Dirac equation

$$\begin{aligned} (i\not{\partial} - m)\psi'(x) &= (i\not{\partial} - m)e^{i\alpha(x)}\psi(x) \\ &= e^{i\alpha(x)}((i\not{\partial} - m)\psi(x) - \partial^\mu\alpha(x)\gamma_\mu\psi(x)) \end{aligned} \quad (2.8)$$

Since  $\partial^\mu\alpha(x)\gamma_\mu\psi(x) \neq 0$ , the invariance of Eq. 2.5 is spoiled by local gauge transformations. To restore the invariance of the Dirac equation, the derivative  $\partial^\mu$  has to be replaced by the covariant derivative  $D_\mu$

$$\partial^\mu \rightarrow D_\mu = \partial_\mu + ieA_\mu(x) \quad (2.9)$$

<sup>(1)</sup>Where  $\not{\partial} = \gamma^\mu\partial_\mu$ ,  $\gamma^\mu$  denote the Dirac matrices and the Einstein summation convention is applied.

<sup>(2)</sup>In case of quantum electrodynamics gauge transformations are described by  $U(1)_q$ .  $U(1)_q$  is part of the unitarity group  $U(n)$ , where  $U(n)$  describes the set of  $n \times n$  dimensional matrices which satisfy  $U^\dagger U = 1$ . The subscript denotes the conserved quantity, which in this case is the electric charge  $q$ . One possible representation is  $U(\alpha) = e^{-i\alpha G}$ , where  $G$  is called the generator of the group.

## 2. Theory

---

The newly introduced vector gauge field  $A_\mu(x)$  corresponds to the photon, the mediator of the electromagnetic interaction and transforms like

$$A^\mu(x) \rightarrow A'^\mu(x) = A^\mu(x) + \frac{1}{e} \partial_\mu \alpha(x) \quad (2.10)$$

Therefore the Dirac equation becomes invariant under local gauge transformations by replacing the derivative  $\partial^\mu$  with  $D_\mu$ . If in addition a kinetic term for the photon is added to the equation, one obtains the gauge invariant Lagrangian of quantum electrodynamics

$$\mathcal{L}_{\text{QED}} = \bar{\psi} (i\cancel{\partial} - m) \psi + e \bar{\psi} A_\mu \psi - \frac{1}{4} F_{\mu\nu} F^{\mu\nu} \quad (2.11)$$

in which the first term, as already in Eq. 2.5, describes the free motion of a spin  $\frac{1}{2}$  particle with mass  $m$ , the second term represents the interaction of such a particle with a photon and the last term, with the field strength tensor

$$F_{\mu\nu} = \partial_\mu A_\nu - \partial_\nu A_\mu \quad (2.12)$$

is the kinetic term of the photon field. Since an additional photon mass term, which would look like  $\frac{1}{2} m_\gamma^2 A_\mu A^\mu$ , would again spoil the gauge invariance of Eq. 2.11, it immediately follows that  $m_\gamma = 0$ . Therefore the condition of gauge invariance in QED dictates that the photon has to be massless, which agrees well with the measured upper limit of  $m_\gamma < 1 \cdot 10^{-18}$  eV [18]. The demand for massless force carriers is in fact a crucial prerequisite for gauge invariance, which will also be seen in quantum chromodynamics and especially in the context of the electroweak theory. Ultimately the requirement of gauge invariance leads to the Brout-Englert-Higgs mechanism, which in turn gives rise to the existence of the Higgs boson. But why should one care for gauge invariance within the Standard Model in the first place? It has been shown, that gauge invariance is an essential precondition for renormalisability [21]. Renormalisability means that divergent terms, occurring in theoretical calculation of physical observables, can be absorbed in finite measurable quantities. This can be illustrated with the electron-electron scattering process, again an example from quantum electrodynamics. Calculating the leading order process, which is shown in the Feynman diagram in Fig. 2.1(a), works fine, but the result is only an approximation. To receive an exact result, also higher order corrections have to be included, for example the vacuum polarisation, which is presented in Fig. 2.1(b). When calculating the cross section for this process something interesting happens: one picks up a divergent term which essentially looks like

$$\int_{m^2}^{\infty} \frac{1}{z} dz \quad (2.13)$$

where  $z$  is the square of the virtual particle's momentum. Therefore the cross section for this process becomes infinite, obviously contradicting experimental results. To mask the divergence, one can introduce an upper cut-off value  $M^2$ , which in a later step is sent to infinity. With this, Eq. 2.13 becomes

$$\int_{m^2}^{M^2} \frac{1}{z} dz = \ln \left( \frac{M^2}{m^2} \right) \quad (2.14)$$

The important point of renormalisation is, that this term, which also diverges, is absorbed in physical quantities, as for this example, in the electron charge. Thus, the basic statement of renormalisation in this example is, that the electron charge as it is measured in experiment, is not the same as the charge which enters the theory calculations. It is distinguished between a bare charge  $e_0$ , which is used in

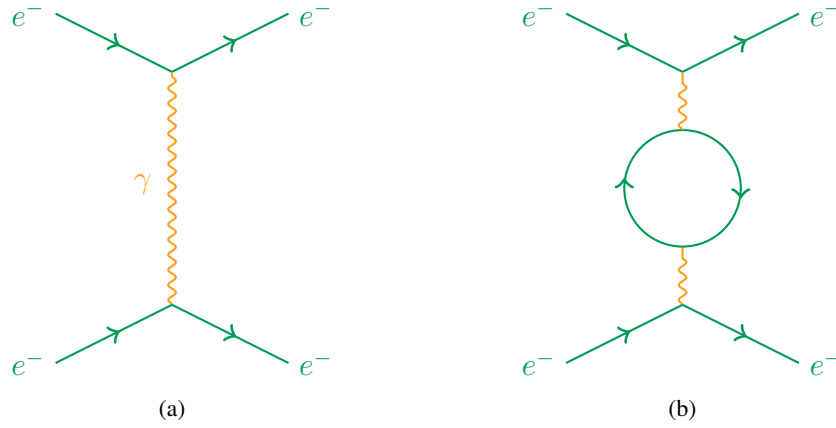


Figure 2.1.: Electron-electron scattering via the exchange of a virtual photon. The leading order process is shown in Fig. (a), a higher order correction, in which a virtual photon splits up into an electron positron pair which annihilates again, is shown in Fig. (b)

theory calculations and a renormalised charge  $e$  measured in experiment. The relation between those two is then given by

$$e \equiv e_0 \left( 1 - \frac{e_0^2}{12\pi^2} \ln \left( \frac{M^2}{m^2} \right) \right)^{\frac{1}{2}} \quad (2.15)$$

With this, the infinity of Eq. 2.13 is now absorbed in  $e$ . Since the charge measured in experiment is obviously finite, the divergence in  $\ln \left( \frac{M^2}{m^2} \right)$  has to be cancelled by a corresponding divergence in the bare charge  $e_0$ . A direct consequence of this is the energy dependence of coupling constants. In leading order, the coupling constant in QED  $\alpha$  can be written as

$$\alpha(Q^2) = \frac{e^2(Q^2)}{4\pi} = \frac{\alpha(\mu^2)}{1 - \frac{\alpha(\mu^2)}{3\pi} \ln \left( \frac{Q^2}{\mu^2} \right)} \quad (2.16)$$

in which  $Q$  denotes the momentum scale of the process and  $\mu$  is a reference renormalisation scale, closely related to the cut-off value  $M^2$ . The experimental results, shown in Fig.2.2(a), indeed proof that the coupling constant of QED, as described by Eq. 2.16, increases with larger momentum transfer. (For this section Ref. [19, 22–25] have been used.)

## 2.1.2. Quantum chromodynamics

Quantum chromodynamics is the theoretical framework of the strong force. It describes the interactions between particles with colour charge, namely quarks and gluons. In total, there are three colour charges, red, green and blue, which can be considered as axes in an abstract internal space. Since there is no distinguished colour, or in other words no distinguished axis in colour space, transformations between colours, corresponding to rotations in colour space, represent a symmetry, which is described by the  $SU(3)_C$  symmetry group.<sup>(3)</sup> In quantum chromodynamics, the force mediators are represented

<sup>(3)</sup>The special unitarity group  $SU(N)$  is a subgroup of  $U(N)$ , which in addition fulfils  $|U| = 1$ . QCD is described by the three dimensional representation  $SU(3)$ , with the colour charge  $C$  as conserved quantity.  $SU(N)$  groups have a total of  $N^2 - 1$  generators, which for  $SU(3)$  form the gluons and can be expressed in terms of the Gell-Mann matrices  $\lambda_\alpha$ .

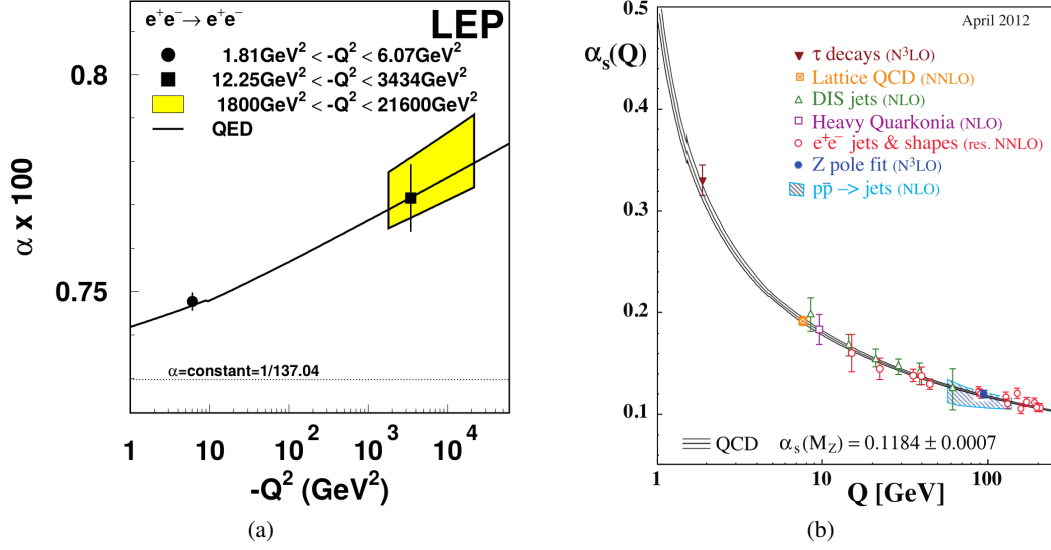


Figure 2.2.: Running of the coupling constants for the electromagnetic and strong forces as obtained from experiment [26, 27]. Figure (a) shows the energy dependence of  $\alpha$ , while Fig. (b) presents the result for  $\alpha_s$ .

by eight bicoloured gauge fields  $G_\mu^\alpha$ , which correspond to the gluons. The Lagrangian of quantum chromodynamics can be written as

$$\mathcal{L}_{\text{QCD}} = -\frac{1}{4} \mathbf{G}_{\mu\nu} \mathbf{G}^{\mu\nu} + \sum_k \bar{q}_k (i\not{D} - m_k) q_k \quad (2.17)$$

where  $\mathbf{G}_{\mu\nu}$  represents the gluon field strength tensor and  $q_k$  denotes the different quark flavours. The covariant derivative is given by

$$D_\mu = \partial_\mu + ig_s \frac{\lambda}{2} \mathbf{G}_\mu \quad (2.18)$$

in which  $g_s$  is the strong coupling and  $\lambda$  and  $\mathbf{G}$  are vectors of the Gell-Mann matrices  $\lambda_\alpha$  and gauge fields, respectively. The field strength tensor is

$$\mathbf{G}_{\mu\nu} = \partial_\mu \mathbf{G}_\nu - \partial_\nu \mathbf{G}_\mu - g_s \mathbf{G}_\mu \times \mathbf{G}_\nu \quad (2.19)$$

and looks similar to  $F_{\mu\nu}$  (cf. Eq. 2.12) except for the additional cross product. This term is a characteristic feature of quantum field theories based on non-abelian gauge groups, which represents the fact that the gauge bosons carry colour themselves and therefore interact with each other. The Feynman diagrams of such self interactions are shown in Fig 2.3. The fact that gluons carry colour impacts also the QCD coupling constant  $\alpha_s$ , which in leading order is given by

$$\alpha_s(Q^2) = \frac{g_s^2}{4\pi} = \frac{\alpha_s(\mu^2)}{1 + \frac{\alpha_s(\mu^2)}{12\pi} (33 - 2n_f) \ln\left(\frac{Q^2}{\mu^2}\right)} \quad (2.20)$$

where  $n_f$  is the number of quark flavours able to participate in a certain interaction. The overall plus sign in front of the logarithm (compared to the overall minus in Eq. 2.16) follows from the gluon self interactions. Therefore, opposite to the coupling constant of quantum electrodynamics  $\alpha$ ,  $\alpha_s$  decreases

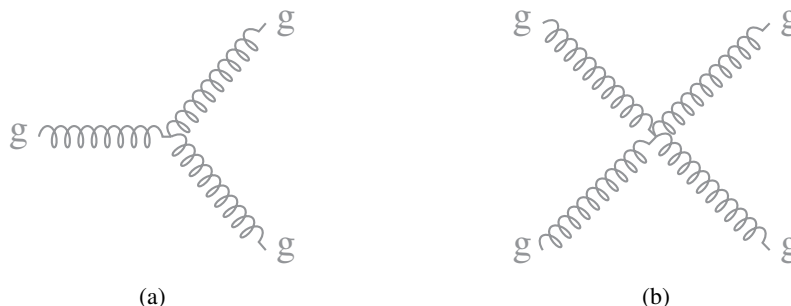


Figure 2.3.: Gluon self coupling vertices due to the non-abelian structure of quantum chromodynamics.

with increasing momentum transfer  $Q$ , which is shown in Fig. 2.2(b). This behaviour gives rise to the phenomena of asymptotic freedom and confinement. Asymptotic freedom describes the behaviour of quarks at very small distances, which correspond to very high energies. In this regime quarks behave as quasi-free particles, because the coupling constant  $\alpha_s$  becomes increasingly small. On the other hand, for large distances, corresponding to small energies, the coupling constant increases. This causes the phenomena of confinement, which means that quarks can not exist as free particles, but are bound into colourless objects, so-called hadrons. Hadrons are usually divided into two groups<sup>(4)</sup>, mesons and baryons. Mesons are a combination of a quark and an anti-quark, where the colour of the quark compensates the anti-colour of the anti-quark. The baryon consists either of three quarks or three anti-quarks, where each of the (anti-)quarks carries a different (anti-)colour. Since colour is an additive quantum number, both, mesons and baryons are uncoloured objects. The process of forming hadrons from quarks is referred to as hadronisation and is, because of the low energy scales involved, theoretically challenging. Due to confinement, only so-called jets, consisting of a shower of uncoloured particles formed during the hadronisation process, instead of single quarks, can be observed in an experiment.

(References for this section are [19, 22–25].)

### 2.1.3. The electroweak theory

Within the theory of the Standard Model it can be shown that both the electromagnetic and the weak interactions, although appearing to be separate forces, are a low energy representation of a single interaction. This interaction is described by the electroweak theory (EW). It is based on the  $SU(2)_L \times U(1)_Y$  gauge group and has a total of four different gauge fields. Three of them, the  $W_\mu^1$ ,  $W_\mu^2$  and  $W_\mu^3$ , belong to  $SU(2)_L$  and couple to the weak isospin<sup>(5)</sup>, while the fourth field, the  $B_\mu$  is associated with  $U(1)_Y$  and couples to the weak hypercharge

$$Y = 2(Q - I_3) \quad (2.21)$$

<sup>(4)</sup>A recent measurement [28] has revealed the existence of a more exotic state of five quarks ( $uudc\bar{c}$ ), a so-called pentaquark.

<sup>(5)</sup>Only left handed fermions and right handed anti-fermions carry a weak isospin unequal zero. Therefore the gauge bosons of  $SU(2)_L$  couple only to left handed particles and right handed anti-particles, which is known as parity violation.

## 2. Theory

---

where  $Q$  denotes the electrical charge and  $I_3$  is the third component of the weak isospin. The Lagrangian of the electroweak interaction is given by

$$\mathcal{L}_{\text{EW}} = \sum_k i\bar{\psi}_k \not{D}_\mu \psi_k - \frac{1}{4} \mathbf{W}_{\mu\nu} \mathbf{W}^{\mu\nu} - \frac{1}{4} B_{\mu\nu} B^{\mu\nu} \quad (2.22)$$

where the  $\psi_k$  denote the different quark and lepton flavours. The covariant derivative of the electroweak interaction (for left handed particles<sup>(6)</sup>) reads

$$D_\mu = \partial_\mu + \frac{1}{2} ig\boldsymbol{\tau} \mathbf{W}_\mu + \frac{1}{2} ig'Y B_\mu \quad (2.23)$$

where  $g$  and  $g'$  denote the couplings of  $SU(2)_L$  and  $U(1)_Y$ , while  $\boldsymbol{\tau}$  and  $\mathbf{W}_\mu$  are three component vectors, comprising of the pauli matrices and the gauge fields  $W_\mu^\alpha$ , respectively. The field strength tensors of the electroweak theory are given by

$$B_{\mu\nu} = \partial_\mu B_\nu - \partial_\nu B_\mu \quad (2.24)$$

$$\mathbf{W}_{\mu\nu} = \partial_\mu \mathbf{W}_\nu - \partial_\nu \mathbf{W}_\mu - g \mathbf{W}_\mu \times \mathbf{W}_\nu \quad (2.25)$$

In contrast to  $U(1)_Y$ ,  $SU(2)_L$  is a non-abelian group, therefore Eq. 2.25 includes a self interaction term similar to the one of QCD (cf. Eq. 2.19). In order to preserve the gauge invariance of Eq. 2.22, the gauge bosons of the electroweak interaction have to have zero mass. But as experiments have shown, only the photon is massless, while the  $Z$  and  $W^\pm$  bosons are massive (cf. Table 2.1). To meet the experimental results and to satisfy the principle of gauge invariance, the electroweak symmetry has to be broken. Within the Standard Model, this symmetry breaking is described by the Brout-Englert-Higgs mechanism [29, 30]. This mechanism adds a new scalar field

$$\Phi = \frac{1}{\sqrt{2}} \begin{pmatrix} \phi^+ \\ \phi^0 \end{pmatrix} \quad (2.26)$$

to the electroweak Lagrangian. The additional terms in the Lagrangian read

$$\mathcal{L}_{\text{Higgs}} = (D_\mu \Phi)^\dagger (D^\mu \Phi) - V(\Phi) \quad (2.27)$$

where the potential  $V$  is given by

$$V(\Phi) = \mu^2 \Phi^\dagger \Phi + \lambda (\Phi^\dagger \Phi)^2 \quad (2.28)$$

with  $\lambda$  being a positive real number. The minima of this potential depend on the choice of the parameter  $\mu^2$ , as can be seen in Fig. 2.4. If  $\mu^2$  is set to a value larger than zero, the only minimum is at  $\Phi = 0$ . However, if  $\mu^2 < 0$  is chosen, the minima of the potential are

$$\Phi_{\text{min}} = \pm \sqrt{\frac{-\mu^2}{\lambda}} \equiv \pm \nu \quad (2.29)$$

where  $\nu$  is called the vacuum expectation value of the Higgs field. By choosing one of the minima  $\Phi_{\text{min}}$ , the original symmetry of the potential is broken. This is referred to as spontaneous symmetry breaking, which means that an underlying symmetry is spoiled by the selection of a particular ground

<sup>(6)</sup>The covariant derivative for right handed particles is  $D_\mu = \partial_\mu + \frac{1}{2} ig'Y B_\mu$ .

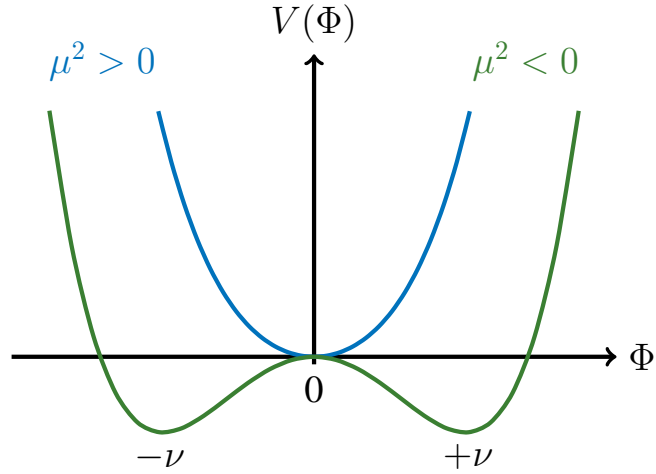


Figure 2.4.: The potential  $V(\Phi)$  plotted for an one-dimensional scalar field  $\Phi$ , for both cases,  $\mu^2 > 0$  and  $\mu^2 < 0$ .

state. Expanding the potential around the ground state and rewriting the terms in the Lagrangian results in the physical mass eigenstates of the gauge bosons. By using the Weinberg angle

$$\theta_W = \tan^{-1} \left( \frac{g'}{g} \right) \quad (2.30)$$

the electroweak gauge bosons, and their acquired masses, can be expressed in terms of the electroweak gauge fields as

$$A_\mu = \sin \theta_W W_\mu^3 + \cos \theta_W B_\mu \quad \text{with} \quad m_\gamma = 0 \quad (2.31)$$

$$W_\mu^\pm = \frac{1}{\sqrt{2}} (W_\mu^1 \mp iW_\mu^2) \quad \text{with} \quad m_{W^\pm} = \frac{g\nu}{2} \quad (2.32)$$

$$Z_\mu = \cos \theta_W W_\mu^3 - \sin \theta_W B_\mu \quad \text{with} \quad m_Z = \frac{m_{W^\pm}}{\cos \theta_W} \quad (2.33)$$

This means that two gauge fields of  $SU(2)_L$ , the  $W_\mu^1$  and  $W_\mu^2$ , are absorbed in the  $W^\pm$  bosons, while the photon and  $Z$  boson are superpositions of the  $W_\mu^3$  and the gauge field of the  $U(1)_Y$  gauge group  $B_\mu$ . By introducing the Higgs mechanism, not only do the gauge bosons gain their mass, but one can also account for quark and lepton masses by expanding the Higgs Lagrangian with an additional mass term for fermions

$$\tilde{g}_f \left( \bar{\Psi}_L^f \Phi \Psi_R^f + \bar{\Psi}_L^f \Phi^\dagger \Psi_R^f \right) \quad (2.34)$$

where  $\Psi$  denote the left and right handed Dirac spinors of a fermion  $f$  and  $\tilde{g}_f$  is its corresponding Yukawa coupling. Thus the mass of an elementary fermion

$$m_f = \tilde{g}_f \frac{\nu}{\sqrt{2}} \quad (2.35)$$

is defined by its Yukawa coupling to the Higgs field. The insertion of an additional field to the electroweak Lagrangian can therefore account for the masses of the gauge bosons, quarks and leptons. Furthermore, the additional field introduces a new particle to the Standard Model, the Higgs boson, which has been observed by the LHC experiments ATLAS and CMS in 2012 [16, 17].

(This section is adapted from Ref. [22, 25, 31, 32].)

## 2.2. The top quark

After first direct experimental evidence in 1994, the top quark was finally discovered in 1995 by the Tevatron experiments CDF and DØ [4, 5]. Since then a multitude of measurements have been performed to determine top quark properties. One property which is extensively studied is its mass. With  $m_{\text{top}} = 173.34 \pm 0.36 \text{ (stat)} \pm 0.67 \text{ (syst)} \text{ GeV}$  [14], the top quark is the heaviest fundamental particle known. Therefore it plays an important role in various fields of particle physics. Naming the most popular ones:

- the top quark mass itself is a free parameter of the Standard Model, and therefore has to be determined by experiment
- with its short lifetime of  $\sim 10^{-24}$  s, the top quark is the only quark, which does not form hadronic bound states. Since it decays before hadronisation, the properties of a bare quark can be studied
- the Yukawa coupling of the top quark is close to unity, therefore it could play a special role in electroweak symmetry breaking
- the top quark mass together with the mass of the Higgs boson is related to the question if the electroweak vacuum is stable or not
- the top quark is a major background process for different searches of new physics. For such searches a precise knowledge of top quark properties is imperative

A variety of top quark mass measurements, with steadily increasing precision, have been published in the last two decades. An overview of the different results from ATLAS and CMS is presented in Fig. 2.5. In addition to these existing results, new analyses with more data and different techniques are continuously performed, to further enhance the precision on  $m_{\text{top}}$ . This section describes the production and decay properties of top quarks and briefly discusses the question of the top quark mass definition.

### 2.2.1. The CKM matrix

For an appropriate discussion of the production and decay mechanisms of the top quark, the CKM flavour mixing matrix has to be introduced. The CKM matrix, which is named after N. Cabibbo, M. Kobayashi and T. Masukawa, for their pioneering work in this field [3, 33], describes the mixing between mass and weak eigenstates. Since the electroweak symmetry is broken (cf. Section 2.1.3) the two eigenstates are not identical. Therefore the CKM matrix relates the states participating in the weak interaction with the states which are observed in experiment. Since the mass eigenstates are a superposition of different weak eigenstates, quarks can change their flavour via the exchange of  $W^\pm$  bosons. The relation between the weak eigenstates, denoted by a prime, and the mass eigenstates is

given by the CKM matrix

$$\begin{pmatrix} d' \\ s' \\ b' \end{pmatrix} = \begin{pmatrix} V_{ud} & V_{us} & V_{ub} \\ V_{cd} & V_{cs} & V_{cb} \\ V_{td} & V_{ts} & V_{tb} \end{pmatrix} \begin{pmatrix} d \\ s \\ b \end{pmatrix} \quad (2.36)$$

The particular entries in the CKM matrix define the transition of a quark of flavour  $i$  to flavour  $j$ , with the probability for such a flavour change given as  $|V_{ij}|^2$ . As can be seen from the structure of the matrix, only transitions between up- and down-type quarks are allowed.<sup>(7)</sup> The CKM matrix elements are measured to be [18]

$$V_{\text{CKM}} = \begin{pmatrix} 0.97427 \pm 0.00014 & 0.22536 \pm 0.00061 & 0.00355 \pm 0.00015 \\ 0.22522 \pm 0.00061 & 0.97343 \pm 0.00015 & 0.0414 \pm 0.0012 \\ 0.00886^{+0.00033}_{-0.00032} & 0.0405^{+0.0011}_{-0.0012} & 0.99914 \pm 0.00005 \end{pmatrix}$$

From these numbers it follows, that transitions within the same generations are preferred, since the values of the diagonal elements are close to unity. The corresponding CKM matrix elements for the top quark are  $|V_{td}|^2 = 7.8 \cdot 10^{-5}$ ,  $|V_{ts}|^2 = 1.6 \cdot 10^{-3}$  and  $|V_{tb}|^2 = 0.998$ . This means that if there is a top quark involved in an electroweak process, in 99.8 % of the cases the top quark is related to a bottom quark, instead of a down or strange quark.

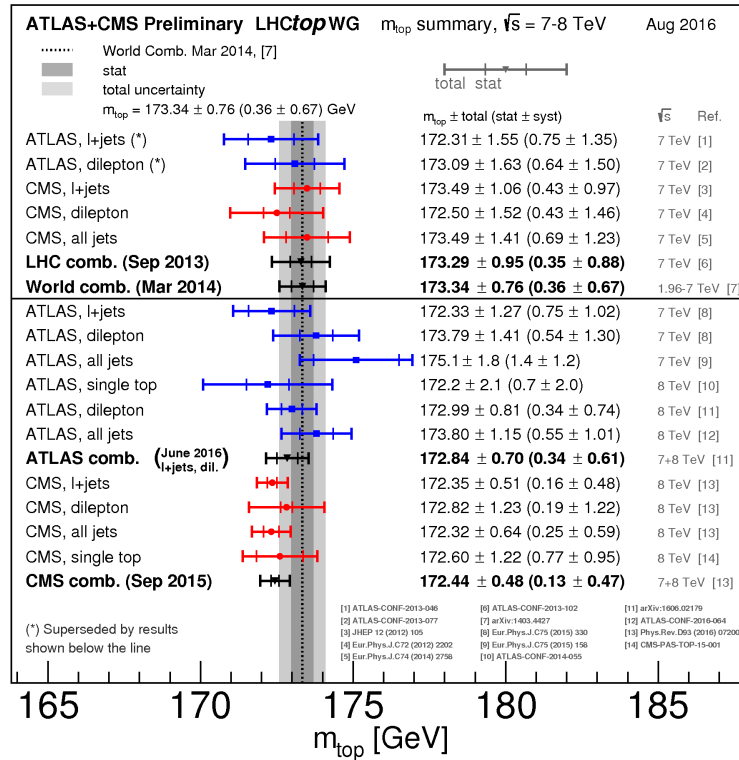


Figure 2.5.: Direct top quark mass measurements performed by ATLAS and CMS [34]

<sup>(7)</sup>Transitions within the up-type or the down-type quarks are called flavour changing neutral currents (FCNC). In the SM such FCNC do not exist at tree level and they are strongly suppressed at higher orders.

## 2.2.2. The parton distribution function

In collider experiments, the parton distribution function (PDF) describes the substructure of protons, the so-called partons. In the parton model, the proton consists of two up quarks and one down quark, which are the main constituents, temporarily created quark anti-quark pairs, originating from quantum fluctuations, and a multiplicity of gluons. The PDF gives the probability of finding a certain parton with a specific fraction of the proton's momentum  $x$  at a given momentum transfer scale  $Q$ . Therefore parton distribution functions are important in collider experiments to predict the outcome of proton-proton collisions. As can be seen in Fig. 2.6, which shows the PDF of the proton, the valence quarks on average carry high momentum fractions, while for decreasing  $x$ , gluons and other quark flavours become increasingly likely.

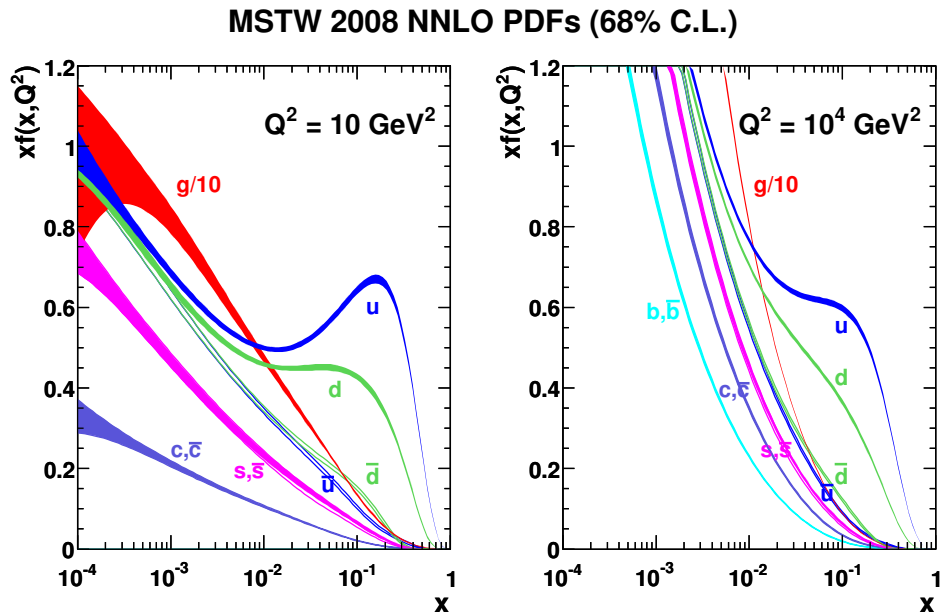


Figure 2.6.: Parton distribution function for the proton provided by the MSTW group [35] for two different momentum scales (the gluon contribution has been divided by 10).

## 2.2.3. Top quark production

There are two main mechanisms for producing top quarks: either single top quark production in which a top quark is produced in an electroweak interaction, or  $t\bar{t}$  pair production, in which a  $t\bar{t}$  system is created in a strong process.

### Single-top quark production

In electroweak interactions single top quarks can be produced in three different ways. The t-channel process describes the production of a top quark by a flavour excitation process: a virtual  $W$  boson is

radiated by a quark, which couples to a down-type quark, originating either from the quark-sea of the proton or from a gluon splitting process, thereby producing a top quark. Another production mechanism is the s-channel process, in which a virtual  $W$  boson is created if an up-type quark annihilates with a down-type anti-quark, or vice versa. The  $W$  boson then splits up into an (anti-)top quark and the corresponding down-type (anti-)quark. The final mechanism for single top quark production is the associated production of a  $W$  boson and a top quark, referred to as  $Wt$ -channel. In this channel either a down-type quark is excited by a gluon, which hence has sufficient energy to radiate a  $W$  boson and to become a top quark, or a down-type quark splits up into a virtual top quark and a  $W$  boson. The virtual top quark subsequently couples to a gluon, thereby becoming real. The theoretical cross sections as well as the measured values for the three electroweak production channels are given in Table 2.2 and the corresponding Feynman diagrams are shown in Fig. 2.7. Overall, there is

	t-channel [pb]	s-channel [pb]	$Wt$ -channel [pb]
$\sigma_t^{\text{theory}}$	$56.4^{+2.4}_{-1.1}$	$3.8 \pm 0.15$	$11.1 \pm 0.8$
$\sigma_{\bar{t}}^{\text{theory}}$	$30.7^{+1.1}_{-1.3}$	$1.8 \pm 0.08$	$11.1 \pm 0.8$
$\sigma_{t+\bar{t}}^{\text{measured}}$	$82.6^{+12.1}_{-12.1}$	$< 14.6 @ 95\%CL$	$23.0^{+3.6}_{-3.9}$

Table 2.2.: Single top quark production cross sections for the LHC at  $\sqrt{s} = 8$  TeV. The theoretical predictions are obtained from Ref. [36] and are calculated independently for the top and anti-top quark for  $m_{\text{top}} = 173.0$  GeV. The experimental results are a combination of top and anti-top quark cross sections and are taken from Ref. [37–39].

good agreement between theoretical predictions and experimental results. The total theoretical cross section for electroweak top quark production at LHC for a centre-of-mass energy of 8 TeV amounts to  $114.9^{+2.8}_{-1.9}$  pb.

An interesting point is, that the cross sections for producing a top quark or anti-top quark at LHC are different in the t- and s-channel. This is caused by the structure of the proton itself, which is composed of one  $d$  and two  $u$  valence-quarks. In case of the t-channel process the difference in cross sections can be understood as follows: Due to charge conservation an up quark can only radiate a  $W^+$ , whereas a down quark has to emit a  $W^-$  boson. Therefore, the emitted  $W$  boson annihilates either with a down-type quark resulting in a top quark or with a down-type anti-quark producing an anti-top quark. Since the number of up quarks in the proton is twice as large as the number of down quarks and the down-type sea quarks and anti-quarks occur at same rate, the production cross section for top quarks is larger than the cross section of anti-top quark production. A similar argument holds for the s-channel. Since there are more up quarks than down quarks in the proton, the virtual  $W$  boson, which is exchanged, will rather be a  $W^+$  than a  $W^-$ . Therefore the cross section for top quark production is enhanced.

## Top quark pair production

In contrast to single top quarks,  $t\bar{t}$  pairs are created via the strong interaction. The leading order Feynman diagrams are shown in Fig. 2.8 and can be classified in three different categories, the s-, t-

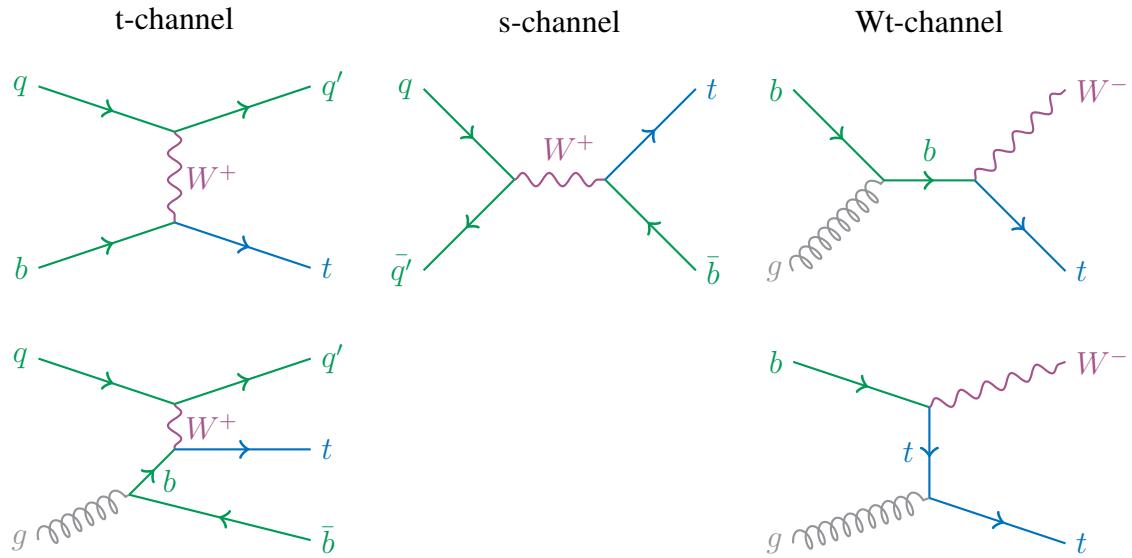


Figure 2.7.: Exemplary production mechanisms of single top quarks via the electroweak interaction

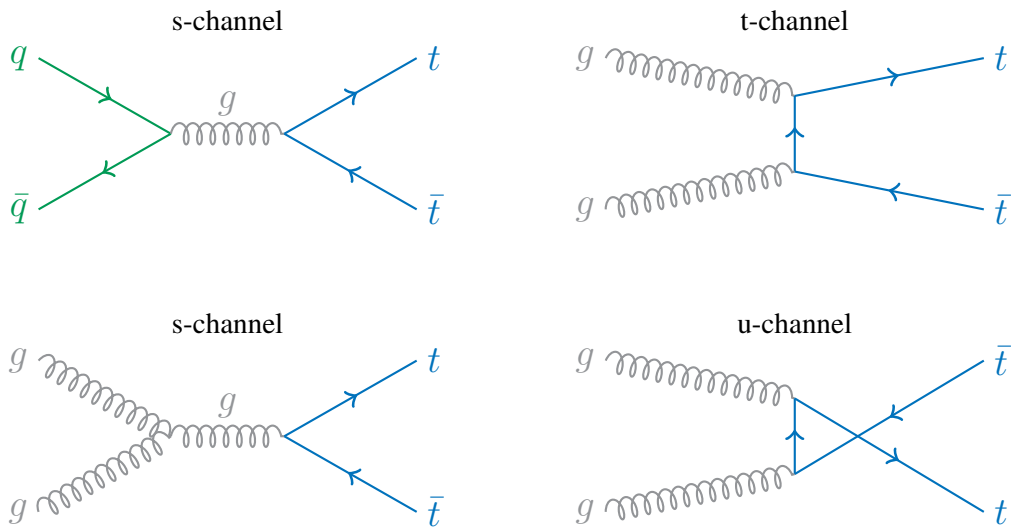


Figure 2.8.: Feynman diagrams for the leading order  $t\bar{t}$  pair production mechanisms

and u-channel. Similar to the electroweak production, the s-channel process describes the annihilation of a quark and an anti-quark, but instead of a  $W$  boson a gluon is emitted. The gluon subsequently splits up into a top and an anti-top quark. In this channel also an additional process is possible. As discussed in Section 2.1.2, gluons themselves carry colour and therefore couple to each other. This allows for a complementary process, in which two gluons annihilate under the emission of a virtual gluon, again splitting up into a  $t\bar{t}$  pair. In the t-channel, two gluons exchange a virtual top quark, which leads to the creation of a new  $t\bar{t}$  pair. The u-channel has the same initial and final state particles as the t-channel, but the assignment of the top and anti-top quark to the initial state gluons is reversed. In addition to the leading order diagrams, the  $t\bar{t}$  pair production can also involve higher order processes, which for next-to-leading (NLO) order are shown exemplary in figure 2.9. A trivial example for a

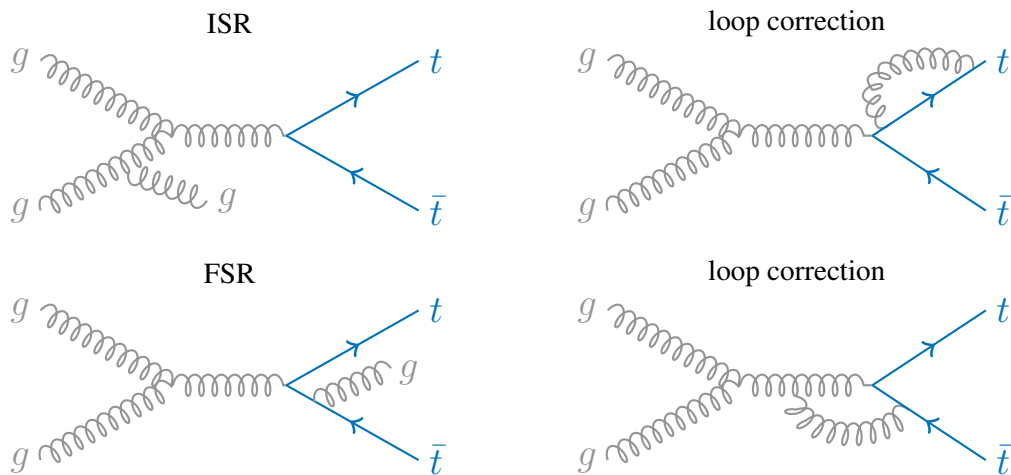


Figure 2.9.: Exemplary Feynman diagrams for next-to-leading order  $t\bar{t}$  pair production

NLO correction is the radiation of an additional gluon, either in the initial (ISR) or in the final state (FSR). In addition, also loop corrections have to be taken into account. Loop corrections describe the exchange of a purely virtual particle within the interaction. For example, as shown in Fig. 2.9, an additional virtual gluon can be exchanged between the gluon and one of the top quarks, or a top quark can emit a gluon and reabsorb it in a later stage. In total, the theoretical prediction for the  $t\bar{t}$ -production cross section of  $\sigma_{t\bar{t}} = 252.9^{+13.3}_{-14.5}$  pb [40] is in good agreement with the experimental result of  $\sigma_{t\bar{t}} = 242.4 \pm 10.3$  pb [40]. Therefore the  $t\bar{t}$  production cross section is roughly twice as large as the cross section of the electroweak single top production, and thus the strong force is the main source for top quarks at LHC.

## 2.2.4. Top quark decay

Because of its high mass, the top quark has a very short lifetime and decays via the electroweak interaction into a  $W$  boson and a down-type quark. As discussed in Section 2.2.1, this down-type quark is primarily a bottom quark. Since a  $W$  boson can either decay into a lepton and corresponding neutrino, referred to as leptonic decay or into an up-type quark and a down-type anti-quark (or vice versa)<sup>(8)</sup>, named hadronic decay, there are three different decay channels for a  $t\bar{t}$  pair, characterised

<sup>(8)</sup>Although the process  $W^+ \rightarrow t\bar{b}$  would technically be allowed, it is prohibited by the high rest mass of the top quark. Therefore, hadronic decays of  $W$  bosons involve only quarks other than the top quark.

## 2. Theory

by the decay of the involved  $W$  bosons. The corresponding branching fractions, which are  $\approx 1/3$  for the leptonic and  $\approx 2/3$  for the hadronic decay, are given in Table 2.3. Therefore one can distinguish three different decay modes for a  $t\bar{t}$  pair:

- the dileptonic channel, in which both  $W$  bosons decay into a lepton and a neutrino
- the lepton+jets channel, in which one  $W$  boson decays hadronically and the other leptonically
- the fully hadronic channel, where both  $W$  bosons decay into quarks

Decay mode	$W \rightarrow e\nu_e$	$W \rightarrow \mu\nu_\mu$	$W \rightarrow \tau\nu_\tau$	$W \rightarrow q\bar{q}'$
Branching fraction	$(10.71 \pm 0.16)\%$	$(10.63 \pm 0.15)\%$	$(11.38 \pm 0.21)\%$	$(67.41 \pm 0.27)\%$

Table 2.3.: Branching fractions for the  $W$  boson taken from Ref. [18].

### The dileptonic channel

With a probability of roughly 33% for a leptonic decay of the  $W$  boson, the predicted branching ratio for this channel is 10.5%<sup>(9)</sup>. Therefore it has the smallest branching ratio of the three channels. Its final state is characterised by two bottom quarks and a total of four high energetic leptons and neutrinos (cf. Fig. 2.10). Since there are two neutrinos in the final state, a kinematic reconstruction of the  $t\bar{t}$  pair is not possible. To measure top quark properties in this channel elaborated techniques have to be applied. However, despite the low branching fraction, the dileptonic decay offers a very clean event topology, because of the very low background contributions in this channel.

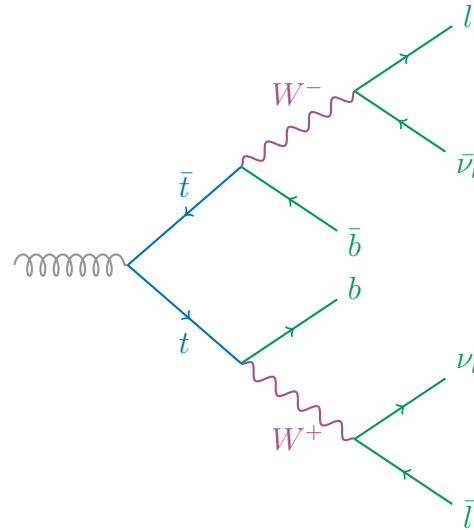


Figure 2.10.: The dileptonic  $t\bar{t}$ -decay

<sup>(9)</sup>These numbers include the contribution from all three lepton flavours. Since  $\tau$ -lepton decays are to roughly 65% hadronic [18] and furthermore are always accompanied by a  $\nu_\tau$ , most analyses exclude  $\tau$  leptons in top quark measurements. This reduces the branching fractions to  $\approx 5\%$  and  $\approx 30\%$  in the dileptonic and lepton+jets channel, respectively.

### The lepton+jets channel

The predicted probability for the lepton+jets channel is 43.8%<sup>(9)</sup>. In this channel the final state consists of two bottom quarks, two light quarks, one high energetic lepton and one neutrino (cf. Fig. 2.11). In contrast to the dileptonic channel, although a neutrino is present, the kinematic reconstruction of the  $t\bar{t}$ -decay is feasible. The main background in this channel originates from  $W$ +jet production, while a minor contribution arises from QCD multijet. Since the lepton+jets decay channel is well-balanced between a clean event signature and a large branching fraction, it is the preferred channel for many top quark measurements.

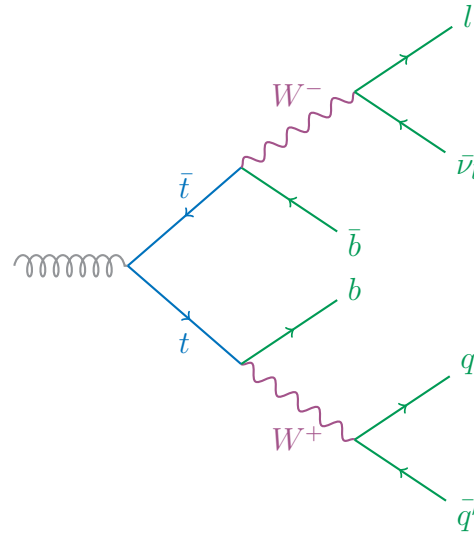


Figure 2.11.: The lepton+jets  $t\bar{t}$ -decay

### The fully hadronic channel

In the fully hadronic channel both  $W$  bosons decay hadronically, which corresponds to a probability of 45.7%. Therefore the fully hadronic channel has the largest branching fraction of the three channels. The event signature is described by four light and two bottom quarks (cf. Fig. 2.12). In contrast to the other two channels there are no high energetic leptons or neutrinos in the final state. The absence of neutrinos has the advantage that all decay particles of the  $t\bar{t}$ -system can be detected, allowing a full reconstruction. The dominant background process for the fully hadronic channel is QCD multijet production. Due to the absence of leptons and neutrinos the rejection of these background events is very challenging.

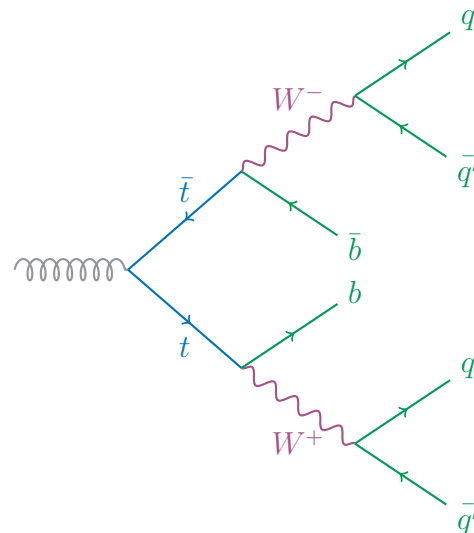


Figure 2.12.: The fully hadronic  $t\bar{t}$ -decay

### 2.2.5. The top quark mass

As already described, the top quark is the heaviest fundamental particle known. The precise measurement of  $m_{\text{top}}$  is therefore one of the goals of high energy particle accelerator experiments, like ATLAS or CMS. As shown in Fig. 2.5, a multitude of measurements have been performed to measure  $m_{\text{top}}$ . All those results are so-called direct measurements of the top quark MC mass. Such measurements use kinematic distributions of the top quark decay products and extract  $m_{\text{top}}$  by comparing the measured distributions to MC predictions for specific top quark MC parameters. Therefore the extracted value of the top quark mass is directly related to the MC parameter for  $m_{\text{top}}$ .<sup>(10)</sup>

In QCD the mass of a quark depends on the specific properties of the renormalisation scheme used. Accordingly, different mass schemes, like the pole mass or the  $\overline{\text{MS}}$  mass scheme exist (cf. Ref. [18]), which are related to each other by perturbation theory. However, due to its dependence on the specific non-perturbative hadronisation model within the MC simulation, the top quark MC mass is not well defined within the framework of QCD. Therefore there is a discrepancy between the top quark MC mass, as measured in direct measurements, and the pole mass scheme defined by theory, which is estimated to be on the order of 1 GeV [41]. With their increasing precision, direct measurements have reached a point where their overall uncertainty has become competitive with the uncertainty on the top quark mass definition. Therefore there is a wide effort ongoing to resolve the theoretical relation between the top quark MC mass and other mass definitions. To avoid the issue of the ill-defined top quark MC mass, the top quark pole mass ( $m_{\text{top}}^{\text{pole}}$ ) can be inferred from data. Such indirect measurements, deduce the top quark pole mass by exploiting the dependence of the measured  $t\bar{t}$  cross section on  $m_{\text{top}}^{\text{pole}}$ . The results of such measurements are shown in Fig. 2.13. Although pole mass measurements have not reached the precision of the direct top quark mass results yet, they could become competitive in the future.

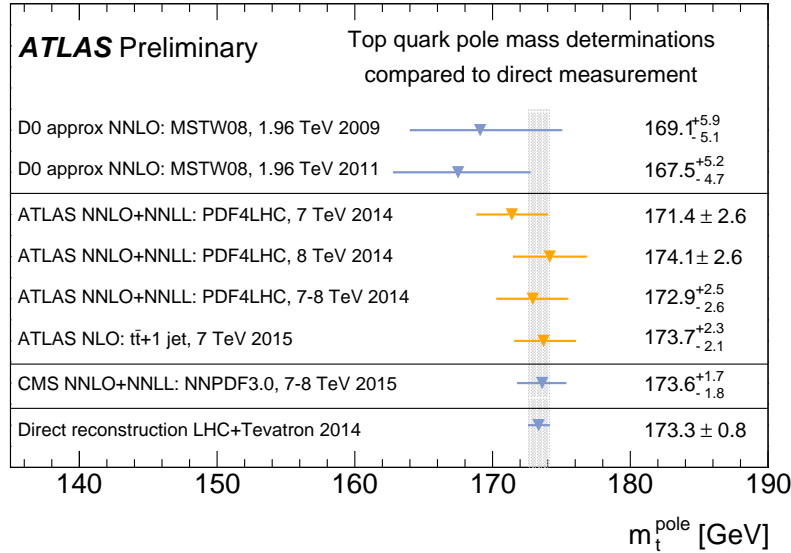


Figure 2.13.: Measurements of the top quark pole mass performed by ATLAS, CMS and DØ [34].

<sup>(10)</sup>The mass measured in this analysis also corresponds to the top quark MC mass.

## 3. Experimental setup

In this chapter the experimental setup, required to measure the top quark mass, is described. First the Large Hadron Collider is introduced, while second the ATLAS experiment is briefly summarised. Furthermore, the top quark production at the Large Hadron Collider is discussed, where in the last part the principles of MC simulations, which are used to compare the measured data to theoretical predictions, are explained.

### 3.1. The LHC accelerator

The Large Hadron Collider (LHC) is an international experiment, located at CERN<sup>(1)</sup> near Geneva, Switzerland, built to test the Standard Model and unveil new physics phenomena. Besides smaller experiments, CERN hosts the LHC, which is, to date, the most energetic particle accelerator build by mankind. The LHC is a circular machine which has a circumference of 27 km and is housed in a tunnel below ground, originally built for its predecessor the Large Electron Positron Collider (LEP). The accelerator is designed to accelerate protons<sup>(2)</sup> to a centre-of-mass energy of  $\sqrt{s} = 14$  TeV. In order to reach such a high energy, LHC depends on a complex pre-accelerator chain, which uses already existing infrastructure at CERN. In a first step, protons are accelerated to an energy of 50 MeV by the Linac 2 accelerator. The particles are subsequently inserted in the Proton Synchrotron Booster and the Proton Synchrotron to be further accelerated to 1.4 GeV and 25 GeV. As last part of the pre-acceleration process, the Super Proton Synchrotron increases the energy of the protons to 450 GeV. The LHC then accelerates protons to their final collision energy, which amounted to 4 TeV during the 2012 data taking period, corresponding to a proton-proton centre-of-mass energy of  $\sqrt{s} = 8$  TeV. An overview over the CERN accelerator complex is shown in Fig. 3.1.

The task of the LHC comprises three things: particles have to be accelerated, which is done by radio-frequency (RF) cavities, particles have to be bend on a circular track, which is achieved by dipole magnets and the positions of particles have to be adjusted, which is accomplished by multi-pole magnets. After the pre-acceleration, the protons are filled in the two beam pipes of the LHC, where the protons rotate clockwise and counter-clockwise. For each beam pipe there is one RF cavity, which accelerates the protons by up to 16 MeV per turn with an electromagnetic RF field. A picture of such a cavity is shown in Fig. 3.2(a). To hold the particles on a circular path a total of 1232 15 m long dipole magnets are used, shown in Fig. 3.2(b), which reach a peak magnetic field of 8.33 T. In order to achieve such high performances, both the RF cavities and the magnets have to be superconductive, which means that they have to be cooled down to 1.9 K. In addition a multitude of magnets with different designs, are responsible to steer and focus the protons. In the LHC, protons are subdivided into 1374 bunches with a spacing of down to 25 ns and an average of  $1.7 \cdot 10^{11}$  protons per bunch.

<sup>(1)</sup>CERN is the acronym of the European Organization for Nuclear Research, which operates the largest particle physics laboratory in the world and pursues a variety of experiments in different areas of particle physics.

<sup>(2)</sup>LHC is also able to accelerate heavy ion nuclei to centre-of-mass energies of 2.76 TeV / nucleon.

### 3. Experimental setup

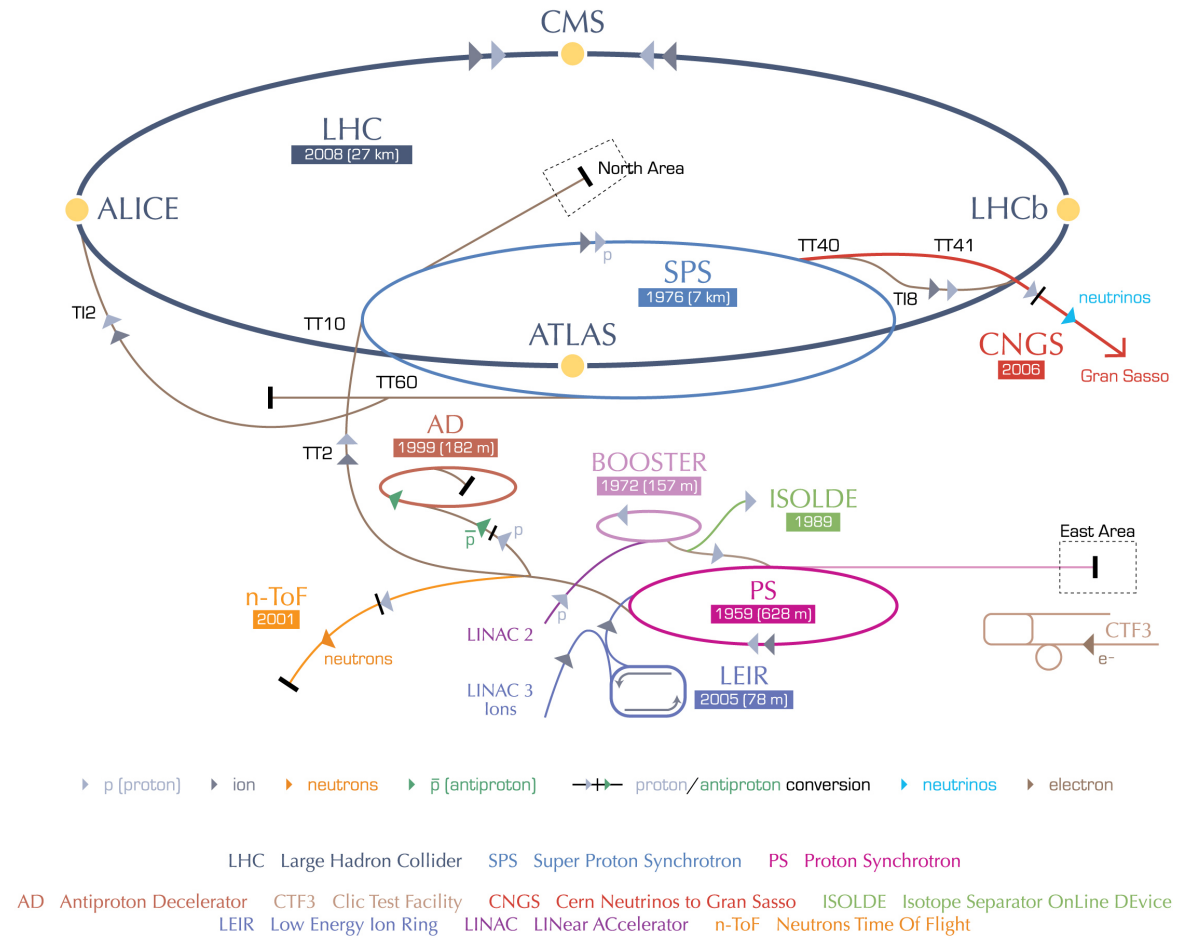


Figure 3.1.: The CERN accelerator complex: The LHC ring with the four major experiments (in dark blue) together with the pre-accelerator chains for protons and heavy ions [42].



Figure 3.2.: Pictures of a RF cavity (Fig. (a)) and a dipole magnet (Fig. (b)) prior to their installation in the LHC tunnel [43, 44].

The actual number of proton-proton collisions can be described by the instantaneous luminosity of the collider. The luminosity is a function of different parameters, like the number of bunches, the number of protons in a bunch and the spatial spread of the bunches. In 2012, the integrated luminosity, describing the overall amount of proton-proton collisions collected<sup>(3)</sup>, corresponds to  $23.1 \text{ fb}^{-1}$ .

Besides two smaller experiments, LHCf and TOTEM, there are four major experiments affiliated to the LHC. The ALICE experiment studies the quark-gluon plasma in heavy ion collisions, whereas the LHCb experiment is dedicated to  $b$ -physics. The ATLAS and CMS experiments are both general-purpose detectors covering a broad field of particle physics, with the benefit to cross check each other's results.

(This chapter is based on Ref. [43, 46].)

## 3.2. The ATLAS experiment

The ATLAS<sup>(4)</sup> experiment is a forward-backward symmetric multi-purpose detector located in one of the experimental caverns of the LHC. It has been designed to cover a wide range of particle physics topics, like the precise measurement of Higgs and top quark properties and the search for new physics phenomena. The ATLAS detector, which is shown in Fig. 3.3, has a cylindrical shape and is divided into a central part, called the barrel, and two end-cap parts. The detector is located at LHC point 1, one of the four sites, where protons are brought to collision. ATLAS consists of three different detector layers, the inner detector (ID), the calorimeter (CAL) and the muon spectrometer (MS). To measure the momenta of charged particles the whole detector is immersed in several magnetic fields generated by superconductive magnets. The enormous amount of data taken is handled by a specifically designed trigger and data acquisition system. Besides these main detector parts, which are briefly described in the following, there are three smaller detector modules. The main purpose of ALFA and LUCID is to measure the luminosity delivered to the experiment, while the function of the zero-degree calorimeter is to determine the centrality of heavy-ion collisions.

(For this section Ref. [48–54] have been used.)

### 3.2.1. The ATLAS coordinate system

ATLAS uses a right-handed coordinate system, with the nominal interaction point in the centre of the detector as origin. The beam axis of the LHC defines the  $z$ -axis, with the positive  $x$ -axis pointing to the centre of the LHC ring and the  $y$ -axis pointing upwards. Because of its shape, cylindrical coordinates are used to describe objects in the detector. The azimuthal angle  $\phi$  is measured around the beam axis, while the polar angle  $\theta$  is defined towards it. However, instead of the polar angle the pseudorapidity, given as  $\eta = \ln(\tan(\theta/2))$ , is used<sup>(5)</sup>. The angular separation  $\Delta R$  between objects in the detector can therefore be expressed as  $\Delta R = \sqrt{\Delta\phi^2 + \Delta\eta^2}$ .

<sup>(3)</sup>In 2012, the LHC has reached a peak instantaneous luminosities of  $7.7 \cdot 10^{33} \text{ cm}^{-2}\text{s}^{-1}$ . With such high instantaneous luminosities, additional proton-proton collisions in a bunch crossing, so-called pile-up events, occur at high rates. In 2012 the average number of such pile-up events amounted to 20.7 [45].

<sup>(4)</sup>ATLAS is the acronym for A Toroidal LHC Apparatus

<sup>(5)</sup>For high energies,  $\eta$  is approximately equal to the Lorentz invariant rapidity  $y$ , defined as  $y = \frac{1}{2} \cdot \ln((E + p_z) / (E - p_z))$ .

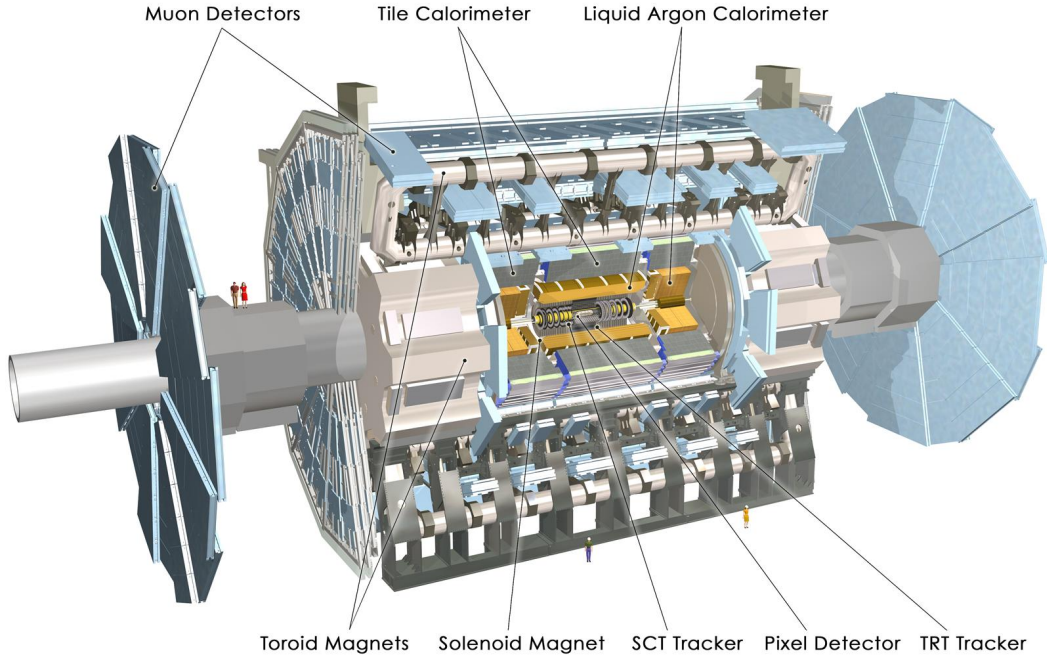


Figure 3.3.: Computer generated view of the ATLAS detector with its main components: The inner detector, the calorimeter system, the muon spectrometer and the magnet system [47].

#### 3.2.2. The magnet system

The ATLAS magnet system consists of four superconducting Niob-Titan magnets, which are cooled to 4.5 K. The magnetic field provided by the magnets is essential for the momentum measurements in the inner detector and in the muon spectrometer. According to the Lorentz force

$$\mathbf{F} = q(\mathbf{v} \times \mathbf{B}) \quad (3.1)$$

charged objects experience a force proportional to their momentum, which leads to a bending of the particle's path. Therefore the momentum of charged particles can be determined by measuring their tracks. The ATLAS magnet system is shown in Fig. 3.4 and consists of one solenoid and three toroid magnets. The solenoid is centred along the beam axis and is built to supply a magnetic field of 2 T for the inner detector. The toroids, one in the barrel and one in each end-cap, are arranged radially symmetric around the beam axis. With a nominal current of 20.5 kA the toroids provide a peak field of up to 4.1 T.

#### 3.2.3. The inner detector

The inner detector has been designed to provide precise vertex identification and to achieve a momentum resolution of  $\sigma_{p_T}/p_T = 0.05\% \cdot p_T \oplus 1\%$ . It encloses the beam pipe within a pseudorapidity range of  $|\eta| < 2.5$  and is therefore the most central element of the ATLAS detector. The ID consists of three parts, the pixel detector, the semiconductor tracker and the transition radiation tracker. As can be seen

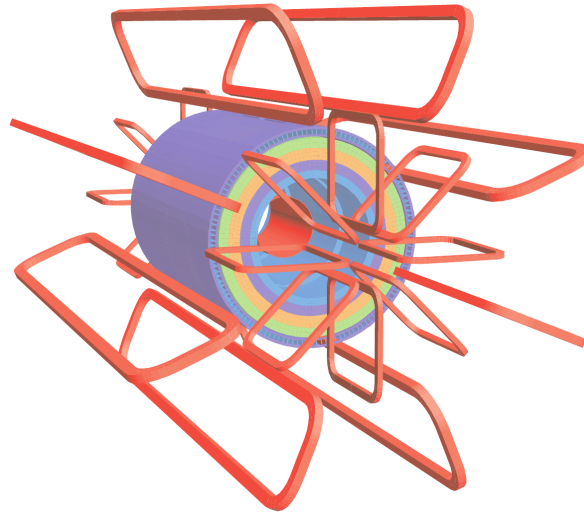


Figure 3.4.: The ATLAS magnet system coloured in red [48]. Shown are the barrel coils, the end-cap toroidal coils and the solenoid embedded in the calorimeter.

in Fig. 3.5, the different parts are arranged cylindrical around the beam pipe, within the barrel region, while in the end-caps the elements are orientated perpendicular to the beam line.

The pixel detector is constructed to provide a hermetic coverage around the interaction point with fine

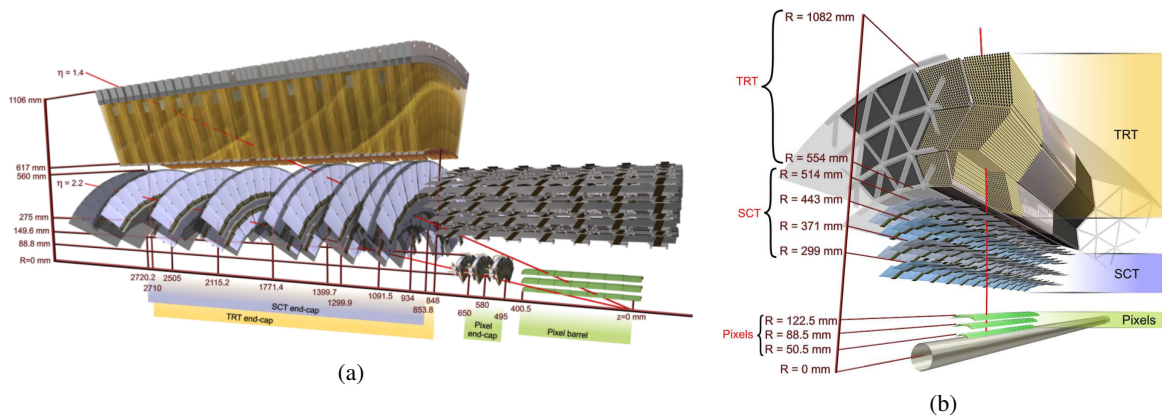


Figure 3.5.: Schematic view of the end-cap (Fig. (a)) and the barrel (Fig. (b)) part of the inner detector [55].

granularity. To reconstruct primary as well as secondary vertices from short lived particle decays, like  $b$ -hadrons, the detector is located close to the interaction point. It consists of overlapping pixel sensors, which are mounted on three barrels surrounding the beam axis, and on a total of six disk layers perpendicular to the beam in the end-cap regions. The pixel detector provides a spatial resolution of about  $\approx 10 \mu\text{m}$  in the  $R$ - $\phi$  plane and  $\approx 115 \mu\text{m}$  in the  $z$  direction. The semiconductor tracker (SCT) surrounds the pixel detector and is composed of stereo silicon strip modules, each consisting of two layers rotated by  $40 \text{ mrad}$  to each other. Its elements are arranged in four barrels parallel to the beam line and are mounted on nine disks in each of the end-caps. Overall, the semiconductor tracker is designed to give at least four precision space-point measurements, with an accuracy of  $\approx 17 \mu\text{m}$  in

the transverse plane and  $\approx 580 \mu\text{m}$  along the beam direction. Since both, the pixel detector and the SCT, are silicon-based they are prone to irradiation during operations. To suppress electronic noise, originating from radiation damage, the modules are kept at temperatures below  $-5^\circ$ . The inner detector is completed by the transition radiation tracker (TRT). It is build from thin gas-filled proportional drift tubes, equipped with a gold-plated tungsten wire. In the barrel region the tubes are aligned along the beam pipe, while they are radially positioned in each end-cap. The TRT has a spatial resolution of  $\approx 130 \mu\text{m}$  and provides an average of 36 hits per track. Its main purpose is the identification of electrons by the detection of transition-radiation photons.

#### 3.2.4. The calorimeter system

The ATLAS calorimeter system consists of two parts, the electromagnetic calorimeter (ECAL) specifically designed to measure the energy of mainly electromagnetically interacting particles like electrons and photons and the hadronic calorimeter (HCAL) constructed to determine the energy of hadrons. Both calorimeters are sampling type calorimeters, which means that they consist of alternating layers of high-density material, in which the particles can induce showers, and readout layers, where these showers are measured. The ATLAS calorimeter system covers a range of  $|\eta| < 4.9$  and due to the full coverage in the azimuthal angle allows for the measurement of missing transverse energy. A schematic view of the calorimeter system is presented in Fig. 3.6.

The electromagnetic calorimeter uses lead as absorber material and liquid argon as active medium.

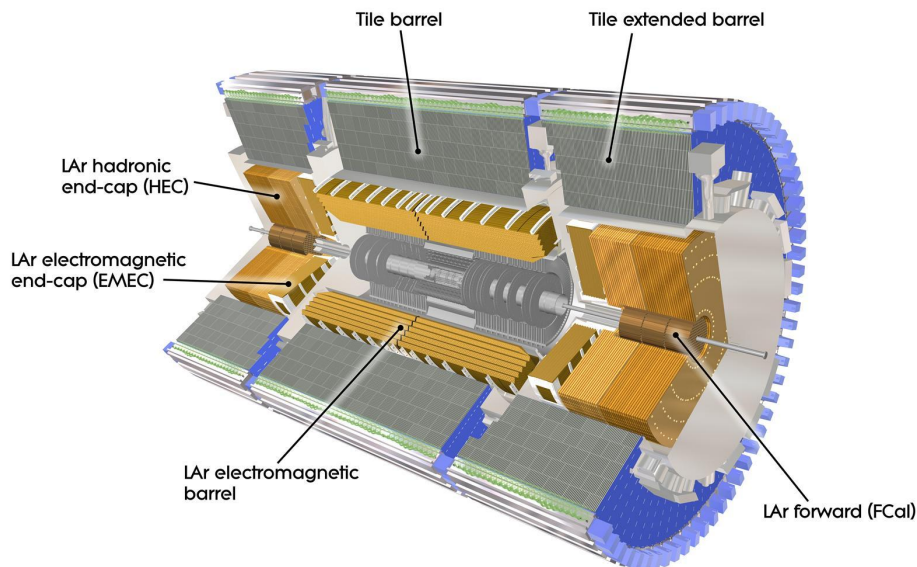


Figure 3.6.: Schematic view of the ATLAS calorimeter system [56]. In the barrel region, the electromagnetic calorimeter encloses the inner detector, which itself is embedded in the tile calorimeter. The end-cap region comprise the forward calorimeters, which are surrounded by the electromagnetic and hadronic end-cap calorimeters, encased by the extended tile calorimeters.

When passing through the absorber, incoming particles produce electromagnetic showers which ionise the argon atoms in the active layer. Since the energy of the incoming particles is proportional to the total number of created charges, the energy of electromagnetic interacting particles can be measured by determining the total number of ionised atoms. The accordion-shaped ECAL provides a full coverage in  $\phi$  and includes a pseudorapidity of  $|\eta| < 3.2$ . The barrel module extends up to  $|\eta| < 1.475$  and the end-caps range from  $1.375 < |\eta| < 3.2$ , where the overlap between the modules ensures a continuous  $\eta$  coverage. For  $|\eta| < 1.8$  an instrumented layer of liquid argon, the so-called presampler, is used to account for energy losses prior to the calorimeter. Overall, the electromagnetic calorimeter offers a thickness of 22 and 24 radiation lengths in the barrel and end-cap regions, and provides a design energy resolution of  $\sigma_E/E = 10\%/\sqrt{E(\text{GeV})} \oplus 0.7\%$ .

The hadronic calorimeter consists of three different components, the tile calorimeter, the hadronic end-cap calorimeter and the forward calorimeter. The main component of the HCAL is the tile calorimeter. The barrel part covers a pseudorapidity of  $|\eta| < 1$ , while the extended barrels reach from  $0.8 < |\eta| < 1.7$ , where the overlap, similar to the ECAL, prevents gaps in  $\eta$ . The tile calorimeter surrounds the electromagnetic calorimeter and is made of steel absorbers and scintillating tiles. Attached to the scintillators are wavelength-shifting fibres, converting the light induced by ionising particles to visible light, which is detected by photomultiplier tubes. Similar to the ECAL, the energy of impinging particles can be deduced from the total amount of light collected. In contrast to the tile calorimeter, the hadronic end-cap calorimeter uses copper as absorber material and liquid argon for ionisation. It covers a range of  $1.5 < |\eta| < 3.2$ , thereby overlapping with the forward calorimeter. The forward calorimeter system itself encloses the beam pipe and is shifted with respect to the electromagnetic calorimeter to avoid backscattering of neutrons. It covers an  $\eta$  range of  $3.1 < |\eta| < 4.9$  and comprises three parts which all use liquid argon as active medium. Closest to the interaction point, is a copper calorimeter mainly designed to measure electromagnetic interactions, followed by two tungsten calorimeters, intended for hadronic measurements. In total the HCAL provides a thickness of about 10 interaction lengths over the whole region. The design energy resolution of the tile and hadronic end-cap calorimeters is  $\sigma_E/E = 50\%/\sqrt{E(\text{GeV})} \oplus 3\%$ , where the forward calorimeter provides a design resolution of  $\sigma_E/E = 100\%/\sqrt{E(\text{GeV})} \oplus 10\%$ .

### 3.2.5. The muon spectrometer

The ATLAS muon spectrometer is specifically constructed to measure the tracks, and therefore the momenta, of muons. A schematic overview of the muon system is shown in Fig. 3.7. Since muons are minimal ionising particles, they are usually the only detectable particles, which escape the calorimeters. To determine their positions, ATLAS is equipped with precision tracking chambers, so-called monitored drift tubes (MDT). They cover a pseudorapidity range of  $|\eta| < 2.7$  and are mounted in three consecutive cylindrical layers in the barrel region and on four disks in each end-cap. The monitored drift tubes are designed to deliver precision-tracking information in the  $\eta$  plane, but do not provide any  $\phi$  measurements. The MDTs consist of multiple layers of aluminium tubes, filled with a gaseous mixture of argon and carbon dioxide. In each tube, a gold-plated tungsten rhenium wire is centred, which is kept at high voltage. Therefore, similar to the TRT, ionisation charges created by traversing muons are collected and readout. With this setup, a z-resolution of  $35 \mu\text{m}$  is achieved. Due to the high rate of particles near the beam axis, the disk closest to the interaction point, with  $2.0 < |\eta| < 2.7$ , is equipped with high rate capable cathode strip chambers (CSC) instead of MDTs. The CSCs are multiwire proportional chambers and follow the same principle as the muon drift tubes. However, instead

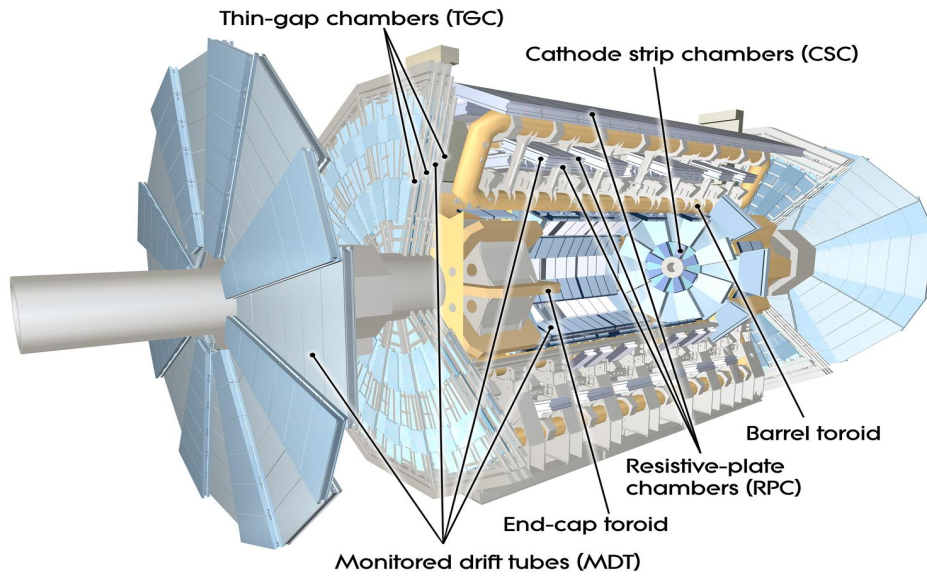


Figure 3.7.: The ATLAS muon system [57]

of being segmented in different tubes with single wires, multiple wires within a single module are used. The cathode strip chambers provide an  $\eta$ -resolution of  $40 \mu\text{m}$ . Overall the muon spectrometer is designed to provide a momentum resolution of 4 - 5% over most of the kinematic region except for high transverse momenta, where the resolution increases to  $\approx 10\%$  for a 1 TeV muon.

To trigger on muon tracks, the muon system is complemented with additional fast readout modules.<sup>(6)</sup> The resistive plate chambers (RPC) are gaseous parallel electrode-plate detectors, installed in the barrel region ( $|\eta| < 1.05$ ), while the thin gap chambers (TGC), a type of slim multiwire proportional chamber, are used in the end-cap regions of ATLAS ( $1.05 < |\eta| < 2.4$ ). In addition, these detectors offer the benefit of providing a rough  $\phi$  position measurement with a resolution of about 3 – 10 mm.

#### 3.2.6. Data processing

The ATLAS data processing consists of two main parts. First the data has to be readout from the detector. Since it is not feasible to record all of the proton-proton collisions of the 20 million bunch crossings per second<sup>(7)</sup> a trigger system is employed to select only the interactions of interest. The trigger consists of three subsystems, the level-1 trigger, the level-2 trigger and the event filter. The task of the level-1 trigger is to search for high transverse momentum objects like electrons or jets and to look for high values of total and missing transverse energy. Since the level-1 trigger has to decide in  $< 2.5 \mu\text{s}$  whether to keep an event or not, it uses only limited detector information from the muon system and the calorimeters. Overall, the level-1 trigger can handle a maximum rate of 65 kHz<sup>(8)</sup>. If the level-1 trigger accepts an event, it defines regions of interest, which are transferred to the level-2 trigger. For these regions, which contain about 2% of the overall event information, the level-2 trigger

<sup>(6)</sup>Due to the slow drift time of the ionised charges, MDTs and CSCs can not be used for triggering at the LHC.

<sup>(7)</sup>During Run I the LHC has been operated with an increased bunch spacing of 50 ns, since 2015 the design bunch spacing of 25 ns is used.

<sup>(8)</sup>The numbers represent the values for the 2012 data taking period. The actual design values are 100 kHz, 3.5 kHz and 200 Hz, for the level-1 trigger, level-2 trigger and event filter, respectively.

uses the full detector information to further reduce the number of events to a rate of 5 kHz<sup>(8)</sup>. In a final step, the event filter, which employs offline analysis procedures, lowers the rate to 400 Hz<sup>(8)</sup>.

Second the events selected by the trigger system have to be reconstructed, which means that the electrical signals from the different ATLAS subdetectors are interpreted as physical objects like electrons or jets. This is done on-site at the CERN data centre. However, to cope with the large amount of data produced by ATLAS, which amount to several Petabyte a year, the Worldwide LHC Computing Grid (WLCG) has been created. The WLCG consists of several computing centres across the globe, which are responsible for the reconstruction, backup and analysis of ATLAS data.

### 3.3. Top quark production at LHC

As explained in Section 2.2.3, there are two mechanisms to produce top quarks, the single top quark production via the electroweak interaction with a cross section of  $\sigma_t = 114.9_{-1.9}^{+2.8}$  pb and the more probable creation of  $t\bar{t}$  pairs through the strong force with  $\sigma_{t\bar{t}} = 252.9_{-14.5}^{+13.3}$  pb. The strong production happens either through the annihilation of a quark and an anti-quark or the fusion of two gluons. To determine the dominant process for LHC at  $\sqrt{s} = 8$  TeV, one can look at the momentum fractions, partons have to carry to produce a  $t\bar{t}$ -system. The square of the centre-of-mass energy of two colliding partons can be written as

$$\hat{s} = (p_a + p_b)^2 \quad (3.2)$$

where the momentum of a parton  $p_i$  can be expressed in terms of the fraction  $x_i$  of the proton's momentum. In relativistic approximation, the momentum of the proton is equal to the beam energy and therefore

$$p_a = \begin{pmatrix} x_a \\ 0 \\ 0 \\ x_a \end{pmatrix} \cdot E_{beam} \quad p_b = \begin{pmatrix} x_b \\ 0 \\ 0 \\ -x_b \end{pmatrix} \cdot E_{beam} \quad (3.3)$$

To produce a  $t\bar{t}$  pair  $\sqrt{\hat{s}}$  has to be at least equal to the rest mass of the  $t\bar{t}$  system

$$\hat{s} = (p_a + p_b)^2 \geq (2 m_{top})^2 \quad (3.4)$$

For simplicity one can assume that  $x_a \approx x_b$ , which means that both partons carry a similar momentum fraction. With this assumption, the momentum fraction required to create a  $t\bar{t}$ -pair is given by

$$x \geq \frac{2 m_{top}}{\sqrt{s}} \quad (3.5)$$

where  $\sqrt{s} = 2 \cdot E_{beam}$  is the centre-of-mass energy of the collider. For  $\sqrt{s} = 8$  TeV and an assumed top quark mass of 172.5 GeV, the momentum fraction a parton has to carry is about 0.04. Since there are much more gluons than quarks with such a low momentum fraction in the proton (cf. Fig. 2.6), the gluon-gluon fusion is the main  $t\bar{t}$ -production process at LHC. Overall, the total number of  $t\bar{t}$  pairs produced at LHC can be calculated, from the cross section and the total integrated luminosity by

$$N_{event} = L \cdot \sigma_{event} \quad (3.6)$$

With a luminosity of  $23.1 \text{ fb}^{-1}$  this corresponds to roughly six million  $t\bar{t}$ -pairs produced in the 2012 data taking period.

### 3.4. Monte Carlo event generation

To compare experimental data to theoretical expectations, Monte Carlo simulations (MC)<sup>(9)</sup> are indispensable for high energy physics. Monte Carlo generators are dedicated software tools which predict the outcome of collider experiments and thus are used to interpret experimental results. The two essential principles used for the prediction of physical observables with MC simulations are perturbation theory and the factorisation theorem. In mathematics, perturbation theory is used to approximate the result of a given problem, if no exact solution can be calculated. It can be used if it is possible to formulate the problem in terms of a power series

$$F(x) = a_0x^0 + a_1x^1 + a_2x^2 + a_3x^3 + \mathcal{O}(x^4) \quad (3.7)$$

The basic idea is that, if  $x < 1$ , higher orders of  $x$  add only increasingly small corrections to the final result. So under this condition, a problem can be approximated by taking into account only leading order contributions while higher order corrections are neglected. This approach is commonly used within quantum field theories, where the complex equations are approximated with power series, to predict physical observables. For example, the matrix element needed to predict the  $t\bar{t}$  production cross section via the strong interaction, can be expressed and calculated in terms of an expansion in orders of  $\alpha_s$ . The leading order process is described by the tree level, which in this case has been shown in Fig. 2.8. Since each vertex in the Feynman graph is proportional to  $\alpha_s$ , adding an additional leg or loop to the diagram (cf. Fig. 2.9), means incorporating a higher order correction. Calculating the lowest order Feynman diagram, will give a good approximation of the experimental measurement, however by including higher orders, which are increasingly difficult to calculate, the data will be described more precisely. Therefore, with the experimental precision reached by experiments, it is essential to have higher-order corrections available, to perform precise measurements of SM quantities like kinematic distributions or top quark properties. Most of the MC generators, presently at hand, include the full NLO matrix elements for the single top quark and  $t\bar{t}$  processes.

The other basic principle for MC event generation is the factorisation theorem, which basically implies that a proton-proton collision can be subdivided into different stages:

- **Parton distribution function:** As detailed in Section 2.2.2, the parton distribution function describes the momentum fractions of partons within the proton. Therefore the PDF determines the initial state of the hard scattering process in a proton-proton collision.
- **Hard process:** The hard scattering process, refers to the calculation of the matrix element of the process of interest in the proton-proton collision. In case of  $t\bar{t}$  production it describes the annihilation of the initial state partons, the creation of the  $t\bar{t}$ -pair as well as the decay of the top quarks.
- **Parton shower:** The parton shower describes the radiation of additional gluons from initial and final state partons. However, since  $\alpha_s$  increases at low momentum scales (cf. Section 2.1.2), QCD perturbation theory breaks down for energies of the order  $\Lambda_{\text{QCD}}$ . Therefore parton showering can only be used down to an intrinsic cut-off energy of  $\mathcal{O}(1\text{GeV})$ .

<sup>(9)</sup>The name derives from the method used to integrate high-complex probability density functions in multi-dimensional phase spaces. In most cases such integrations can not be performed analytically and therefore numerical Monte Carlo techniques have to be used.

- **Hadronisation:** Due to the low energy scale involved, the formation of colourless hadrons from coloured particles, in contrast to the hard scattering and the parton shower, can not be described by perturbative QCD. Therefore QCD-inspired models have to be used to characterise the hadronisation process.
- **Underlying event:** The underlying event describes the evolution of the proton remnants. Since they carry colour they are colour-connected to the hard process and hadronise themselves. Furthermore additional partons from the remnants can interact with each other.
- **Unstable particle decays:** Many of the hadrons created during the hadronisation process are unstable particles, therefore subsequent hadron decays have to be incorporated in the simulation.

A schematic overview over the different steps of the event simulation is shown in Fig. 3.8. The final step of the event generation is the detector simulation, in which the detector response is modelled. The output of the detector simulation undergoes the same reconstruction algorithms as data and therefore can be compared to experimental measurements.

(For this section Ref. [18, 58] have been used.)

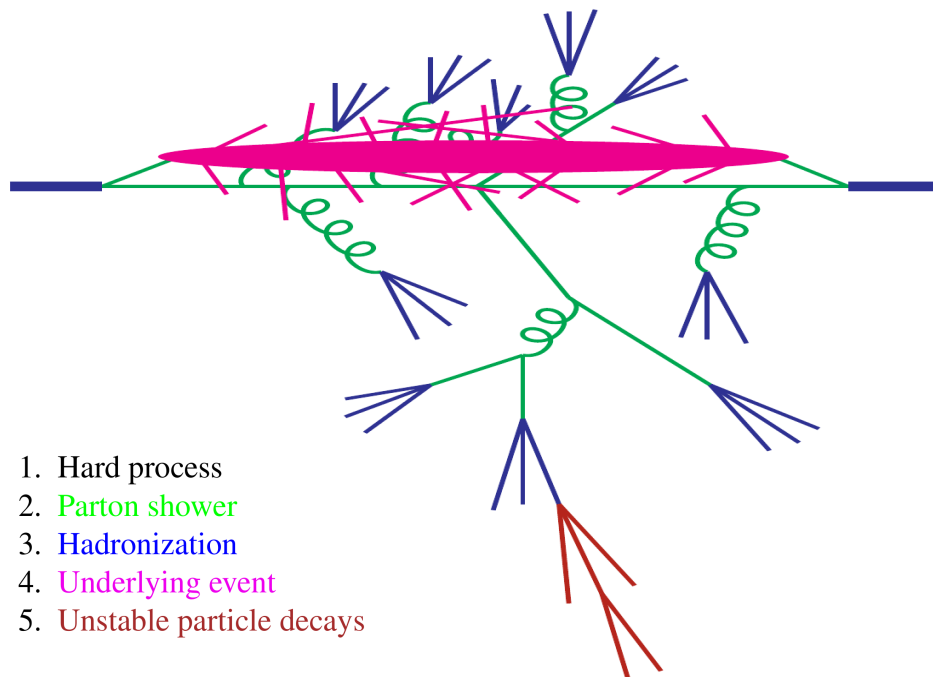


Figure 3.8.: Schematic overview of the structure of a proton-proton collision [58]. The colour code for the different stages of the event generation is given in the legend.



## 4. Data and Monte Carlo Samples

This analysis is performed with proton-proton collisions at a centre-of-mass energy of 8 TeV, recorded with the ATLAS detector at the LHC in 2012. The total integrated luminosity of the dataset corresponds to  $20.2 \text{ fb}^{-1}$ . Different MC simulations are employed, to model signal and background processes, to create templates and to evaluate systematic uncertainties. Single-top quark as well as  $t\bar{t}$  processes are generated using POWHEG-BOX [59–61] with the CT10 [62] parton distribution function and a top quark mass parameter of 172.5 GeV. For hadronisation and showering the generated events are processed by PYTHIA [63] with the P2011C [64] parameter tune using the CTEQ6L1 [65] PDF set. To construct templates, MC datasets with varied top quark mass parameter, ranging from 165 to 180 GeV in steps of 2.5 GeV, have been utilised<sup>(1)</sup>. The largest background contributions for this analysis originate from  $W^\pm$  and  $Z$  boson processes in association with jets. They are simulated with ALPGEN [67], using the CTEQ6L1 PDF set. The showering and hadronisation is done with PYTHIA adjusted to the P2011C tune. HERWIG [68] with CTEQ6L1 is used to generate Diboson ( $ZZ$ ,  $WW$  and  $WZ$ ) processes, where the AUET2 [69] parameter set has been applied. Additional datasets specifically used to evaluate the impact of systematic uncertainties are described in Chapter 7. To account for additional proton-proton interactions, simulated pile-up events are added to the generated processes. Those events are reweighted to match the pile-up profile measured in data. After the MC generation step, all events are passed through a full simulation of the ATLAS detector [70] done with GEANT4 [71], and are then processed with the same reconstruction procedure as data. Since the full detector simulation is very computing intensive, some of the datasets used for the evaluation of systematic uncertainties and the single-top quark mass variation samples, have been processed with a simplified shower parametrisation model for the calorimeter [72]. The full list of datasets used in the analysis can be found in Appendix A. In contrast to the other background processes, the impact of QCD multi-jet production is estimated directly from data. Multi-jet events can be falsely selected if they contain either a lepton originating from a heavy flavor hadron decay (non-prompt) or if a jet is wrongly identified as a lepton (fake). To estimate the contribution of the multi-jet background a data-driven matrix method is used, which is described in Chapter 5.

---

<sup>(1)</sup>In case of the single-top t-channel process, ACERMC [66] in combination with the CTEQ6L1 PDF set is used to create the mass variation datasets.



## 5. Event reconstruction and selection

In this chapter the physics object definitions used in the analyses are described and the event selection criteria, applied to reject background processes, are presented.

### 5.1. Physics objects

The analysis considers  $t\bar{t}$  final states, which include ( $b$ -tagged) jets, electrons, muons and missing transverse energy. The physics object definitions follow the official ATLAS recommendations.

#### Jets:

Jets are built from energy deposits in the electromagnetic and hadronic calorimeter. Adjacent calorimeter cells are combined to topological clusters [73], which are the input to the anti-kt jet reconstruction algorithm [74], operated with a radius parameter of  $R = 0.4$ . Topological clusters are calibrated with the local cluster weighting technique, which corrects for the non-compensation of the ATLAS calorimeter. In addition, different calibration procedures are applied to restore the original jet energy [75]. Furthermore, a jet area based pile-up correction procedure is used, to remove energy deposits originating from coincident proton-proton collisions [45]. To ensure that jets originate from the hard scattering process, a cut on the jet vertex fraction (JVF) is introduced. The jet vertex fraction is defined as the sum of transverse momenta ( $p_T$ ) of tracks associated to the jet, compatible with the primary vertex<sup>(1)</sup>, divided by the sum of the  $p_T$  of all tracks attributed to the jet. To suppress jets originating from pile-up processes, jets with  $p_T < 50$  GeV and  $|\eta| < 2.4$ , have to exceed a JVF of 50%. In order to reject jets originating from noise bursts in the calorimeter, LHC beam-gas interactions or cosmic-ray induced showers, jets are required to fulfil distinct quality criteria [76]. In this analysis only jets with  $p_T > 25$  GeV and  $|\eta| < 2.5$  are considered.

#### Electrons:

Electron candidates [77] are reconstructed from energy deposits (clusters) in the electromagnetic calorimeter, if they agree with a well-reconstructed track in the inner detector. Only candidates with a transverse energy of  $E_T > 25$  GeV and  $|\eta_{\text{cluster}}| < 2.47$ , excluding the end-cap barrel transition region,  $1.37 < |\eta_{\text{cluster}}| < 1.52$ , are selected. Electron candidates have to pass tight identification criteria, which includes strict selection cuts on tracking and calorimeter variables, and their longitudinal impact parameter<sup>(2)</sup> has to be smaller than 2 mm. Furthermore, stringent isolation criteria are applied, to further suppress fake electrons arising from misidentified jets as well as non-prompt electrons originating from photon conversions or heavy flavor decays. Isolation means, that additional

<sup>(1)</sup> Since there are multiple vertices reconstructed in an event, the vertex with the highest  $\sum_{\text{track}} p_{T,\text{track}}^2$  and at least five associated tracks with  $p_T > 0.4$  GeV is selected.

<sup>(2)</sup> The impact parameter is calculated with respect to the primary vertex.

energy and momentum deposits in fixed cones around the electron candidates may not exceed  $p_T$ - and  $\eta$ -dependant thresholds. The thresholds are chosen in a way, to allow for an uniform isolation efficiency of 90% in the various  $E_T$  and  $\eta$  regions. Since electrons are also reconstructed as jets in the detector an overlap removal is performed. If there is a reconstructed jet closer than  $\Delta R < 0.2$  to the electron candidate, the jet is removed from the event. Furthermore, if there is another jet, with  $p_T > 25$  GeV and a jet vertex fraction  $JVF > 0.5$ , reconstructed within  $\Delta R < 0.4$  the electron candidate is removed. In addition, also electrons which only satisfy loosened identification criteria are considered in the analysis. They are used to estimate the number of fake and non-prompt electrons, which pass the final event selection.

### Muons:

Muon candidates [78] are build, by combining tracks from the inner detector with track segments measured in the muon spectrometer. After an independent track reconstruction in the ID and MS, muon candidates are constructed by refitting matching tracks, taking into account both detector components, simultaneously. Combined muons are required to have a transverse momentum of  $p_T > 25$  GeV and a pseudorapidity of  $|\eta| < 2.5$ . For muons, the same longitudinal significance restriction as for electrons is applied. In addition, they have to satisfy different quality criteria, like requirements for hits in the transition radiation tracker or number of hits in the ID. Only isolated muons are considered, therefore an isolation variable  $I_{\text{mini}}$  is introduced.  $I_{\text{mini}}$  is defined as the ratio of the sum of the transverse momenta of all tracks in a variable cone around the muon candidate and the transverse momentum of the muon  $p_T^\mu$ , where the cone size is given by  $\Delta R = 10^{\text{GeV}/p_T^\mu}$ . Since muons can originate from decays of heavy flavor hadrons, an overlap removal is performed. The muon candidate is removed, if there is a reconstructed jet within  $\Delta R < 0.4$ , with a transverse momentum of at least 25 GeV and  $JVF > 0.5$ . Muons without any isolation criteria are used, to estimate the background of non-prompt and fake muons, which can originate for example from cosmic muons, punch-through particles or left over heavy flavor decays.

### Missing transverse energy:

The missing transverse energy ( $E_T^{\text{miss}}$ ) [79] is calculated as the vectorial sum of the transverse components of calorimeter energy deposits. To account also for muons in an event, their transverse momentum is included in the calculation. Energy contributions are calibrated in the same way as the physics objects they are associated to. Deposits not related to high  $p_T$  objects, like electrons, muons or jets, are calibrated with the local cluster weighting technique.

### Flavor tagging:

Jets containing  $b$ -hadrons can be tagged by taking advantage of  $b$ -hadron characteristics, like their high invariant mass, their long life time and their large branching fraction to leptons. In this analysis the multi-variate MV1 [80] tagger is employed, which identifies  $b$ -jets by combining the outputs of different  $b$ -tagging algorithms with a neural network. The MV1 algorithm is operated such, that a jet originating from a  $b$  quark is identified with an efficiency of 70%, while only one out of about 140 light-flavour-jets is wrongly tagged as a  $b$ -jet. These efficiencies have been derived from dileptonic  $t\bar{t}$  events. To account for small discrepancies between the  $b$ -tagging performance in data and MC simulations,  $p_T$ - and  $\eta$ -dependant scale factors are applied.

## 5.2. Event selection

If  $|V_{tb}| = 1$  is assumed, which means that the top quark decays exclusively into a  $W$  boson and a bottom quark, the  $t\bar{t}$  lepton+jets final state is characterised by one charged lepton<sup>(3)</sup>, one neutrino and four jets originating from bottom and light quarks, respectively. To pick such events, multiple selection criteria have been applied. Depending on the charged lepton flavor, the events are split in two categories, the electron and the muon channel. The first part of the event selection consists of the trigger system. Only events, in which a single-electron or single-muon trigger has fired, are selected. The analysis uses the lowest unprescaled triggers available in the 2012 data taking period, which are EF\_e24vhi\_medium1 in the electron and EF\_mu24i\_tight in the muon case. Both triggers apply isolation criteria, which cause inefficiencies for high energetic leptons. The efficiency is recovered, by a disjunction of the low  $p_T$  triggers with higher  $p_T$  threshold triggers without any isolation criteria, named EF\_e60\_medium and EF\_mu36\_tight, respectively. To guarantee data quality, only data events listed in the so called good runs list (cf. Appendix A) are selected, which ensures a fully operational detector at the time of data taking. To reject non-collisional background events, in every event a primary vertex with at least four tracks, exceeding a  $p_T$  of 400 MeV each, has to be reconstructed, in order to be considered in the analysis. To specifically select  $t\bar{t}$  lepton+jets events, the following selection criteria, as recommended by ATLAS, are applied:

- to account for the high-energetic lepton from the  $W$  boson decay, exactly one electron or muon with  $p_T \geq 30$  GeV, which has been matched to the trigger object, is required
- to account for the quarks originating from the  $t\bar{t}$  decay, at least four jets with  $p_T \geq 30$  GeV, at least two of them  $b$ -tagged, have to be reconstructed in an event
- to account for the undetected neutrino, a missing transverse energy larger than 30 (20) GeV<sup>(4)</sup> in the electron (muon) channel, is required
- to account for the leptonically decaying  $W$  boson, only events with a transverse  $W$  boson mass<sup>(5)</sup>  $m_T^W$  of at least 30 GeV in the electron and  $m_T^W + E_T^{\text{miss}} \geq 60$  GeV<sup>(4)</sup> in the muon channel are selected

Since high energetic gluon radiations are not well modelled in MC simulations, an additional cut on the  $p_T$  of the 5<sup>th</sup> leading jet<sup>(6)</sup> is applied to reject events with additional high momentum jets. Therefore, in events with more than four jets, the  $p_T$  of the 5<sup>th</sup> jet may not exceed 40 GeV. As shown in Appendix E an additional requirement on the angular distance between two jets  $\Delta R_{jj}$  can significantly reduce the impact of systematic effects on the measured top quark mass. Thus the minimum distance between any two jets in an event  $\Delta R_{jj}$  has to exceed 1.1, in order to pass the event selection.

To estimate the contribution of fake and non-prompt lepton backgrounds, a data-driven matrix method

<sup>(3)</sup>Because of the rather short life-time of  $\tau$ -leptons, only electrons and muons are considered in this analysis.

<sup>(4)</sup>The separate cut values for the two channels originate from the different fake probabilities for electrons and muons.

<sup>(5)</sup>Due to the missing  $z$ -component of the neutrino momentum the invariant mass of the  $W$  boson can not be calculated, instead the transverse mass, defined as  $m_T^W = \sqrt{E_T^{\text{miss}} p_T^{e/\mu} (1 - \cos(\Delta\phi(e/\mu, E_T^{\text{miss}})))}$  is used.

<sup>(6)</sup>The jets in an event are ordered by their transverse momentum from highest to lowest  $p_T$ . Since one expects four high energetic jets from the  $t\bar{t}$  decay, the 5<sup>th</sup> leading jet is likely to originate from gluon radiation.

Process	Electron channel	Muon channel
$t\bar{t}$ signal	$10\,636 \pm 30$	$16\,357 \pm 38$
Single-top signal	$504 \pm 15$	$771 \pm 19$
$W$ +jets	$196 \pm 15$	$382 \pm 24$
$Z$ +jets	$13 \pm 4$	$4 \pm 2$
$WW/WZ/ZZ$	$4 \pm 1$	$8 \pm 1$
Fake leptons	$50 \pm 14$	$48 \pm 12$
Total expected	$11\,403 \pm 39$	$17\,571 \pm 50$
Data	12141	18463

Table 5.1.: Event yields, after all selection criteria have been applied. The expected contributions have been scaled to match the data luminosity of  $20.2 \text{ fb}^{-1}$ . Figures given in the table have been rounded to the next whole number and the uncertainties correspond to statistical uncertainties, only.

is used [81]. The number of fake leptons<sup>(7)</sup> passing the tight lepton selection criteria  $N_{\text{fake}}^{\text{tight}}$  can be estimated from the number of loose  $N^{\text{loose}}$  and tight leptons  $N^{\text{tight}}$  with

$$N_{\text{fake}}^{\text{tight}} = \frac{\epsilon_{\text{fake}}}{\epsilon_{\text{real}} - \epsilon_{\text{fake}}} (\epsilon_{\text{real}} N^{\text{loose}} - N^{\text{tight}}) \quad (5.1)$$

where  $\epsilon_{\text{fake}} / \epsilon_{\text{real}}$  denote the probabilities for a fake / real lepton to pass the tight selection criteria. These lepton efficiencies depend on the event characteristics, like e.g. the lepton and jet transverse momenta, and are derived from dedicated event samples, with large fractions of fake leptons. To estimate the contribution of fake lepton background, a weighing factor

$$w = \frac{\epsilon_{\text{fake}}}{\epsilon_{\text{real}} - \epsilon_{\text{fake}}} (\epsilon_{\text{real}} - \delta) \quad (5.2)$$

is applied to each event, in which  $\delta = 1$  if the event passes the tight selection, and  $\delta = 0$  otherwise. The final event yields, after all event selection criteria have been applied, are given in Table 5.1. Since the expected number of signal events depends on the actual top quark mass, a mass of  $172.5 \text{ GeV}$  is assumed for the numbers quoted. Therefore the slightly higher number of events in data compared to the MC prediction indicates a smaller  $m_{\text{top}}$  value than  $172.5 \text{ GeV}$ . The minor contribution from non-top quark processes, after the final selection, is taken into account by bin-wise subtracting the estimated number of background events from the measured electron and muon  $p_T$  distributions.

### 5.3. Data and MC distributions

In this chapter some data to MC comparison plots are shown for a top quark mass of  $172.5 \text{ GeV}$ , after the final event selection has been applied. The jet multiplicity, the missing transverse energy and the angular separation between jets are shown in Fig. 5.1. Figures 5.2 and 5.3 present the kinematic distributions of jets and  $b$ -tagged jets, respectively, while the kinematic distributions for electrons and muons are illustrated in Fig. 5.4. The same plots, but for a top quark mass of  $167.5 \text{ GeV}$ , are given in Appendix B.

<sup>(7)</sup>For better readability, the term fake leptons denotes both fake and non-prompt leptons.

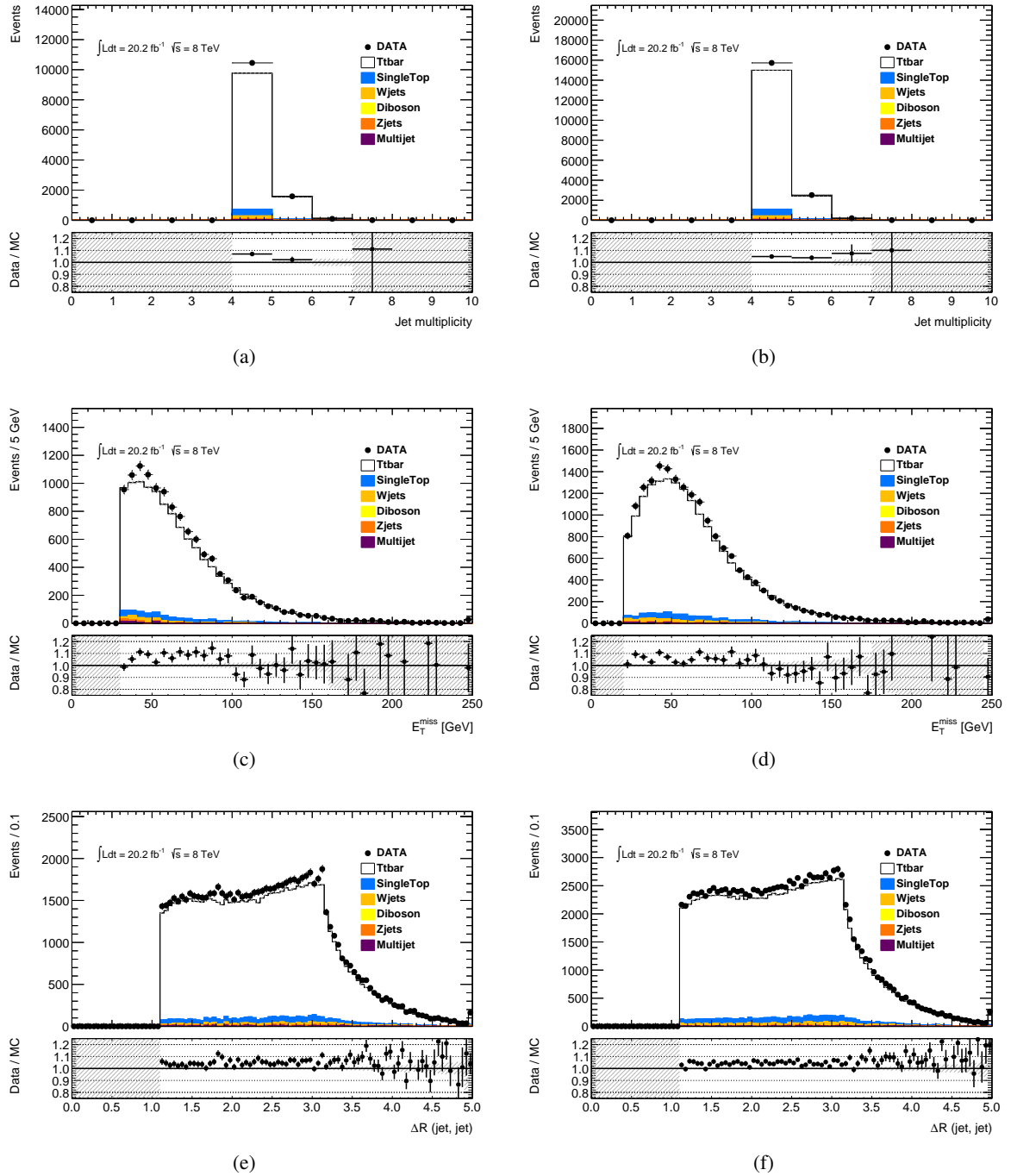


Figure 5.1.: Distributions for the selected events, in the electron channel on the left and in the muon channel on the right hand side, are presented. Figure (a) and (b) show the jet multiplicities, while Fig. (c) and Fig. (d) illustrate the  $E_T^{\text{miss}}$  distributions. The  $\Delta R_{jj}$  distributions are presented in Fig.(e) and Fig.(f). The data are plotted as black points with their respective statistical error. In addition, the expected contributions of the relevant physics processes, colour coded according to the legend, are indicated. For the  $t\bar{t}$  and single-top signal processes a top quark mass of 172.5 GeV is assumed.

## 5. Event reconstruction and selection

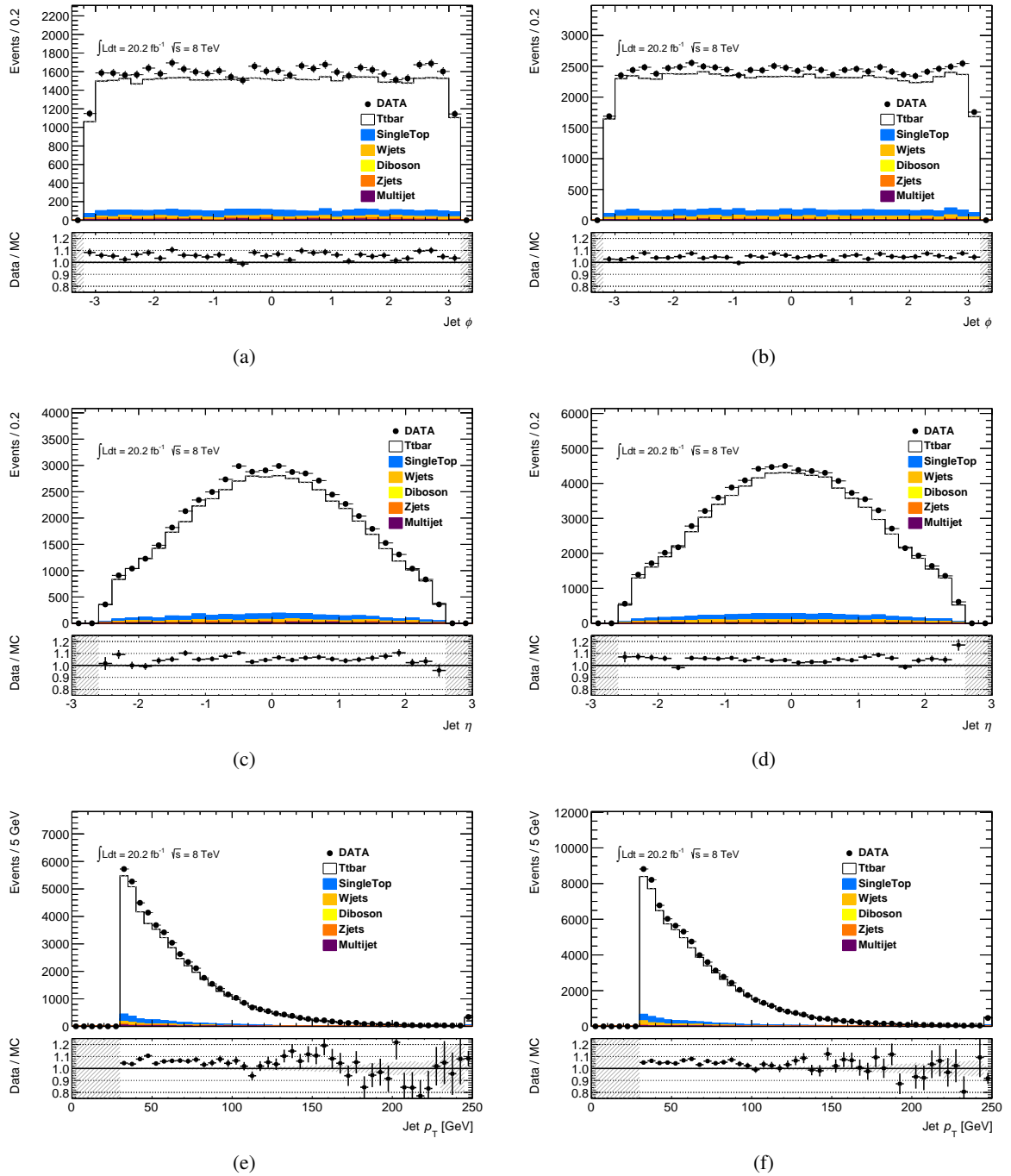


Figure 5.2.: Distributions for the selected events, in the electron channel on the left and in the muon channel on the right hand side, are presented. Figures (a) and (b) show the  $\phi$  distributions of the jets, while Fig. (c) and Fig. (d) illustrate their  $\eta$  distributions. The jet transverse momenta are presented in Fig. (e) and Fig. (f). The data are plotted as black points with their respective statistical error. In addition, the expected contributions of the relevant physics processes, colour coded according to the legend, are indicated. For the  $t\bar{t}$  and single-top signal processes a top quark mass of  $172.5 \text{ GeV}$  is assumed.

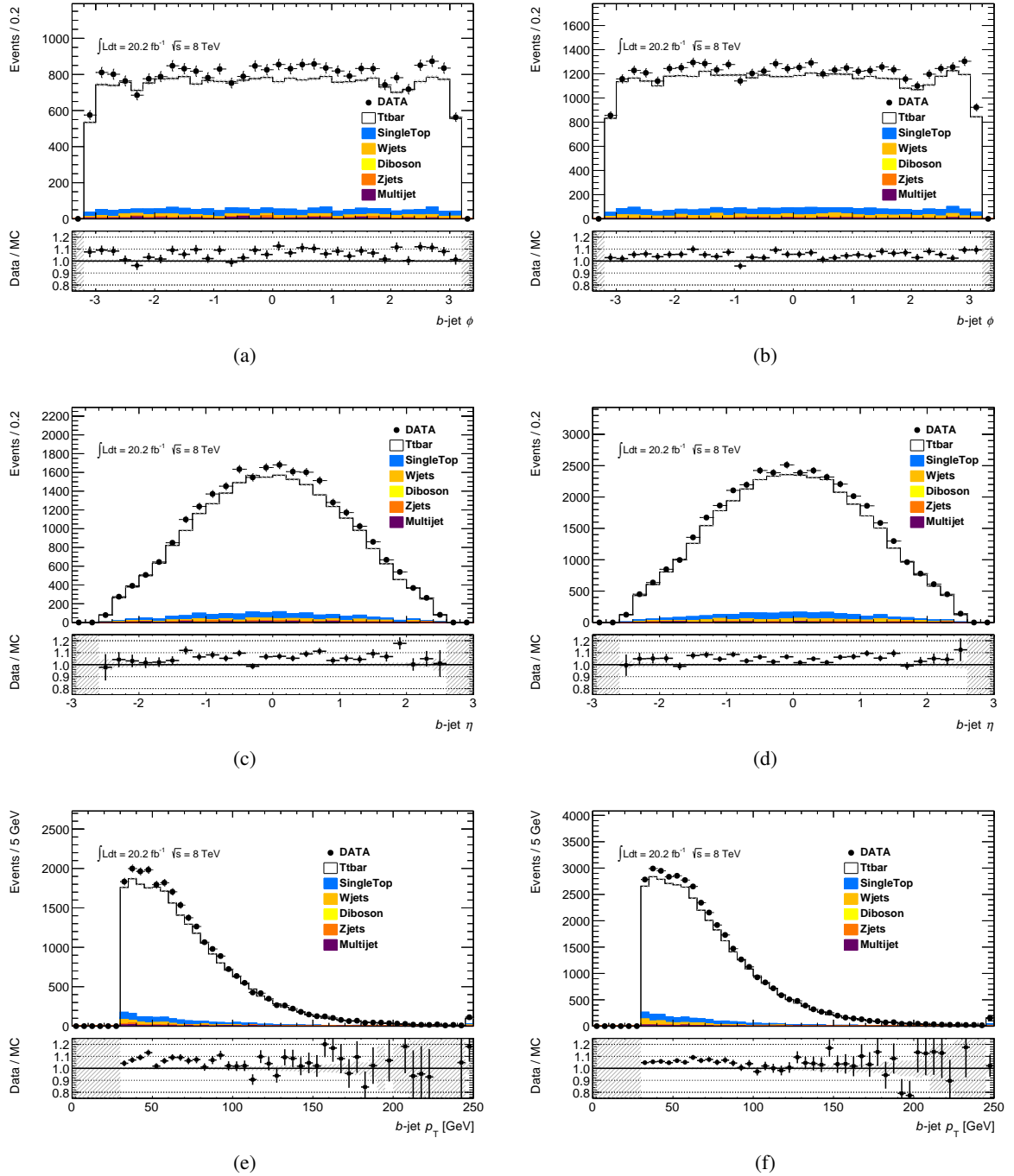


Figure 5.3.: Distributions for the selected events, in the electron channel on the left and in the muon channel on the right hand side, are presented. Figures (a) and (b) show the  $\phi$  distributions of the  $b$ -tagged jets, while Fig. (c) and Fig. (d) illustrate their  $\eta$  distributions. The transverse momenta of  $b$ -tagged jets are presented in Fig. (e) and Fig. (f). The data are plotted as black points with their respective statistical error. In addition, the expected contributions of the relevant physics processes, colour coded according to the legend, are indicated. For the  $t\bar{t}$  and single-top signal processes a top quark mass of 172.5 GeV is assumed.

## 5. Event reconstruction and selection

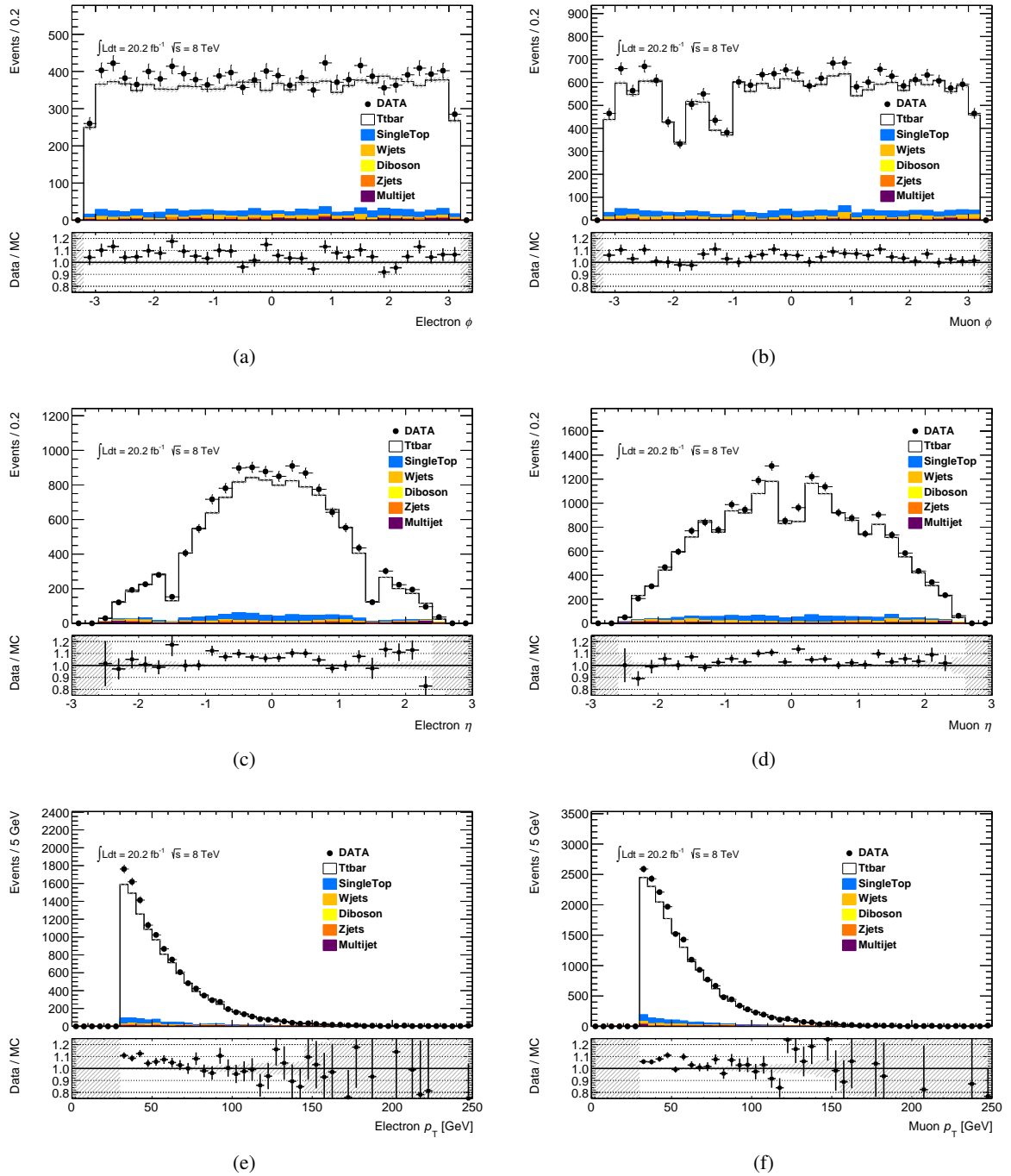


Figure 5.4.: Distributions for the selected events, in the electron channel on the left and in the muon channel on the right hand side, are presented. Figures (a) and (b) show the  $\phi$  distributions of the leptons, while Fig. (c) and Fig. (d) illustrate their  $\eta$  distributions. The lepton transverse momenta are presented in Fig. (e) and Fig. (f). The data are plotted as black points with their respective statistical error. In addition, the expected contributions of the relevant physics processes, colour coded according to the legend, are indicated. For the  $t\bar{t}$  and single-top signal processes a top quark mass of 172.5 GeV is assumed.

## 6. Template fit

This chapter describes the template method used to extract the top quark mass from the electron and muon  $p_T$  distributions. First the method itself is motivated, while second the parametrisation of the lepton  $p_T$  is introduced. The derivation of the templates from the different mass-value MC signal samples are described and the procedure of extracting  $m_{\text{top}}$  from data is detailed. Finally the closure tests, which are performed to verify the validity of the method, are presented.

A template is designed to extract an underlying variable from a given observable. MC simulations are created for different values of this variable and the dependence of the resulting observable is parametrised as a function of it. This parametrisation, the template, is then fitted to the distribution measured in data, to determine the variable. In this analysis the lepton  $p_T$  distributions are used to extract the top quark mass. Therefore the lepton transverse momenta, which are shown in Fig. 5.4(e) and 5.4(f), are parametrised with a modified Novosibirsk function [82]. The Novosibirsk function is basically an asymmetric Gaussian distribution, suitable to describe Gaussian shaped peaks with a large tail to one side. Its functional form is given by

$$f(x) = N \cdot \exp \left( -\frac{1}{2} \cdot \left( \frac{\ln \left( 1 + \tau \cdot (x - \mu) \frac{\sinh(\tau\sqrt{\ln 4})}{\sigma\tau\sqrt{\ln 4}} \right)}{\tau} \right)^2 + \tau^2 \right) \quad (6.1)$$

where  $N$  denotes the overall normalisation,  $\mu$  and  $\sigma$  represent the mean and the width parameters, and  $\tau$  controls the asymmetry of the function. The fits of the Novosibirsk function to the nominal MC signal electron and muon  $p_T$  distributions are shown in Fig. 6.1(a) and Fig. 6.1(b). To construct the template the other mass-value MC samples, which vary only in their top quark mass parameter, are fitted as well (the corresponding plots can be found in Appendix C). The dependence of the fitted Novosibirsk parameters on the top quark mass is shown in Fig. 6.2. Under the assumption that the parameters depend linearly on  $m_{\text{top}}$ , each parameter is fitted with a first order polynomial. Since the normalisation parameters are barely sensitive to  $m_{\text{top}}$ , they are fixed to 0.15 in the electron and to 0.12 in the muon channel.<sup>(1)</sup> The asymmetry parameter in the electron channel only marginally depends on  $m_{\text{top}}$ , as well. However, since the parameter shows some sensitivity in the muon channel, for consistency reasons between the two channels, the asymmetries are not fixed. The results of these fits are used as initial values for a combined fit. The combined fit is designed to fit the linear dependence of the Novosibirsk parameters on the top quark mass. Therefore, all lepton  $p_T$  distributions of the different mass-value samples are taken into account in a single fit<sup>(2)</sup>, in order to extract the slope and y-intercept for each parameter. The result of this fit is shown in Fig. 6.1(c), Fig. 6.1(d) and in Fig. 6.2. The individual slope and intercept values as well as additional plots are stated in Appendix C. Since in

<sup>(1)</sup>These numbers are selected, since they give the lowest  $\chi^2/\text{ndf}$  value in the simultaneous fit.

<sup>(2)</sup>The nominal approach in this analysis is to combine the electron and muon channel to obtain a single value for the measured top quark mass. However, the measurement has also been performed by taking into account the two lepton channels separately, which yields a measured top quark mass for each channel. The corresponding plots can be found in Appendix C.

## 6. Template fit

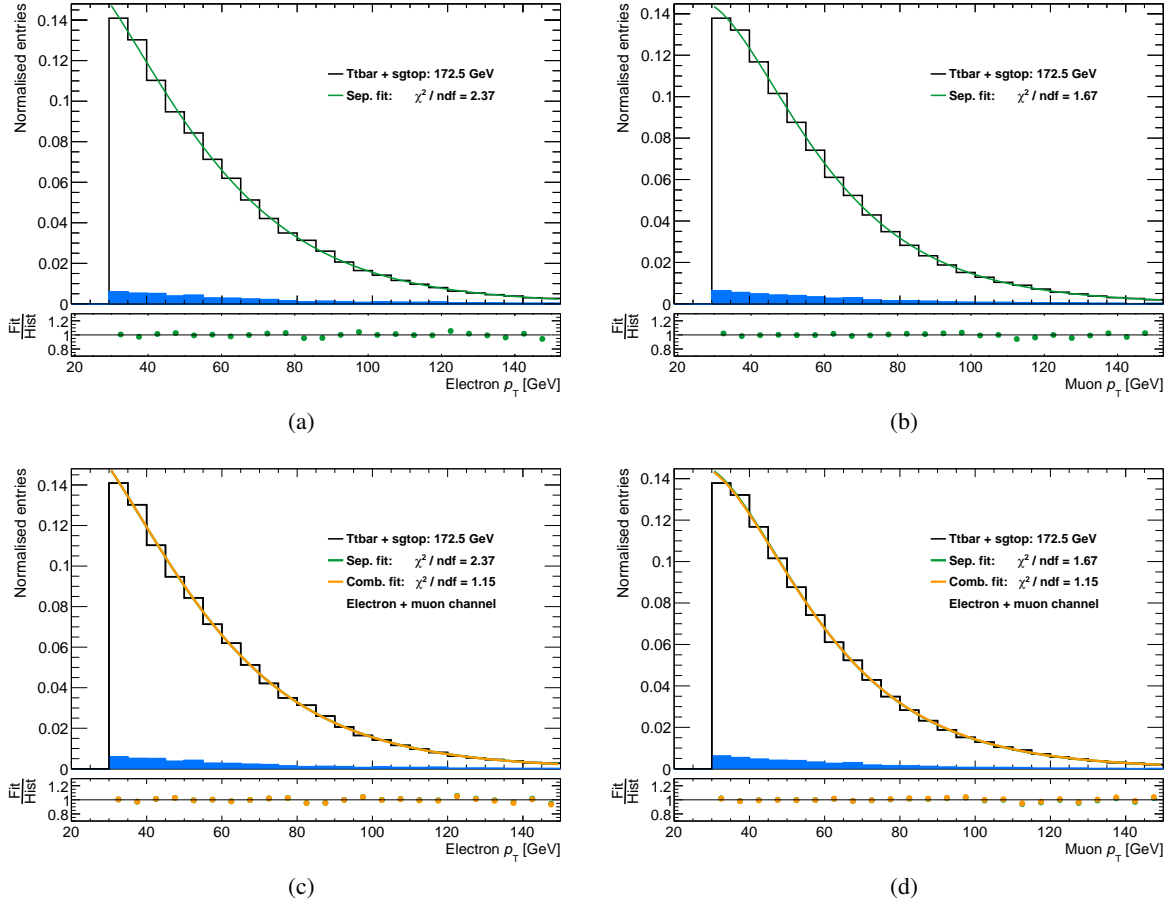


Figure 6.1.: Fits to the lepton  $p_T$  distributions for a top quark mass parameter of 172.5 GeV. In the analysis the  $t\bar{t}$  (shown in white) as well as the single-top process (marked in blue) are considered signal and therefore both are used for the template derivation. Figures (a) and (b) show the fit with the Novosibirsk function to the electron and muon  $p_T$  signal distributions. Figures (c) and (d) also include the combined fit, marked in orange, which assumes a linear fit parameter variation with  $m_{\text{top}}$ . The corresponding  $\chi^2/\text{ndf}$  values are given in the legend. The plots have been normalised to unity.

the combined fit all Novosibirsk parameters are solely dependent on  $m_{\text{top}}$ , the top quark mass entirely controls the shape of the Novosibirsk function. By fitting the template, which is nothing else than the Novosibirsk function with its parameters linearly parametrised by the top quark mass, to the lepton  $p_T$  distributions measured in data, the underlying value of  $m_{\text{top}}$  can be determined. The behaviour of the template for different top quark masses is shown in Fig. 6.3.

The actual value of the top quark mass from a given distribution is extracted with a binned likelihood fit. For the number of events in a given bin, a Poisson distribution is assumed. It is given by

$$\mathcal{L}(\text{lep}_{\text{pt}} | m_{\text{top}}, N_{\text{el}}, N_{\text{mu}}) = \prod_j^{\text{bins}} \left( \frac{\lambda_j^{N_{\text{obs},j}}}{N_{\text{obs},j}!} \right) \cdot \exp(-\lambda_j) \quad (6.2)$$

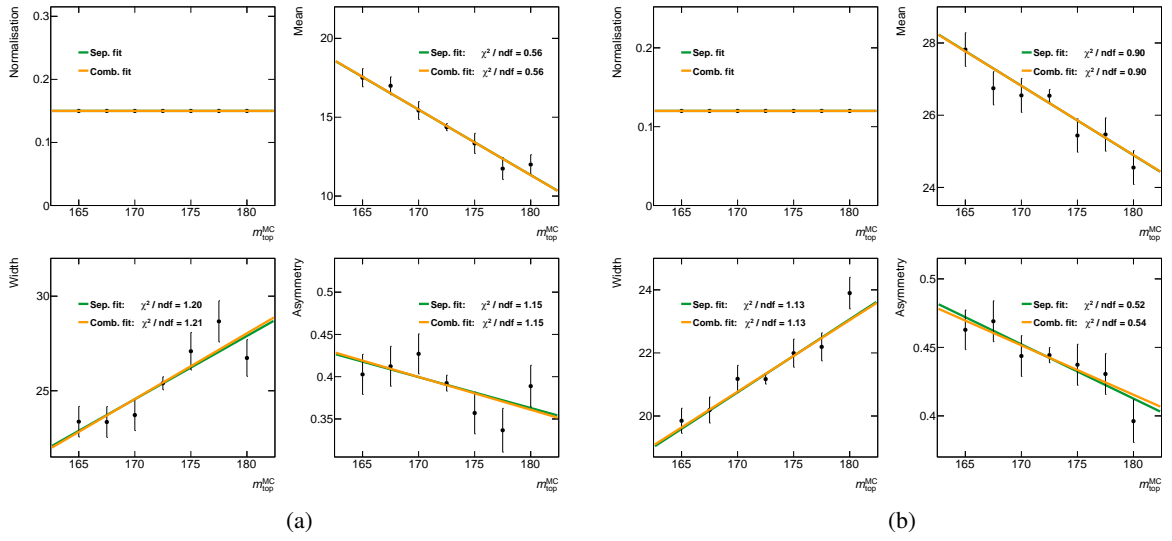


Figure 6.2.: The four parameters of the Novosibirsk function as a function of the top quark mass. The parameters are obtained by fitting a Novosibirsk function to the lepton  $p_T$  distributions of each mass-value MC with the top quark mass parameter ranging from 165 to 180 GeV. Fig. (a) shows the parameter dependencies in the electron and Fig. (b) in the muon channel. In both channels the overall normalisation parameter has been fixed. The first order polynomial fits to the parameter distributions are shown in green, while the combined fit, which is done by taking into account the electron and muon channels simultaneously, is shown in orange.

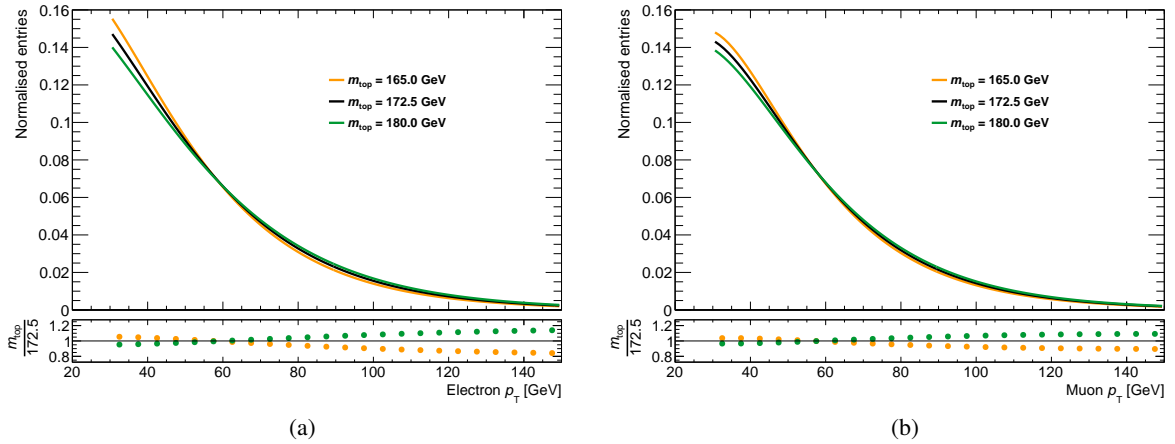


Figure 6.3.: Template shapes for three different values of the top quark mass, 165, 172.5 and 180 GeV. The template for the electron channel is shown in Fig. (a) and the template for the muon channel is presented in Fig. (b). The plots have been normalised to unity. The ratios show the difference in the template predictions for a top quark mass of 165 and 180 GeV, with respect to the nominal mass of 172.5 GeV.

## 6. Template fit

where,  $N_{\text{obs}, j}$  denotes the number of observed and  $\lambda_j$  the number of expected events, in bin  $j$ . Since  $\lambda_j$  is predicted by the template, the only free parameters are the fitted top quark mass  $m_{\text{top}}$ , as well as the overall normalisation factors in the electron and muon channel,  $N_{\text{el}}$  and  $N_{\text{mu}}$ . The result of applying the binned likelihood fit to the lepton  $p_{\text{T}}$  distribution of the signal MC sample is shown in Fig. 6.4. To verify the method and to check for any biases introduced in the extraction of  $m_{\text{top}}$ , pseudo ex-

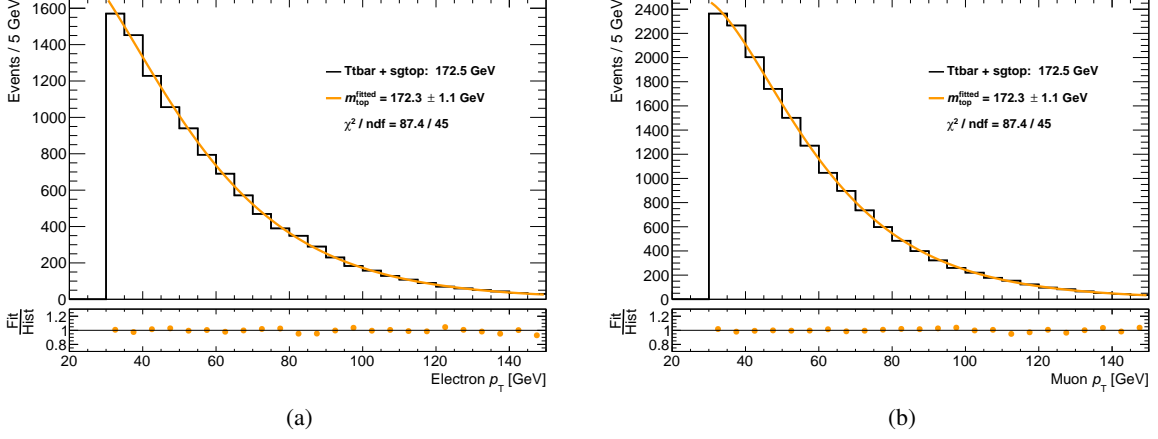


Figure 6.4.: Template fit to the 172.5 GeV signal MC distribution. The histograms show the combination of the signal  $t\bar{t}$  and single-top processes. The template fit in the electron channel is presented in Fig. (a) and the fit in the muon channel is shown in Fig. (b). The fit result with the corresponding statistical error and the  $\chi^2/\text{ndf}$  value are given in the legend.

periments are performed. A pseudo experiment consists of fake distributions obtained by drawing randomly as many events from a given MC sample as are expected in data<sup>(3)</sup>. To account for statistical fluctuations in the measurement, the number of events drawn is Poisson fluctuated around the number of events expected in data. The resulting lepton  $p_{\text{T}}$  distributions are fitted with the template, which returns a ‘measured’ top quark mass for the pseudo experiment. This procedure is repeated 5000 times and for each pseudo experiment, the fitted top quark mass, the corresponding error  $\delta m_{\text{top}}^{\text{fitted}}$  and the pull value, defined as

$$\text{pull} = \frac{m_{\text{top}}^{\text{fitted}} - m_{\text{top}}^{\text{MC}}}{\delta m_{\text{top}}^{\text{fitted}}} \quad (6.3)$$

where  $m_{\text{top}}^{\text{MC}}$  denotes the MC top quark mass parameter, are extracted. Each of these three distributions is Gaussian-shaped and fitted accordingly, resulting in a fitted mean value for each distribution. This procedure is repeated for each MC mass-value, with the results shown in Fig. 6.5. The pull distribution is used to check if there occur any systematical shifts in the course of the measurement. If the measurement is unbiased the fitted mean of the pull distribution is consistent with zero and its width equals unity if the error is estimated correctly. Since the number of events drawn for all pseudo experiments exceeds the number of available MC events by far, an oversampling correction is applied [83]. The fit of a constant function to the mean of the pull distribution, which is shown in Fig. 6.5(c), reveals a consistent shift towards larger masses. The actual shift for  $m_{\text{top}}$  amounts to  $0.50 \pm 0.40$  GeV (cf. Fig. 6.5(a)) and is taken into account in the measurement accordingly. However, since the fitted width

<sup>(3)</sup>The pseudo experiments can also be drawn from the template itself, the result of this approach is presented in Appendix C.

of the pull distribution (cf. Fig 6.5(d)) is compatible with one, the estimation of the statistical error, which is shown in Fig. 6.5(b) as a function of the fitted top quark mass, is reliable.

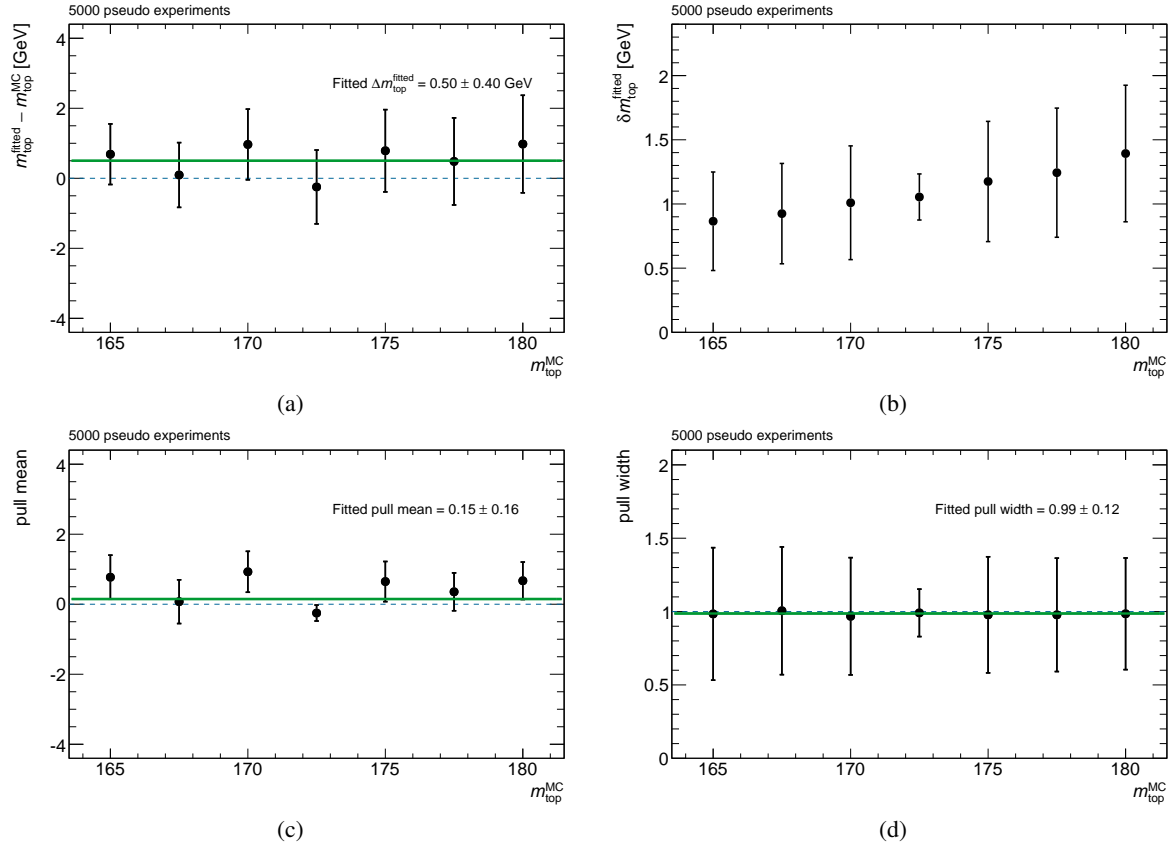


Figure 6.5.: Results of pseudo experiments for the different mass-value MC with the top quark mass parameter ranging from 165 to 180 GeV. The plots are obtained by fitting the results of 5000 pseudo experiments for each mass-value with a Gaussian function. Fig. (a) shows the mean of the fitted top quark mass distribution subtracted by the underlying MC top quark mass parameter, while Fig. (b) and Fig. (c) present the statistical error on the fitted top quark mass and the mean of the pull distributions, respectively. The fitted width of the pull distribution is shown in Fig. (d). The results of constant fits to each of the distributions presented in Fig. (a), Fig. (c) and Fig. (d) are shown in green and the corresponding  $\chi^2/\text{ndf}$  values are given in the legend.



## 7. Uncertainty estimation

This chapter details the different sources of uncertainties studied for the analysis, which can be divided in different categories, the statistical uncertainty, related to the finite amount of data available, the uncertainty on the method calibration, the modelling uncertainties, the background estimation uncertainties and the uncertainties related to the detector itself. An overview of the different contributions to the overall precision of the measured top quark mass is presented in Table 7.1.

To evaluate the uncertainty on the measured top quark mass due to systematic influences, for each uncertainty a total of 5000 pseudo experiments, as described in Chapter 6, are performed. The uncertainties are estimated either with the same MC events as used in the nominal analysis, by just varying the systematic value under study by  $\pm 1\sigma$ , or by different MC events, produced with changed MC parameter(s). In either case the analysis is repeated on the resulting datasets, and the difference in the measured top quark mass between the nominal and the varied datasets is quoted as the systematic uncertainty. If a systematic consists of an up and down variation instead, the uncertainty is calculated as half of the absolute difference between those two. If the up and down variation have the same sign, the larger of the variations is used as systematic. The overall uncertainty on the measured top quark mass is given as the square root of the sum of squares of the different uncertainty components. In addition to the systematic uncertainties themselves, also the statistical precision of each systematic  $\sigma_{\text{stat}}$  is estimated (cf. [84]). It is derived as

$$\sigma_{\text{stat}} = \sqrt{\sigma_1^2 + \sigma_2^2 - 2\rho_{12} \sigma_1 \sigma_2} \quad (7.1)$$

where  $\sigma_1$  and  $\sigma_2$  denote the error on the Gaussian mean in the pseudo experiments for the nominal and varied dataset, and  $\rho_{12}$  is the correlation between the two samples. The correlation can be calculated from the total number of events in the nominal and varied dataset  $N_1$  and  $N_2$  and the number of events present in both samples  $N_{12}$ , with  $\rho_{12} = N_{12}/\sqrt{N_1 N_2}$ . Therefore, in cases where a variation in the nominal dataset is used to estimate a systematic uncertainty, where  $N_{12}$  is usually high, the resulting statistical uncertainty on the particular systematic is small, while in cases, where different MC datasets are used, the statistical precision is lower.

### 7.1. Statistics and method calibration

The statistical precision on the top quark mass is determined with the pseudo experiments described in Chapter 6. By conducting 5000 pseudo experiments the spread of  $m_{\text{top}}$  is assessed with a fit of a Gaussian function. The fitted width of the distribution determines the statistical uncertainty, which is 0.94 GeV in this analysis. In a similar way the uncertainty on the method used to extract the top quark mass is evaluated. As described, pseudo experiments are performed for the different MC top quark mass parameters, revealing an average shift in  $m_{\text{top}}$  (cf. Fig. 6.5(a)). The error on this shift is used as uncertainty for the method calibration and amounts to 0.40 GeV.

Uncertainty	$\Delta m_{\text{top}}$ [GeV]	Up [GeV]	Down [GeV]
Statistics	0.94		symmetric
Method calibration	0.40		symmetric
Signal MC generator	$0.62 \pm 0.01$		symmetric
Single-top Wt generator	$0.28 \pm 0.00$		symmetric
Hadronisation	$0.55 \pm 0.01$		symmetric
ISR and FSR	$1.39 \pm 0.01$		symmetric
Underlying Event	$0.67 \pm 0.01$		symmetric
Colour Reconnection	$0.23 \pm 0.01$		symmetric
Parton distribution function	$0.42 \pm 0.01$		symmetric
Single-top contribution	$0.10 \pm 0.00$	0.09	-0.10
Background contribution	$0.69 \pm 0.00$	0.69	-0.68
Leptons	$0.50 \pm 0.00$	0.48	-0.52
$E_{\text{T}}^{\text{miss}}$	$0.12 \pm 0.00$	0.11	-0.13
$b$ -tagging	$0.08 \pm 0.00$	0.08	-0.08
Jet energy resolution	$0.32 \pm 0.00$	0.34	-0.13
Jet energy scale	$0.60 \pm 0.00$	0.62	-0.55
Jet reconstruction efficiency	$0.00 \pm 0.00$		symmetric
Jet vertex fraction	$0.05 \pm 0.00$	0.04	-0.05
Total	$2.37 \pm 0.04$	2.38	2.35

Table 7.1.: Summary of the uncertainties evaluated in the analysis, where applicable the up and down variations are given. The uncertainties are calculated by building the average of the absolute difference of the up and down variation. For components without an up and down variation, the difference to the nominal value is quoted. If the up and down variation have the same sign, the larger of the variations is used as systematic. The total uncertainty is calculated as the sum of squares of the individual components. In addition, the statistical precision of the systematic uncertainties, scaled by the square root of the total number of pseudo experiments conducted, is quoted.

## 7.2. Modelling uncertainties

To estimate the influence of different choices and parameters in the MC simulations, different MC samples are compared to each other or, where applicable, to the nominal dataset.

### Signal MC generator

To evaluate the uncertainty due to the choice of different signal MC generators for the  $t\bar{t}$  process the nominal POWHEG event generator is compared to MC@NLO [85, 86]. The modelling of the parton shower, hadronisation and underlying event for both generators is done with the HERWIG program using the AUET2 tune. The full difference between the two generators yields an uncertainty of 0.62 GeV on the measured top quark mass.

### Single-top $Wt$ generator

With about 65%, the  $Wt$  associated production is the largest contributor to the single-top signal fraction. To investigate the systematic uncertainty originating from this process, the difference between the diagram removal (DR) and the diagram subtraction (DS) NLO calculation schemes [87] is evaluated. Therefore a POWHEG+PYTHIA dataset which uses the DS scheme is compared with the nominal  $Wt$  MC sample using the DR scheme. The resulting uncertainty calculated as the full difference between the two approaches is 0.28 GeV.

### Hadronisation

Different models exist to describe the hadronisation process. Since one can not decide from first principles which model is better suited to describe nature, two models are compared to determine their influence on the resulting top quark mass. Therefore, the Lund String model [88, 89] as it is implemented in PYTHIA is compared to the cluster fragmentation model [90] used in HERWIG. The two programs also differ in other choices, like the parton shower ordering, matching scales and fragmentation functions. To determine the overall uncertainty due to the hadronisation model, events are generated with the POWHEG generator and then passed either to PYTHIA using the P2011C or to HERWIG with the AUET2 tune. The full difference between the two approaches amounts to 0.55 GeV in the resulting top quark mass.

### Initial and final state radiation

In order to estimate the effects of a change in the amount of initial and final state radiation (ISR/FSR) on the measured top quark mass, different parameters like  $\Lambda_{\text{QCD}}$  and  $h_{\text{damp}}$  [91], have been varied in the POWHEG+PYTHIA simulation with the P2012 tune [64], to allow for an increase or decrease in QCD radiation. The resulting uncertainty calculated as half of the difference between the two samples, is estimated to be 1.39 GeV and is therefore the single largest contribution to the uncertainty on the top quark mass in this analysis.

## Underlying event

The underlying event (UE) refers to processes contributing to an event except for the hard scattering itself. It is mainly comprised of soft and semi-hard multiple parton interactions and the amount of the contribution can be varied in the MC simulation. To assess the influence of different underlying event models the Perugia parameter tunes P2012 and P2012MPIHI are compared [64]. For this comparison the same partonic events created with POWHEG+PYTHIA are used. The full difference between the two models is taken as uncertainty and is estimated to be 0.67 GeV.

## Colour reconnection

The specific model of the colour reconnection (CR) may influence the final result. Since the strength of the colour flow can be tuned in the MC simulation, the impact on the measured top quark mass is estimated by comparing a model with reduced colour reconnection strength to the nominal one. Therefore events are simulated with POWHEG+PYTHIA using either the P2012 or the P2012LOCR tune [64]. The full difference between the two approaches is 0.23 GeV and is taken as systematic uncertainty on the CR model.

## Parton distribution function

To estimate the uncertainty originating in the choice of the parton distribution function (PDF) the recommendations of the TOP4LHC working group are followed [92]. Therefore the envelop of the CT10, MSTW2008 [35] and NNPDF2.3 [93] parton distribution functions is build at 68% level and the largest up and down variations are taken into account as uncertainties. Since the required information are not available in the nominal  $t\bar{t}$  and single-top MC simulations, the MC datasets detailed in Appendix A are used instead. The overall uncertainty due to the PDF is calculated as half of the difference between the up and down variations and is estimated to be 0.42 GeV.

### 7.3. Non $t\bar{t}$ contributions

With roughly 93% the  $t\bar{t}$  process is by far the largest contributor after the final event selection. Nevertheless other physics processes contribute as well, and their influence on the determination of the top quark mass is studied. A variation of the single-top  $t$ -,  $s$ - and  $Wt$ -production cross sections by  $\pm 15\%$  causes a shift of 0.10 GeV, while a variation of the remaining background contributions by  $\pm 50\%$  results in a shift of 0.69 GeV. These numbers are taken as the systematic uncertainties for the single-top and background contribution, respectively.

### 7.4. Detector modelling

Measurements by the detector have an intrinsic uncertainty. The uncertainty related to the different objects measured in the detector are described here. The nominal value is varied according to its estimated uncertainty by  $\pm 1\sigma$  and the uncertainty on the measured top quark mass is taken as half of the difference of the up and down variation. In cases, in which the differences between the up/down

variation and the nominal value have the same sign, the larger of the two differences is taken as systematic uncertainty. If there is no up and down variation for a systematic uncertainty the difference between the nominal and the variation is used. The evaluation of the detector uncertainties has been conducted simultaneously for both signal as well as background processes.

## Lepton systematics

The uncertainties related to electrons and muons, comprise the uncertainties on the energy scale, the energy resolution as well as on the trigger and reconstruction efficiencies for the two lepton flavors. These components have been studied in leptonic  $J/\psi$  and  $Z$  data events [77, 78, 94] and their influence on the top quark mass in the analysis is estimated. A breakdown of the individual items is shown in Table D.1. The overall uncertainty on the measured top quark mass is 0.50 GeV, with the main contribution originating from the electron energy scale.

## $E_T^{\text{miss}}$ systematics

Since the missing transverse energy depends on the other physics objects in an event, its value is recalculated during the estimation of the lepton and jet systematics, accordingly. The influence on the measured value of  $m_{\text{top}}$  is therefore included in the numbers quoted there. In addition the uncertainty due to components in the  $E_T^{\text{miss}}$  calculation, which are not related to physics objects is estimated. Therefore the scale and resolution of the soft term [79] is varied, which results in an overall shift in the measured top quark mass of 0.12 GeV.

## $b$ -tagging systematics

There are small differences between the  $b$ -tagging efficiencies measured in data and MC simulations. To correct for this, scale factors depending on the flavor,  $p_T$  and  $\eta$  values of jets are applied. To estimate the uncertainty on  $m_{\text{top}}$ , the  $b$ -tagging,  $c/\tau$ -tagging and mis-tagging scale factors are varied within their uncertainties. The overall uncertainty is given as the quadratic sum of the individual components and is estimated to be 0.08 GeV.

## Jet energy resolution

The uncertainty due to the jet energy resolution (JER) is obtained by smearing the energies of the jets within their uncertainties and repeating the analysis. The JER is split up in 11 individual components [75], which are taken into account separately. The result of the systematic variations is stated in Table D.2, which in total amounts to an uncertainty on the measured top quark mass of 0.32 GeV.

## Jet energy scale

The jet energy scale (JES) has been calibrated with test beam data and MC simulations. In addition the JES can be improved with in-situ methods, by using the balance of physics objects in the transverse plane [75, 95, 96]. The relative uncertainty on the JES is a function of the  $p_T$  and  $\eta$  of a jet and varies

from about 1% to 4%. The uncertainty can be split up in 26 different components, which have been studied independently to estimate the influence on the measured top quark mass. The corresponding numbers are listed in Table D.3. The overall uncertainty is obtained from the sum of squares of the individual JES components, and is estimated to be 0.60 GeV.

### Jet reconstruction efficiency

To account for minor jet reconstruction inefficiencies for jets with a transverse momentum below 30 GeV, 2% of such jets are randomly dropped from events, and the resulting uncertainty on  $m_{\text{top}}$  is derived. Since the event selection requires at least four jets with  $p_{\text{T}} > 30$  GeV, no effect on the top quark mass could be observed.

### Jet vertex fraction systematics

The uncertainty introduced by the cut on the jet vertex fraction (JVT) is estimated by varying the JVT within its uncertainty. This results in an uncertainty of 0.05 GeV on the measured top quark mass.

By accounting for the various sources of uncertainties the overall precision on the measured top quark mass is estimated to be 2.37 GeV. The influence of different cuts on  $\Delta R_{\text{jj}}$  and the jet multiplicity on the overall precision of  $m_{\text{top}}$  can be found in Appendix E.

## 8. Modelling of the transverse momentum of the top quark

It is a known issue, that the transverse momentum of the top quark is not well modelled in the MC simulations presently available [97]. The main problem is that until recently no next-to-next-to-leading order (NNLO) QCD predictions for differential distributions for the top quark pair production at the LHC were available. With Ref. [98] a complete NNLO calculation has been published, but unfortunately there are no MC generators yet obtainable, which include these new calculations. Since the top quark transverse momentum is directly influencing the lepton  $p_T$ , which is used to extract  $m_{\text{top}}$  in this analysis, the impact on the measured top quark mass is studied, by estimating the influence of NNLO corrections to the NLO MC predictions. Therefore the  $t\bar{t}$  and single-top MC datasets have been reweighted as a function of the transverse momentum of the (anti-)top quark, which is taken from the MC truth record. The datasets are weighted on an event-by-event basis, where the weighting factors, which are derived from Ref. [98] as the ratio of the NNLO to NLO prediction, depend on the (anti-)top quark transverse momentum (cf. Table F.1). Each event is weighted with an overall weighting factor, calculated as the geometric mean of the weighting factors individually obtained for the top quark and the anti-top quark. To actually study the influence of the NNLO reweighting the following approach has been followed. For each mass-value, all  $t\bar{t}$  and single-top MC events are reweighted with the

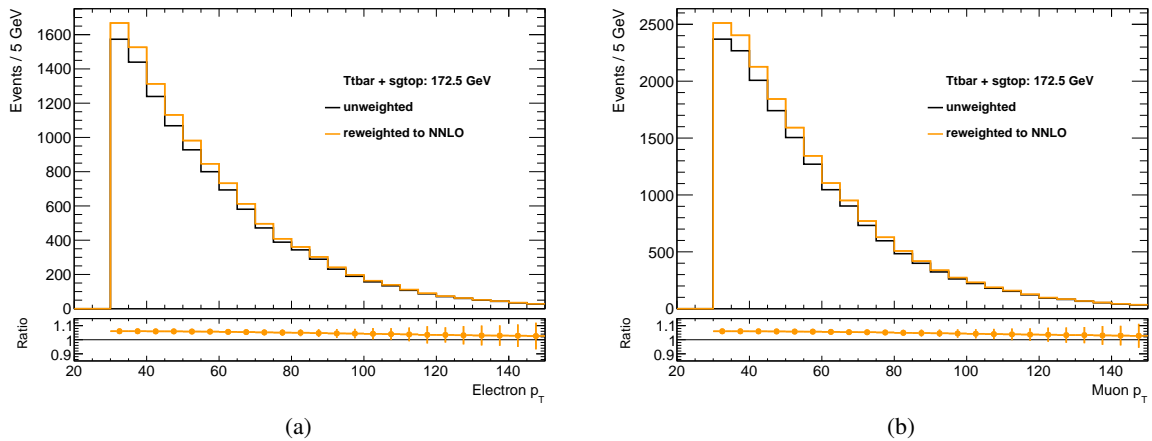


Figure 8.1.: Comparison of the unweighted and weighted lepton  $p_T$  distributions for the  $t\bar{t}$  and single-top processes with a MC top quark mass parameter of 172.5 GeV. Figure (a) shows the electron  $p_T$  distribution and Fig. (b) presents the muon transverse momentum. The unweighted and weighted distributions are coloured black and orange, respectively. For each event, the weighting factor is derived as the geometric mean of the NNLO to NLO ratios obtained for the top quark and (anti-)top quark truth  $p_T$ .

## 8. Modelling of the transverse momentum of the top quark

(anti-)top quark dependent weighting factor and a total of 5000 pseudo experiments are performed with the template derived of the unweighted datasets. An example of the difference of the unweighted and reweighted lepton  $p_T$  distributions is shown in Fig. 8.1. The overall shift is derived, similar to the bias of the measurement discussed in Chapter 6, with a constant fit to the resulting top quark masses, which is shown in Fig. 8.2(a). The actual shift is calculated as the full difference between the result of the constant fit and the bias observed in the measurement (cf. Fig. 6.5(a)) and amounts to  $-0.97^{+0.51}_{-0.47}$  GeV. The uncertainty on this shift is derived, by the quadratic sum of the up/down variation of the (anti-)top quark dependent weighting factors<sup>(1)</sup>, taking into account the uncertainty of the NNLO prediction, and the error on the constant fit itself. As a consistency check, also the reverse approach has been adopted. Here, the template has been created from the weighted datasets, and this template has been applied to the unweighed MC events. Again a total of 5000 pseudo experiments have been performed, with the result shown in Fig. 8.2(b), which yields a shift in the top quark mass of  $1.05^{+0.55}_{-0.50}$  GeV. Due to the nature of this cross check, the shift is opposite to the one obtained previously, but the absolute values are in agreement with each other. Therefore, by not taking into account NNLO order corrections in the MC simulation, the measured top quark mass is underestimated by  $1.0 \pm 0.5$  GeV.

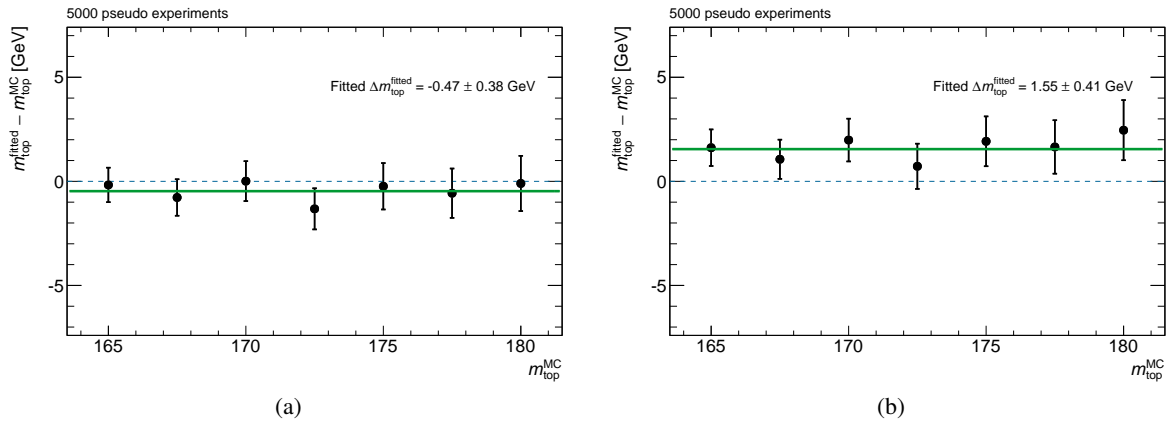


Figure 8.2.: Result of 5000 pseudo experiments for the different MC top quark mass parameters. In Fig. (a) the results of the nominal template, which is used to extract the top quark mass from data, applied to events reweighted to NNLO predictions are shown. In Fig. (b), the template is derived from the reweighted datasets and applied to the unweighted events. Both distributions are fitted with constants, which are shown in green. To estimate the overall influence on the final result in the measured top quark mass due to the reweighting to NNLO predictions, the fit results are compared to the number obtained from Fig. 6.5(a).

<sup>(1)</sup>The results of the pseudo experiments performed for the up and down variation are shown in Appendix F. Furthermore, it turns out that the  $\Delta R_{jj} > 1.1$  requirement, helps in reducing the shift in the measured top quark mass due to NNLO corrections. Without this restriction the shift would amount to  $-1.64^{+0.64}_{-0.52}$  GeV, the corresponding plots are also shown in Appendix F.

## 9. Results

After subtracting the estimated contribution of background processes, the top quark mass is determined by fitting the template as detailed in Chapter 6 to the measured data, which meet the event selection requirements described in Chapter 5. The fit of the template to the electron and muon transverse momentum distributions is shown in Fig. 9.1. The measured top quark mass is

$$m_{\text{top}} = 167.6 \pm 0.9 \text{ (stat) GeV}$$

where the uncertainty quoted represents the statistical precision and the result is already calibrated as described in Chapter 6. The measurement of  $m_{\text{top}}$  has also been performed separately in the electron and muon channels. The fits are shown in Fig. 9.2 and yield values of

$$\begin{aligned} m_{\text{top}}^{\text{electron}} &= 167.5 \pm 1.2 \text{ (stat) GeV} \\ m_{\text{top}}^{\text{muon}} &= 167.7 \pm 1.4 \text{ (stat) GeV} \end{aligned}$$

which are in well agreement with the simultaneous result. Different studies have been performed to cross check the results (cf. Appendix G). No systematic shift in the measured top quark mass has been observed and therefore it is concluded that the rather small value for  $m_{\text{top}}$  is a downwards fluctuation.

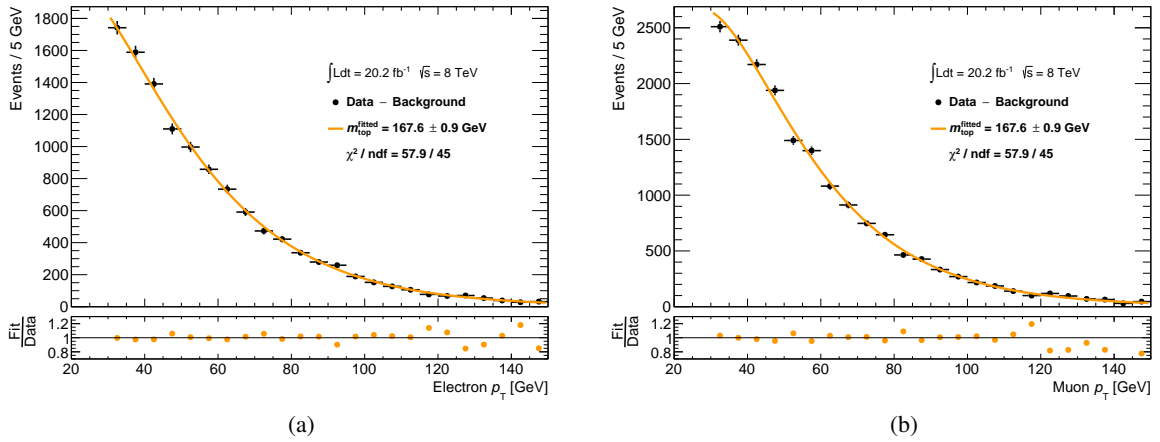


Figure 9.1.: Template fit to the measured lepton transverse momentum distributions. Fig. (a) shows the fitted electron transverse momentum and Fig. (b) presents the fitted muon  $p_T$ . The data points are marked in black and the template fit is coloured orange. The measured top quark mass of  $167.6 \pm 0.9 \text{ (stat) GeV}$  is obtained by taking into account the electron and muon distribution simultaneously, and includes the method calibration. The corresponding  $\chi^2/\text{ndf}$  value of the fit is given in the legend.

## 9. Results

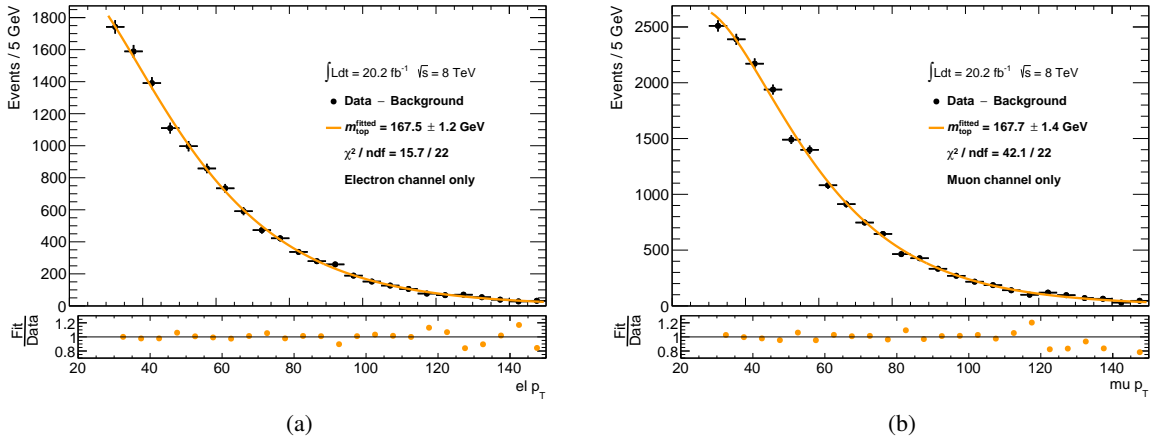


Figure 9.2.: Template fit to the measured lepton transverse momentum distributions. Fig. (a) shows the fitted electron transverse momentum and Fig. (b) presents the fitted muon  $p_T$ . The data points are marked in black and the template fit is coloured orange. The measured top quark masses of  $167.6 \pm 1.2$  (stat) GeV in the electron and  $167.7 \pm 1.4$  (stat) GeV in the muon channel include the method calibration and are obtained separately for the two channels. The corresponding  $\chi^2/\text{ndf}$  values of the fits are given in the legend.

## 10. Conclusion

A total of  $20.2 \text{ fb}^{-1}$  of LHC proton-proton collision data recorded by the ATLAS experiment in 2012 were used to measure the top quark mass in lepton+jets events. By applying tight selection requirements the final event selection consists mainly of  $t\bar{t}$  and single-top events, which both are considered as signal, with minor contributions from  $W$ +jets and fake lepton events. A template method is used to determine  $m_{\text{top}}$ , which exploits the top quark mass dependence of the electron and muon transverse momentum distributions. The measurement technique is verified by pseudo experiments, and the result is calibrated accordingly. The overall precision of  $m_{\text{top}}$  is estimated to be 2.4 GeV and is evaluated by studying different sources of uncertainties. The final result of the measurement of the top quark mass using lepton transverse momenta is

$$m_{\text{top}} = 167.6 \pm 0.9 \text{ (stat)} \pm 2.2 \text{ (syst) GeV}$$

Due to the sensitivity of the lepton  $p_{\text{T}}$  distributions on the top quark transverse momentum, the influence of higher order corrections on this result has been investigated, which indicates that the determined top quark mass may be underestimated by  $1.0 \pm 0.5 \text{ GeV}$ . In a future analysis, this dependence could be exploited to infer the top quark transverse momentum from the measured lepton  $p_{\text{T}}$  distributions. By taking into account the overall uncertainty and the higher order dependence of the result, the measured value of  $m_{\text{top}}$  is compatible with other top quark mass measurements (cf. Ref. [8, 10–14]).



# A List of data and MC datasets

This section lists the datasets which are used in the analysis. The naming of the datasets follows the ATLAS convention. The first part specifies, if a dataset contains data or MC events, denotes the corresponding data taking period and the centre-of-mass energy. In case of data, the run period and the physics stream are stated. For simulation, the dataset ID together with the generator set-up and the simulated process are given. In addition, details of the ATLAS software settings, used for the simulation data, are specified. The last part of the dataset name refers to the settings used in the reconstruction. Simulated datasets marked with <sup>(†)</sup> are processed with a simplified shower parametrisation, while the datasets used to evaluate the PDF uncertainties are indicated with <sup>(\*)</sup>.

## Data

Only data events listed in the good runs list named data12.8TeV.periodAllYear\_DetStatus-v61-pro14-02\_DQDefects-00-01-00\_PHYS\_StandardGRL\_All\_Good.xml are used in this analysis.

data12.8TeV.periodA.physics\_Egamma.PhysCont.NTUP.COMMON.grp14.v01.p1517.p1562  
data12.8TeV.periodB.physics\_Egamma.PhysCont.NTUP.COMMON.grp14.v01.p1278.p1562  
data12.8TeV.periodC.physics\_Egamma.PhysCont.NTUP.COMMON.grp14.v01.p1278.p1562  
data12.8TeV.periodD.physics\_Egamma.PhysCont.NTUP.COMMON.grp14.v01.p1278.p1562  
data12.8TeV.periodE.physics\_Egamma.PhysCont.NTUP.COMMON.grp14.v01.p1278.p1562  
data12.8TeV.periodG.physics\_Egamma.PhysCont.NTUP.COMMON.grp14.v01.p1278.p1562  
data12.8TeV.periodH.physics\_Egamma.PhysCont.NTUP.COMMON.grp14.v01.p1278.p1562  
data12.8TeV.periodI.physics\_Egamma.PhysCont.NTUP.COMMON.grp14.v01.p1562  
data12.8TeV.periodJ.physics\_Egamma.PhysCont.NTUP.COMMON.grp14.v01.p1562  
data12.8TeV.periodL.physics\_Egamma.PhysCont.NTUP.COMMON.grp14.v01.p1562  
data12.8TeV.periodA.physics\_Muons.PhysCont.NTUP.COMMON.grp14.v01.p1517.p1562  
data12.8TeV.periodB.physics\_Muons.PhysCont.NTUP.COMMON.grp14.v01.p1278.p1562  
data12.8TeV.periodC.physics\_Muons.PhysCont.NTUP.COMMON.grp14.v01.p1278.p1562  
data12.8TeV.periodD.physics\_Muons.PhysCont.NTUP.COMMON.grp14.v01.p1278.p1562  
data12.8TeV.periodE.physics\_Muons.PhysCont.NTUP.COMMON.grp14.v01.p1278.p1562  
data12.8TeV.periodG.physics\_Muons.PhysCont.NTUP.COMMON.grp14.v01.p1278.p1562  
data12.8TeV.periodH.physics\_Muons.PhysCont.NTUP.COMMON.grp14.v01.p1278.p1562  
data12.8TeV.periodI.physics\_Muons.PhysCont.NTUP.COMMON.grp14.v01.p1562  
data12.8TeV.periodJ.physics\_Muons.PhysCont.NTUP.COMMON.grp14.v01.p1562  
data12.8TeV.periodL.physics\_Muons.PhysCont.NTUP.COMMON.grp14.v01.p1562

## MC datasets

### Nominal datasets

mc12.8TeV.110090.PowhegPythia\_P2011C\_singletop\_tchan\_lept\_top.merge.NTUP.COMMON.e2575\_s1773\_s1776\_r4485\_r4540.p1575  
mc12.8TeV.110091.PowhegPythia\_P2011C\_singletop\_tchan\_lept\_antitop.merge.NTUP.COMMON.e2575\_s1773\_s1776\_r4485\_r4540.p1575  
mc12.8TeV.110119.PowhegPythia\_P2011C\_st\_schan\_lep.merge.NTUP.COMMON.e1720\_s1581\_s1586\_r3658\_r3549.p1575  
mc12.8TeV.110140.PowhegPythia\_P2011C\_st\_Wtchan\_incl\_DR.merge.NTUP.COMMON.e1743\_s1581\_s1586\_r3925\_r3549.p1575  
mc12.8TeV.200256.AlpGenPythia\_Auto\_P2011C\_WbbNp0.merge.NTUP.COMMON.e2384\_s1581\_s1586\_r3658\_r3549.p1575  
mc12.8TeV.200257.AlpGenPythia\_Auto\_P2011C\_WbbNp1.merge.NTUP.COMMON.e2384\_s1581\_s1586\_r3658\_r3549.p1575  
mc12.8TeV.200258.AlpGenPythia\_Auto\_P2011C\_WbbNp2.merge.NTUP.COMMON.e2384\_s1581\_s1586\_r3658\_r3549.p1575  
mc12.8TeV.200259.AlpGenPythia\_Auto\_P2011C\_WbbNp3incl.merge.NTUP.COMMON.e2384\_s1581\_s1586\_r3658\_r3549.p1575  
mc12.8TeV.200156.AlpGenPythia\_Auto\_P2011C\_WccNp0.merge.NTUP.COMMON.e2384\_s1581\_s1586\_r3658\_r3549.p1575  
mc12.8TeV.200157.AlpGenPythia\_Auto\_P2011C\_WccNp1.merge.NTUP.COMMON.e2384\_s1581\_s1586\_r3658\_r3549.p1575  
mc12.8TeV.200158.AlpGenPythia\_Auto\_P2011C\_WccNp2.merge.NTUP.COMMON.e2384\_s1581\_s1586\_r3658\_r3549.p1575  
mc12.8TeV.200159.AlpGenPythia\_Auto\_P2011C\_WccNp3incl.merge.NTUP.COMMON.e2384\_s1581\_s1586\_r3658\_r3549.p1575  
mc12.8TeV.200056.AlpGenPythia\_Auto\_P2011C\_WcNp0.merge.NTUP.COMMON.e2384\_s1581\_s1586\_r3658\_r3549.p1575  
mc12.8TeV.200057.AlpGenPythia\_Auto\_P2011C\_WcNp1.merge.NTUP.COMMON.e2384\_s1581\_s1586\_r3658\_r3549.p1575  
mc12.8TeV.200058.AlpGenPythia\_Auto\_P2011C\_WcNp2.merge.NTUP.COMMON.e2384\_s1581\_s1586\_r3658\_r3549.p1575



---

## Mass variation datasets

mc12.8TeV.117836.TTbar\_MT1650\_nonallhad.PowHeg\_Pythia\_P2011C.merge.NTUP\_COMMON.e2051\_s1581\_s1586\_r3658\_r3549\_p1562  
mc12.8TeV.117838.TTbar\_MT1675\_nonallhad.PowHeg\_Pythia\_P2011C.merge.NTUP\_COMMON.e2051\_s1581\_s1586\_r3658\_r3549\_p1562  
mc12.8TeV.117840.TTbar\_MT1700\_nonallhad.PowHeg\_Pythia\_P2011C.merge.NTUP\_COMMON.e2051\_s1581\_s1586\_r3658\_r3549\_p1562  
mc12.8TeV.117842.TTbar\_MT1750\_nonallhad.PowHeg\_Pythia\_P2011C.merge.NTUP\_COMMON.e2051\_s1581\_s1586\_r3658\_r3549\_p1562  
mc12.8TeV.117844.TTbar\_MT1775\_nonallhad.PowHeg\_Pythia\_P2011C.merge.NTUP\_COMMON.e2051\_s1581\_s1586\_r3658\_r3549\_p1562  
mc12.8TeV.117846.TTbar\_MT1800\_nonallhad.PowHeg\_Pythia\_P2011C.merge.NTUP\_COMMON.e2051\_s1581\_s1586\_r3658\_r3549\_p1562  
mc12.8TeV.110113.AcerMCPythia\_P2011CCTEQ6L1\_singletop\_tchan.L.mt165.merge.NTUP\_COMMON.e1915\_a188\_a171\_r3549\_p1562 (†)  
mc12.8TeV.110114.AcerMCPythia\_P2011CCTEQ6L1\_singletop\_tchan.L.mt167p5.merge.NTUP\_COMMON.e1915\_a188\_a171\_r3549\_p1562 (†)  
mc12.8TeV.110115.AcerMCPythia\_P2011CCTEQ6L1\_singletop\_tchan.L.mt170.merge.NTUP\_COMMON.e1915\_a188\_a171\_r3549\_p1562 (†)  
mc12.8TeV.110116.AcerMCPythia\_P2011CCTEQ6L1\_singletop\_tchan.L.mt175.merge.NTUP\_COMMON.e1915\_a188\_a171\_r3549\_p1562 (†)  
mc12.8TeV.110117.AcerMCPythia\_P2011CCTEQ6L1\_singletop\_tchan.L.mt177p5.merge.NTUP\_COMMON.e1915\_a188\_a171\_r3549\_p1562 (†)  
mc12.8TeV.110118.AcerMCPythia\_P2011CCTEQ6L1\_singletop\_tchan.L.mt180.merge.NTUP\_COMMON.e1915\_a188\_a171\_r3549\_p1562 (†)  
mc12.8TeV.110123.PowhegPythia\_P2011CCTEQ6L1\_singletop\_sch\_wlep\_mt165.merge.NTUP\_COMMON.e2075\_a188\_a171\_r3549\_p1575 (†)  
mc12.8TeV.110125.PowhegPythia\_P2011CCTEQ6L1\_singletop\_sch\_wlep\_mt167p5.merge.NTUP\_COMMON.e2075\_a188\_a171\_r3549\_p1575 (†)  
mc12.8TeV.110127.PowhegPythia\_P2011CCTEQ6L1\_singletop\_sch\_wlep\_mt170.merge.NTUP\_COMMON.e2075\_a188\_a171\_r3549\_p1575 (†)  
mc12.8TeV.110129.PowhegPythia\_P2011CCTEQ6L1\_singletop\_sch\_wlep\_mt175.merge.NTUP\_COMMON.e2075\_a188\_a171\_r3549\_p1575 (†)  
mc12.8TeV.110131.PowhegPythia\_P2011CCTEQ6L1\_singletop\_sch\_wlep\_mt177p5.merge.NTUP\_COMMON.e2075\_a188\_a171\_r3549\_p1575 (†)  
mc12.8TeV.110133.PowhegPythia\_P2011CCTEQ6L1\_singletop\_sch\_wlep\_mt180.merge.NTUP\_COMMON.e2075\_a188\_a171\_r3549\_p1575 (†)  
mc12.8TeV.110124.PowhegPythia\_P2011CCTEQ6L1\_singletop\_Wtch\_DR\_incl.mt165.merge.NTUP\_COMMON.e2075\_a188\_a171\_r3549\_p1562 (†)  
mc12.8TeV.110126.PowhegPythia\_P2011CCTEQ6L1\_singletop\_Wtch\_DR\_incl.mt167p5.merge.NTUP\_COMMON.e2075\_a188\_a171\_r3549\_p1562 (†)  
mc12.8TeV.110128.PowhegPythia\_P2011CCTEQ6L1\_singletop\_Wtch\_DR\_incl.mt170.merge.NTUP\_COMMON.e2075\_a188\_a171\_r3549\_p1562 (†)  
mc12.8TeV.110130.PowhegPythia\_P2011CCTEQ6L1\_singletop\_Wtch\_DR\_incl.mt175.merge.NTUP\_COMMON.e2075\_a188\_a171\_r3549\_p1562 (†)  
mc12.8TeV.110132.PowhegPythia\_P2011CCTEQ6L1\_singletop\_Wtch\_DR\_incl.mt177p5.merge.NTUP\_COMMON.e2075\_a188\_a171\_r3549\_p1562 (†)  
mc12.8TeV.110134.PowhegPythia\_P2011CCTEQ6L1\_singletop\_Wtch\_DR\_incl.mt180.merge.NTUP\_COMMON.e2075\_a188\_a171\_r3549\_p1562 (†)

## Systematic datasets

mc12.8TeV.117050.PowhegPythia\_P2011C\_ttbar.merge.NTUP\_COMMON.e1727\_a188\_a171\_r3549\_p1575 (†)  
mc12.8TeV.117428.PowhegPythia\_P2012\_TTbar.merge.NTUP\_COMMON.e2710\_a220\_a205\_r4540\_p1575 (†)  
mc12.8TeV.105200.McAtNloJimmy\_CT10\_ttbar\_LeptonFilter.merge.NTUP\_COMMON.e1513\_a159\_a171\_r3549\_p1575 (†)  
mc12.8TeV.105860.PowhegJimmy\_AUET2CT10\_ttbar\_LeptonFilter.merge.NTUP\_COMMON.e1576\_a159\_a171\_r3549\_p1575 (†)  
mc12.8TeV.110407.PowhegPythia\_Perugia2012radLo\_ttbar\_hdamp172p5\_nonallhad.merge.NTUP\_COMMON.e3876\_a220\_a263\_a264\_r4540\_p1770 (†)  
mc12.8TeV.110408.PowhegPythia\_Perugia2012radHi\_ttbar\_hdamp345p0\_nonallhad.merge.NTUP\_COMMON.e3876\_a220\_a263\_a264\_r4540\_p1770 (†)  
mc12.8TeV.117426.PowhegPythia\_P2012loCR\_TTbar.merge.NTUP\_COMMON.e2710\_a220\_a205\_r4540\_p1575 (†)  
mc12.8TeV.117429.PowhegPythia\_P2012mpiHi\_TTbar.merge.NTUP\_COMMON.e2710\_a220\_a205\_r4540\_p1575 (†)  
mc12.8TeV.110142.PowhegPythia\_P2011C\_st\_Wtchan\_incl\_DS.merge.NTUP\_COMMON.e1743\_s1581\_s1586\_r3925\_r3549\_p1575  
mc12.8TeV.105200.McAtNloJimmy\_CT10\_ttbar\_LeptonFilter.merge.NTUP\_COMMON.e1513\_s1499\_s1504\_r3658\_r3549\_p1562 (\*)  
mc12.8TeV.110101.AcerMCPythia\_P2011CCTEQ6L1\_singletop\_tchan.L.merge.NTUP\_COMMON.e1731\_s1581\_s1586\_r3658\_r3549\_p1575 (\*)  
mc12.8TeV.108343.McAtNloJimmy\_AUET2CT10\_SingleTopSChanWenu.merge.NTUP\_COMMON.e1525\_s1499\_s1504\_r3658\_r3549\_p1575 (\*)  
mc12.8TeV.108344.McAtNloJimmy\_AUET2CT10\_SingleTopSChanWmunu.merge.NTUP\_COMMON.e1525\_s1499\_s1504\_r3658\_r3549\_p1575 (\*)  
mc12.8TeV.108345.McAtNloJimmy\_AUET2CT10\_SingleTopSChanWtaunu.merge.NTUP\_COMMON.e1525\_s1499\_s1504\_r3658\_r3549\_p1575 (\*)  
mc12.8TeV.108346.McAtNloJimmy\_AUET2CT10\_SingleTopWtChanIncl.merge.NTUP\_COMMON.e1525\_s1499\_s1504\_r3658\_r3549\_p1575 (\*)



## B Data and MC distributions for $m_{\text{top}} = 167.5 \text{ GeV}$

Here, the same distributions as in Section 5.3 are shown, but with a MC top quark mass parameter of 167.5 GeV instead of 172.5 GeV.

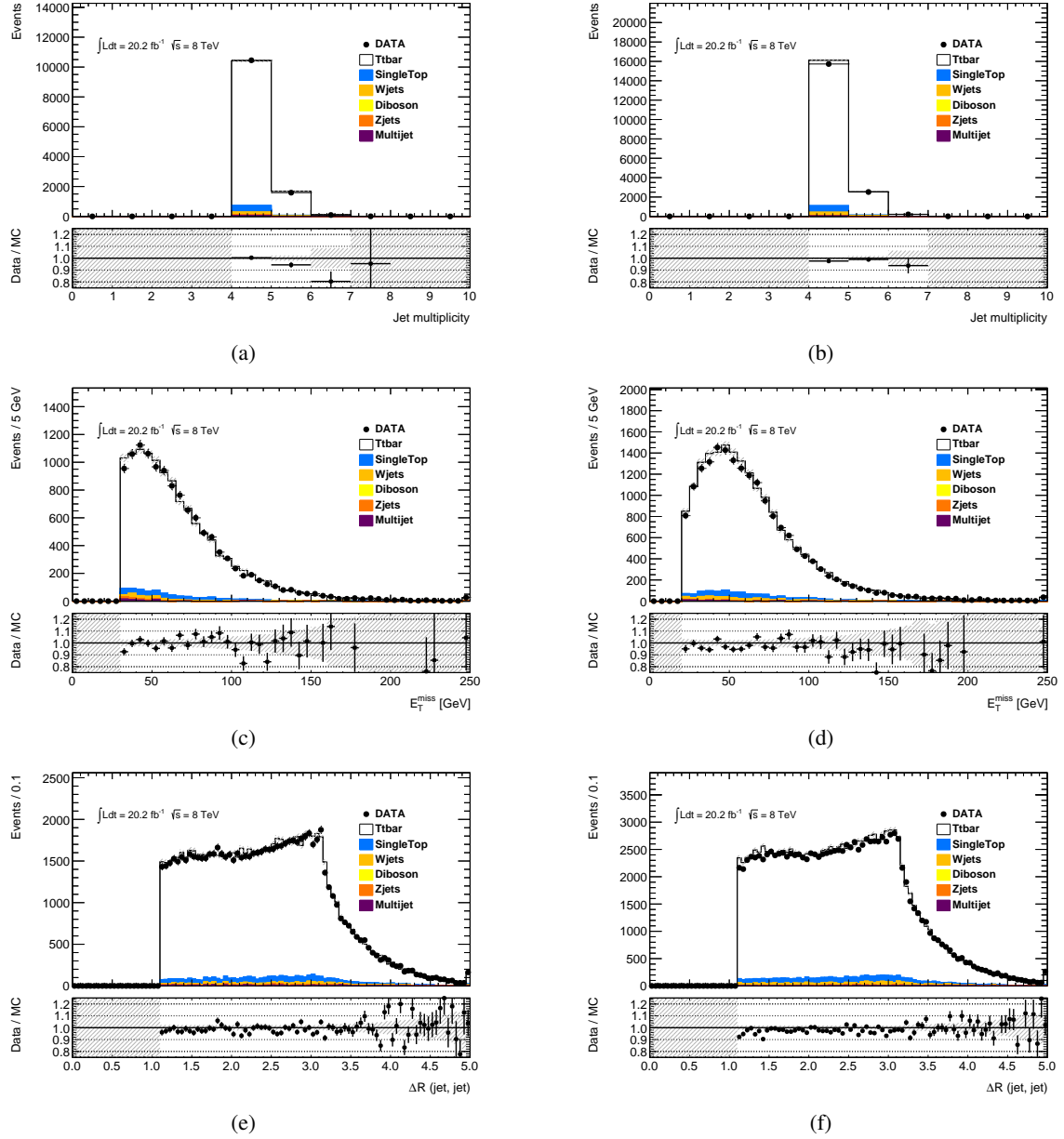


Figure B.1.: Distributions for the selected events, in the electron channel on the left and in the muon channel on the right hand side, are presented. Figure (a) and (b) show the jet multiplicities, while Fig. (c) and Fig. (d) illustrate the  $E_T^{\text{miss}}$  distributions. The  $\Delta R_{ij}$  distributions are presented in Fig.(e) and Fig.(f). The data are plotted as black points with their respective statistical error. In addition, the expected contributions of the relevant physics processes, colour coded according to the legend, are indicated. For the  $t\bar{t}$  and single-top signal processes a top quark mass of 167.5 GeV is assumed.

B. Data and MC distributions for  $m_{top} = 167.5 \text{ GeV}$

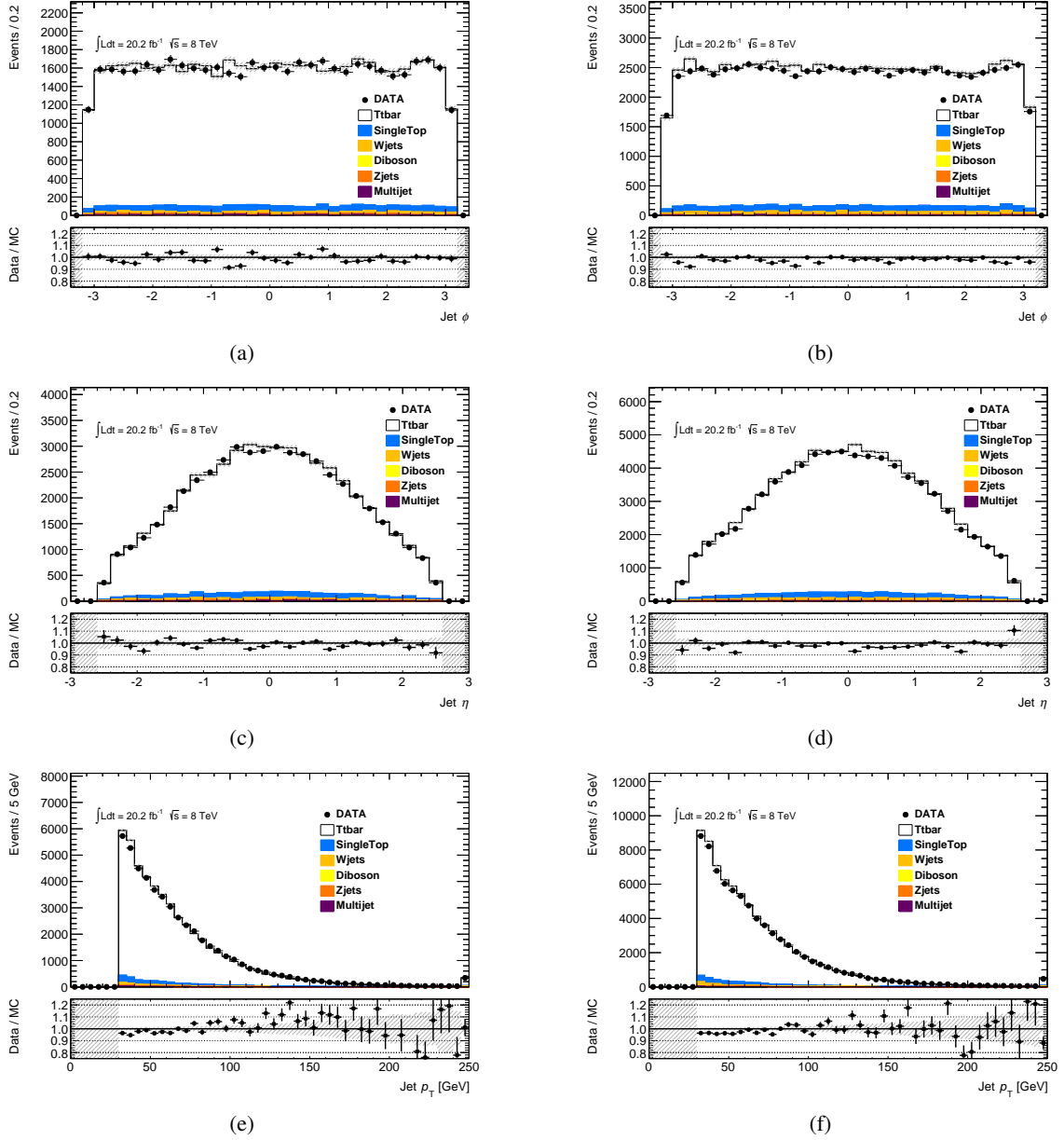


Figure B.2.: Distributions for the selected events, in the electron channel on the left and in the muon channel on the right hand side, are presented. Figures (a) and (b) show the  $\phi$  distributions of the jets, while Fig. (c) and Fig. (d) illustrate their  $\eta$  distributions. The jet transverse momenta are presented in Fig. (e) and Fig. (f). The data are plotted as black points with their respective statistical error. In addition, the expected contributions of the relevant physics processes, colour coded according to the legend, are indicated. For the  $t\bar{t}$  and single-top signal processes a top quark mass of  $167.5 \text{ GeV}$  is assumed.

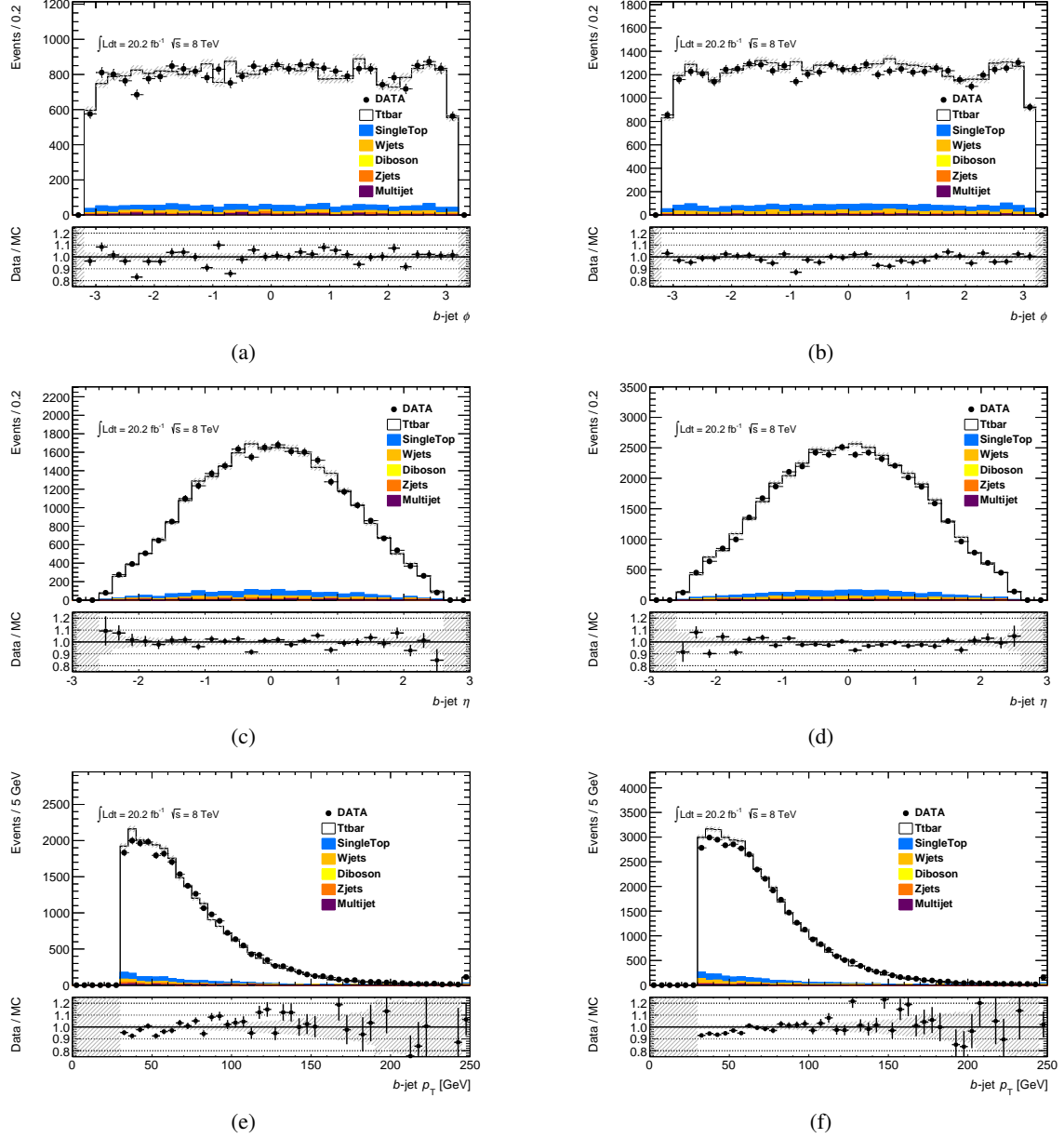


Figure B.3.: Distributions for the selected events, in the electron channel on the left and in the muon channel on the right hand side, are presented. Figures (a) and (b) show the  $\phi$  distributions of the  $b$ -tagged jets, while Fig. (c) and Fig. (d) illustrate their  $\eta$  distributions. The transverse momenta of  $b$ -tagged jets are presented in Fig. (e) and Fig. (f). The data are plotted as black points with their respective statistical error. In addition, the expected contributions of the relevant physics processes, colour coded according to the legend, are indicated. For the  $t\bar{t}$  and single-top signal processes a top quark mass of 167.5 GeV is assumed.

B. Data and MC distributions for  $m_{top} = 167.5 \text{ GeV}$

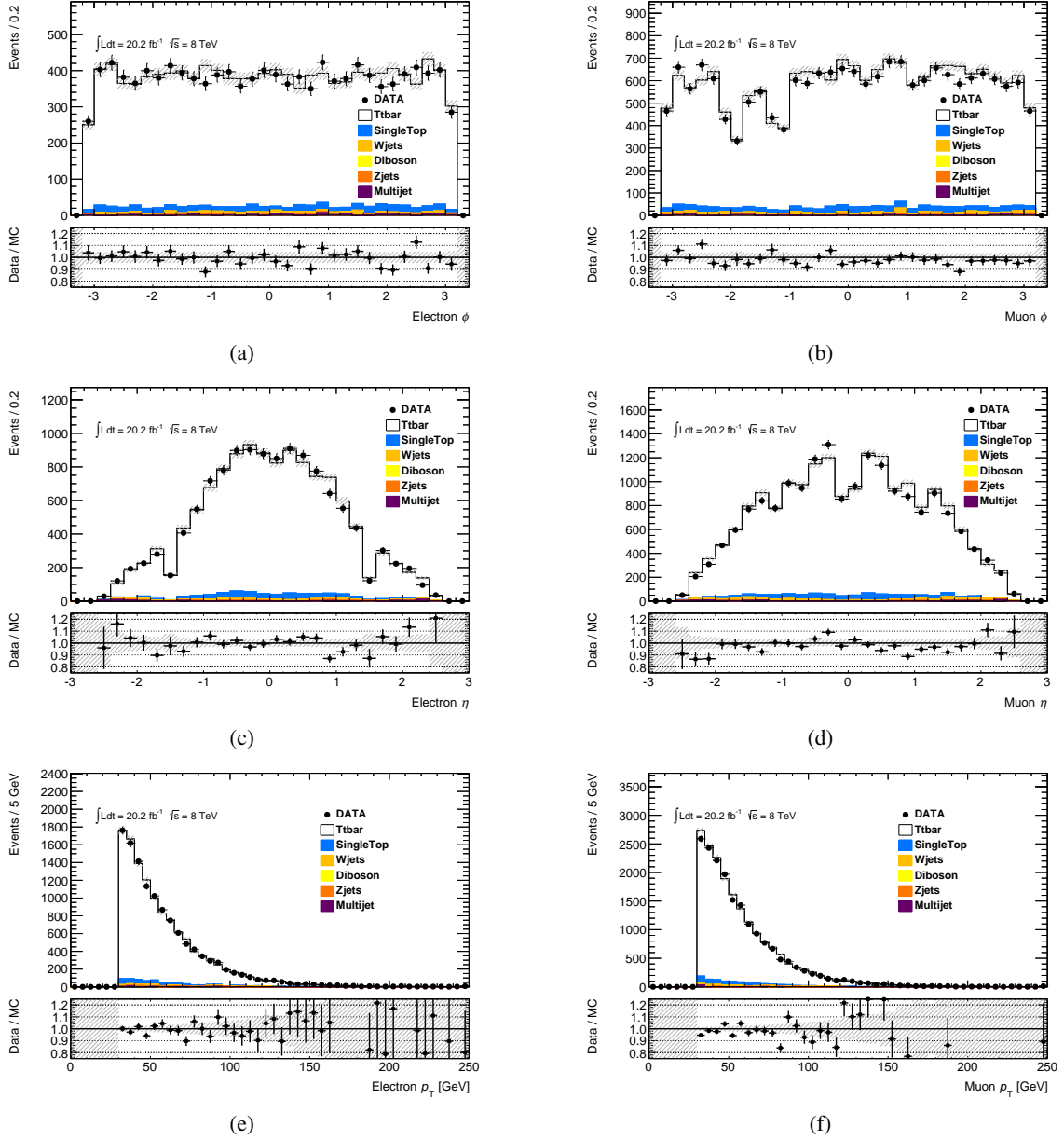


Figure B.4.: Distributions for the selected events, in the electron channel on the left and in the muon channel on the right hand side, are presented. Figures (a) and (b) show the  $\phi$  distributions of the leptons, while Fig. (c) and Fig. (d) illustrate their  $\eta$  distributions. The lepton transverse momenta are presented in Fig. (e) and Fig. (f). The data are plotted as black points with their respective statistical error. In addition, the expected contributions of the relevant physics processes, colour coded according to the legend, are indicated. For the  $t\bar{t}$  and single-top signal processes a top quark mass of  $167.5 \text{ GeV}$  is assumed.

## C Additional information concerning the template fit

In this chapter some additional information concerning the template used to extract the top quark mass are given. The parameters used in the template are stated in Table C.1, while Fig. C.1 and C.2 show the fitted electron and muon  $p_T$  distributions for different mass point samples. Similar plots for the approach in which the electron and muon channels are treated separately are shown in Figs. C.3 - C.6, with the corresponding parameters for the template given in Table C.2. The results of 5000 pseudo experiments which have been drawn from the template itself instead of the MC sample are shown in Fig C.7.

Novosibirsk parameters	Electron channel		Muon channel	
	Intercept	Slope	Intercept	Slope
Normalisation	0.150 (fixed)	0.000 (fixed)	0.120 (fixed)	0.000 (fixed)
Mean	$86.186 \pm 0.478$	$-0.416 \pm 0.003$	$59.323 \pm 0.395$	$-0.191 \pm 0.002$
Width	$-34.472 \pm 0.223$	$0.347 \pm 0.001$	$-17.790 \pm 0.178$	$0.227 \pm 0.001$
Asymmetry	$1.059 \pm 0.007$	$-0.004 \pm 0.000$	$1.065 \pm 0.006$	$-0.004 \pm 0.000$

Table C.1.: Template parameters used in the analysis. Parameters are derived from a simultaneous combined fit to the mass-value samples. In the template, each Novosibirsk parameter is linearly dependent on the top quark mass, with  $\text{par} = \text{intercept} + \text{slope} \cdot m_{\text{top}}$ .

Novosibirsk parameters	Electron channel		Muon channel	
	Intercept	Slope	Intercept	Slope
Normalisation	0.150 (fixed)	0.000 (fixed)	0.120 (fixed)	0.000 (fixed)
Mean	$86.491 \pm 4.714$	$-0.418 \pm 0.027$	$59.494 \pm 4.177$	$-0.192 \pm 0.024$
Width	$-35.602 \pm 3.279$	$0.354 \pm 0.019$	$-18.883 \pm 3.484$	$0.233 \pm 0.020$
Asymmetry	$1.089 \pm 0.086$	$-0.004 \pm 0.000$	$1.099 \pm 0.125$	$-0.004 \pm 0.001$

Table C.2.: Template parameters used in the analysis. Parameters are derived separately for the electron and muon channel, from a fit to the mass-value samples. In the template, each Novosibirsk parameter is linearly dependent on the top quark mass, with  $\text{par} = \text{intercept} + \text{slope} \cdot m_{\text{top}}$ .

### C. Additional information concerning the template fit

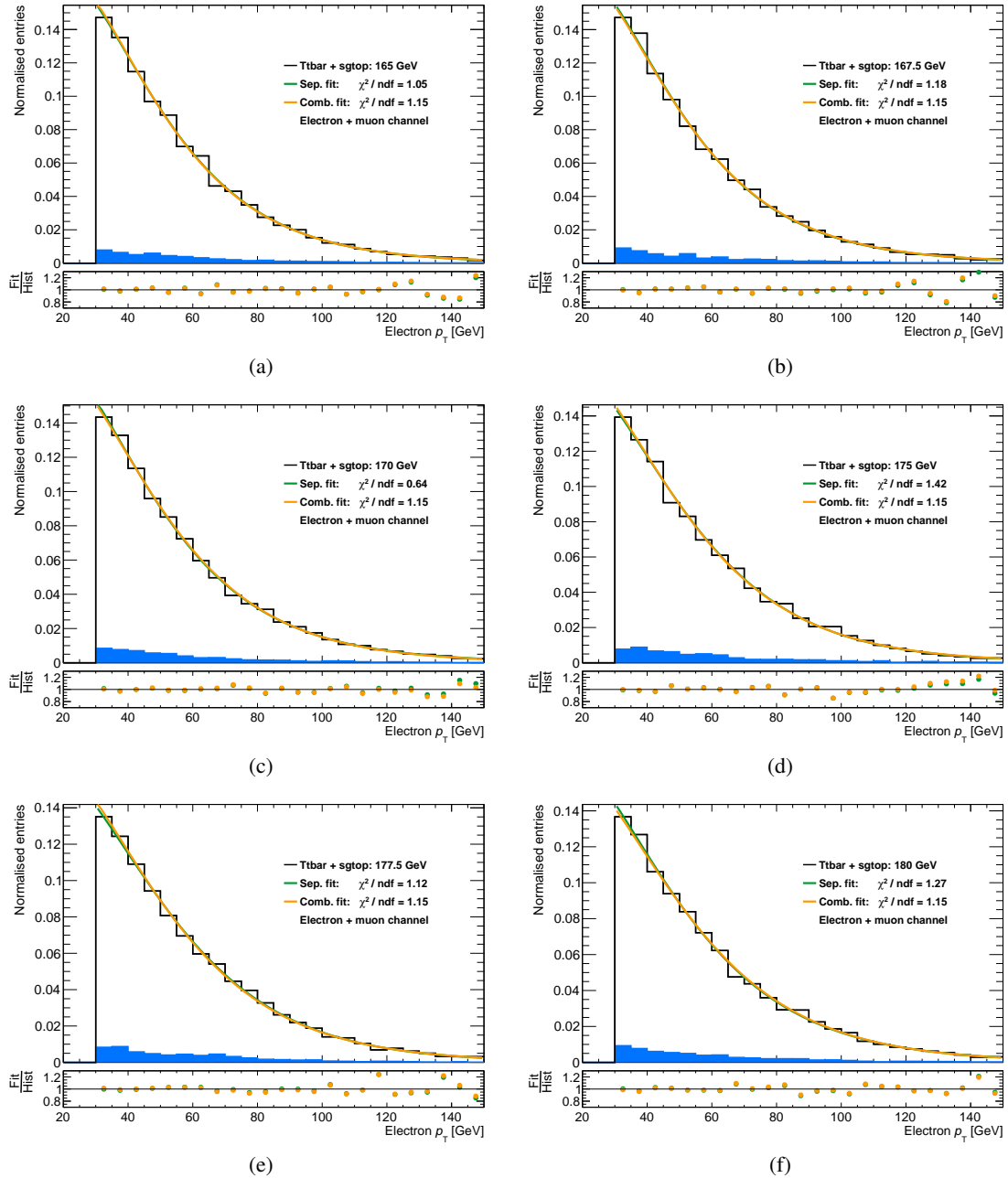


Figure C.1.: Fits to the electron  $p_T$  distributions for different mass-value samples with top quark mass parameters ranging from 165 to 180 GeV. In the analysis the  $t\bar{t}$  as well as the single-top process are considered signal and therefore both are used for the template derivation. The single-top fraction is plotted in blue and the  $t\bar{t}$  contribution is shown in white. The fit with the Novosibirsk function is indicated in green, while the combined fit, which is done by taking into account the electron and muon channels simultaneously, is shown in orange. The corresponding  $\chi^2/\text{ndf}$  value of the fits are given in the legend. The plots have been normalised to unity.

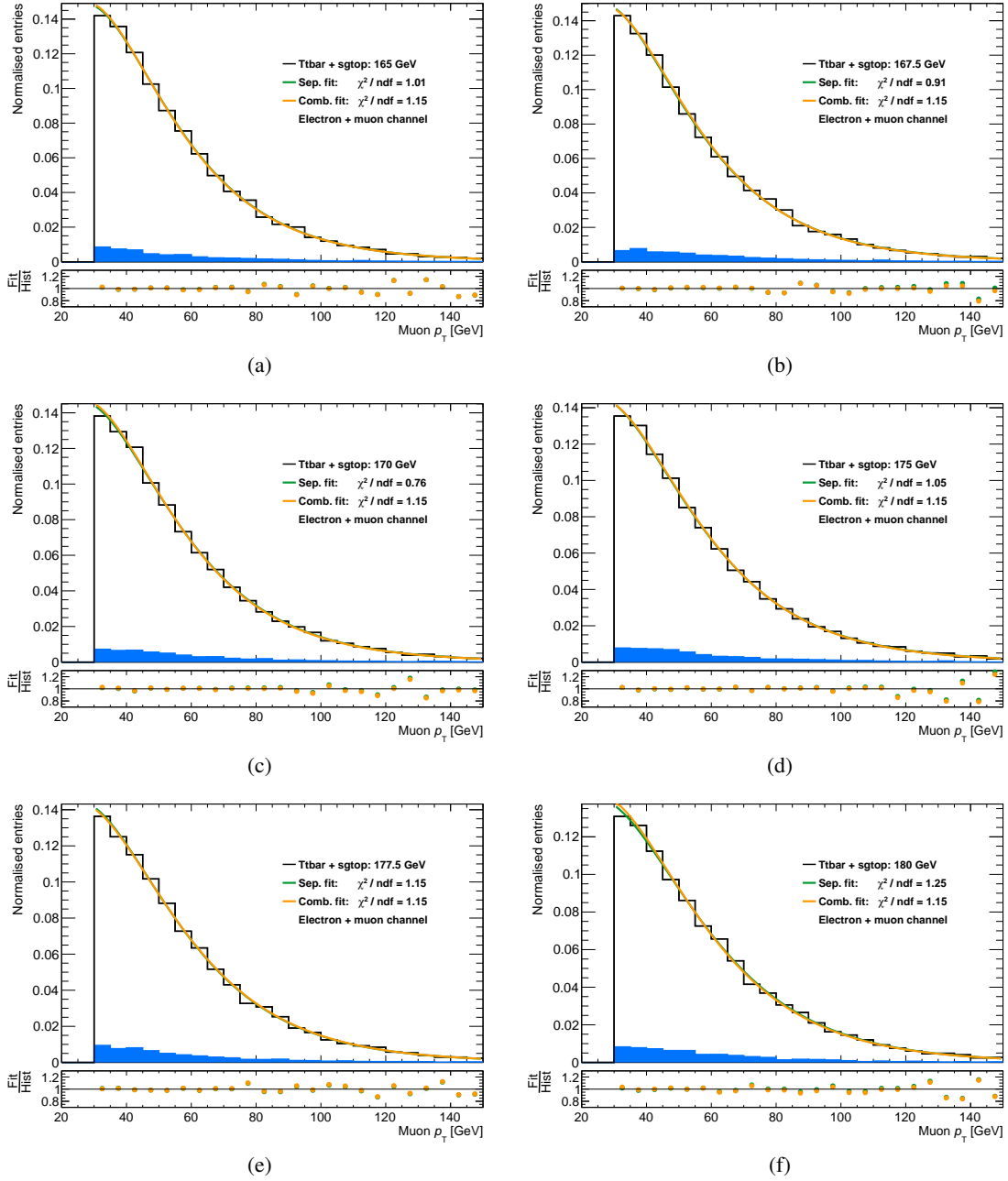


Figure C.2.: Fits to the muon  $p_T$  distributions for different mass-value samples with top quark mass parameters ranging from 165 to 180 GeV. In the analysis the  $t\bar{t}$  as well as the single-top process are considered signal and therefore both are used for the template derivation. The single-top fraction is plotted in blue and the  $t\bar{t}$  contribution is shown in white. The fit with the Novosibirsk function is indicated in green, while the combined fit, which is done by taking into account the electron and muon channels simultaneously, is shown in orange. The corresponding  $\chi^2/\text{ndf}$  value of the fits are given in the legend. The plots have been normalised to unity.

### C. Additional information concerning the template fit

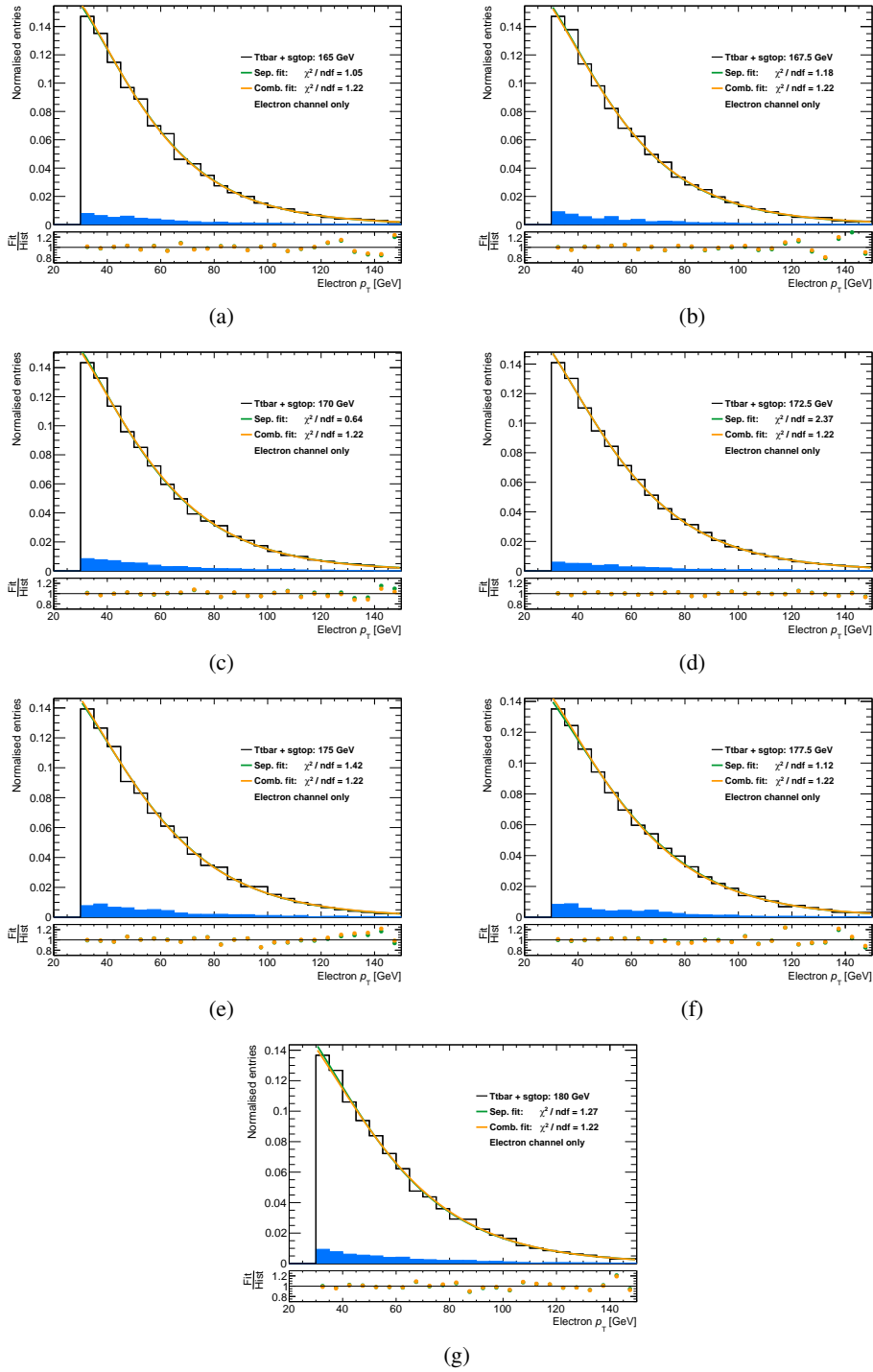


Figure C.3.: Fits to the electron  $p_T$  distributions for different mass-value samples with top quark mass parameters ranging from 165 to 180 GeV. In the analysis the  $t\bar{t}$  as well as the single-top process are considered signal and therefore both are used for the template derivation. The single-top fraction is plotted in blue and the  $t\bar{t}$  contribution is shown in white. The fit with the Novosibirsk function is indicated in green, while the combined fit, which only takes into account the electron channel, is shown in orange. The corresponding  $\chi^2/\text{ndf}$  value of the fits are given in the legend. The plots have been normalised to unity.

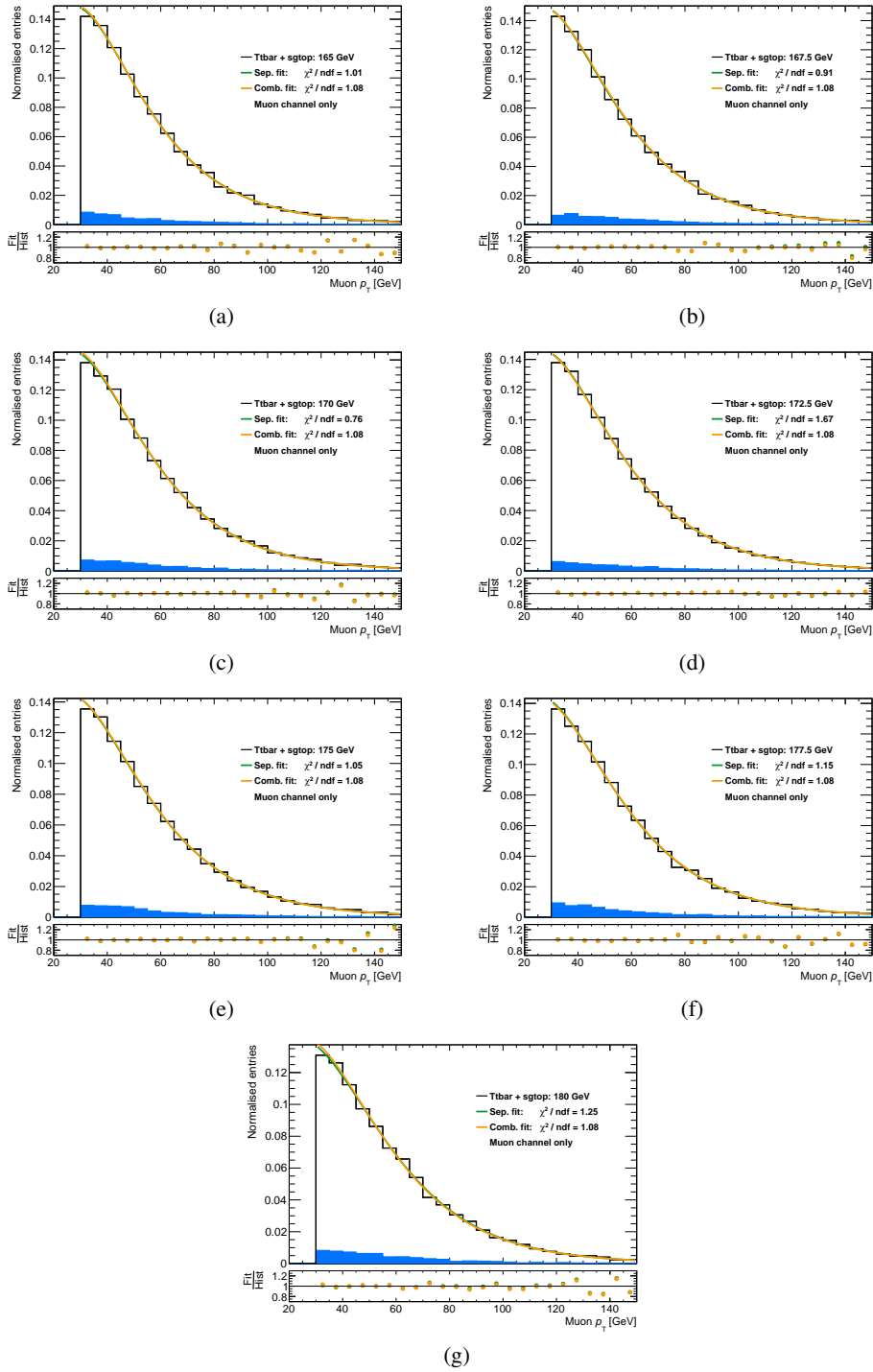


Figure C.4.: Fits to the muon  $p_T$  distributions for different mass-value samples with top quark mass parameters ranging from 165 to 180 GeV. In the analysis the  $t\bar{t}$  as well as the single-top process are considered signal and therefore both are used for the template derivation. The single-top fraction is plotted in blue and the  $t\bar{t}$  contribution is shown in white. The fit with the Novosibirsk function is indicated in green, while the combined fit, which only takes into account the muon channel, is shown in orange. The corresponding  $\chi^2/\text{ndf}$  value of the fits are given in the legend. The plots have been normalised to unity.

### C. Additional information concerning the template fit

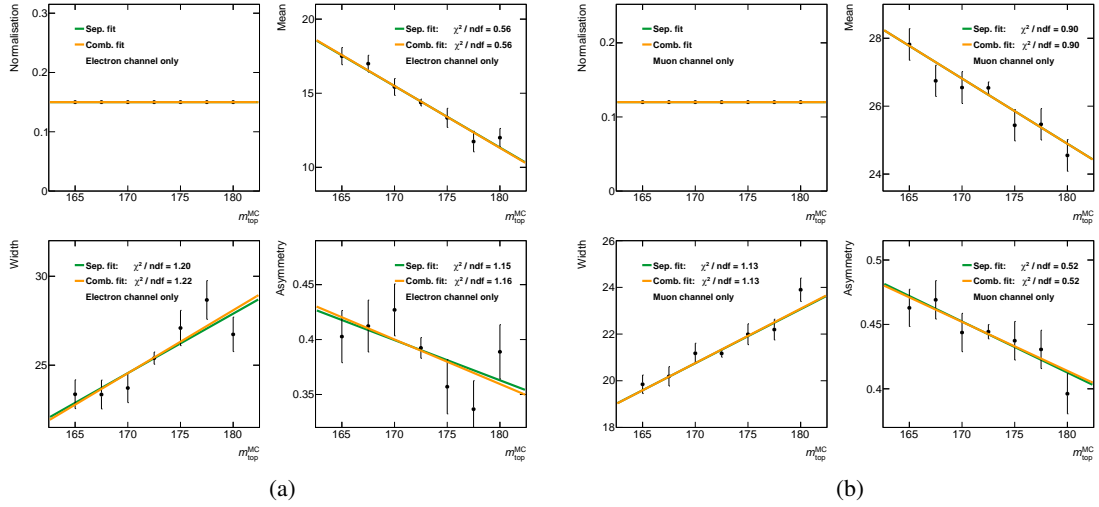


Figure C.5.: The four parameters of the Novosibirsk function as function of the top quark mass. Fig. (a) shows the parameter dependencies in the electron and Fig. (b) in the muon channel. The parameters are obtained by fitting a Novosibirsk function separately to the electron and muon  $p_T$  distributions of the mass-value MC with top quark mass parameters ranging from 165 to 180 GeV. In both channels the overall normalisation parameter has been fixed. The first order polynomial fits to the parameter distributions are shown in green, while the combined fit, which is done by taking into account the electron and muon channels separately, is shown in orange.

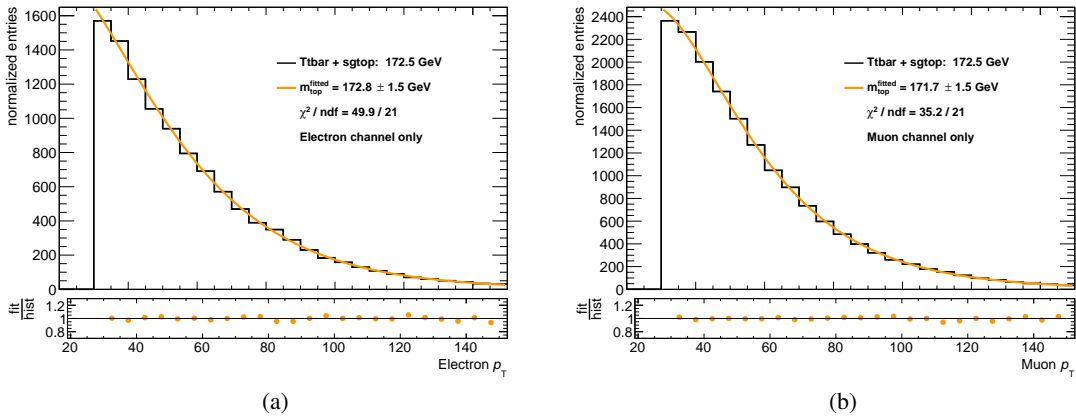


Figure C.6.: Template fit to the 172.5 GeV signal MC distributions, by taking into account the electron and muon channels separately. The histograms show the combination of the signal  $t\bar{t}$  and single-top processes. The template fit in the electron channel is presented in Fig. (a) and the fit for the muon channel is shown in Fig. (b). The fit result with the corresponding statistical error and the  $\chi^2/\text{ndf}$  value are given in the legend.

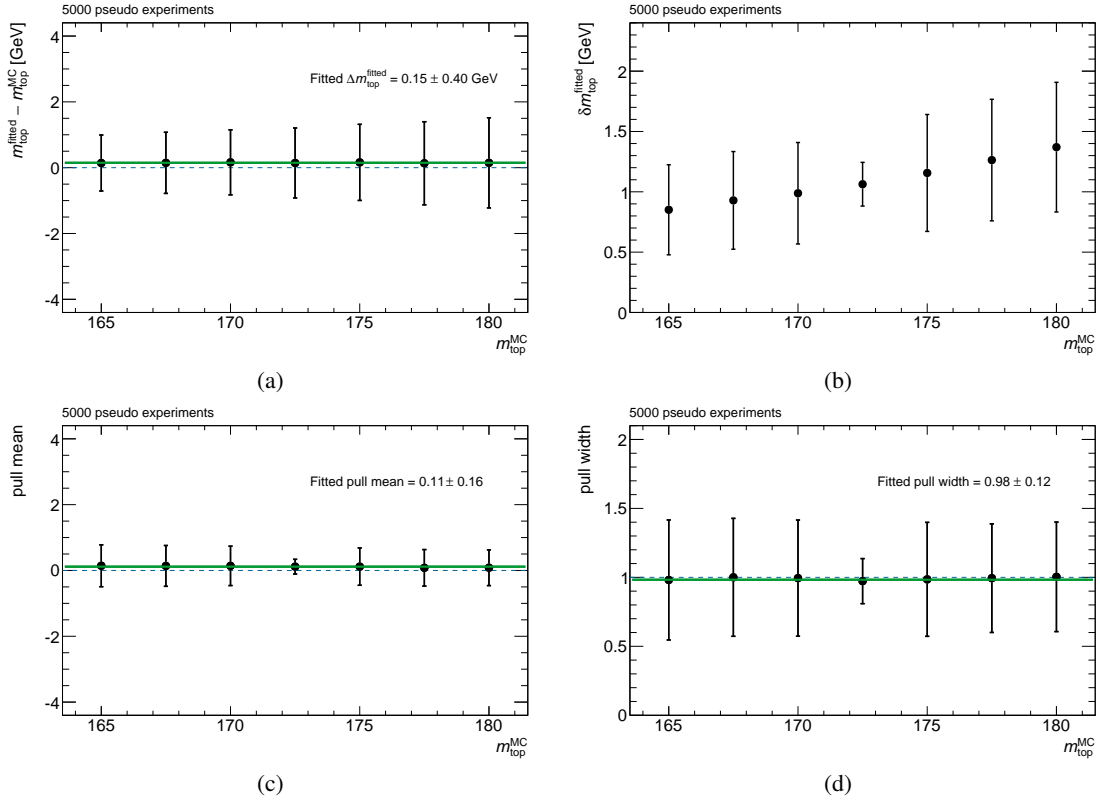


Figure C.7.: Results of pseudo experiments for different top quark mass parameters ranging from 165 to 180 GeV drawn from the templates itself. The plots are obtained by fitting the results of 5000 pseudo experiments for each mass value with a Gaussian function. Fig. (a) shows the mean of the fitted top quark mass distribution subtracted by the underlying MC top quark mass parameter, while Fig. (b) and Fig. (c) present the statistical error on the fitted top quark mass and the mean of the pull distributions. The fitted width of the pull distribution is shown in Fig. (d). The results of constant fits to each of the distributions presented in Fig. (a), Fig. (c) and Fig. (d) are shown in green and the corresponding values are given in the legend.



## D Split-up of lepton and jet related uncertainties

For the evaluation of the systematic uncertainties the ATLAS recommendations are adopted. In this context some of the systematics are split-up in independent sources of uncertainties. This is done in case of the lepton, jet energy resolution and jet energy scale systematic. For completeness the individual components (following the ATLAS naming convention, see Ref. [75, 77, 78, 94–96]) are listed in Tables D.1 - D.3.

Uncertainty	$\Delta m_{\text{top}}$ [GeV]	Up [GeV]	Down [GeV]
LepIdSF	0.15	0.15	-0.15
LepRecoSF	0.10	0.10	-0.10
LepTrigSF	0.00	0.00	0.00
Eer	0.03	0.03	-0.02
Ees	0.46	0.44	-0.48
Musc	0.07	0.07	-0.06
Muid_res	0.01	symmetric	symmetric
Mums_res	0.01	symmetric	symmetric
Total lepton systematics	0.50	0.48	-0.52

Table D.1.: Breakdown of the lepton related uncertainties. The uncertainties are calculated by building the average of the absolute difference of the up and down variation. In the case of the Muid\_res and Mums\_res components the difference to the nominal is quoted. The total uncertainty is calculated from the sum of squares of the individual components.

Uncertainty	$\Delta m_{\text{top}}$ [GeV]	Up [GeV]	Down [GeV]
Jer_np0	0.27	0.27	0.03
Jer_np1	0.04	-0.03	-0.04
Jer_np2	0.06	0.06	0.04
Jer_np3	0.03	-0.05	0.01
Jer_np4	0.10	0.00	0.10
Jer_np5	0.11	0.18	-0.03
Jer_np6	0.02	-0.02	0.00
Jer_np7	0.03	-0.05	0.01
Jer_np8	0.03	0.03	0.03
Jer_diff	0.02	symmetric	symmetric
Jer_noise_forward	0.01	symmetric	symmetric
Total jet energy resolution	0.32	0.34	-0.13

Table D.2.: Breakdown of the jet energy resolution uncertainty with its 11 components. Where applicable, the uncertainties are calculated by building the average of the absolute difference of the up and down variation. If the up and down variation have the same sign, the larger of the variations is used as systematic. In the case of the Jer\_diff and Jer\_noise\_forward components the difference to the nominal is quoted. The total uncertainty is calculated from the sum of squares of the individual components.

D. Split-up of lepton and jet related uncertainties

---

Uncertainty	$\Delta m_{\text{top}}$ [GeV]	Up [GeV]	Down [GeV]
BJesUnc	0.10	0.11	-0.09
EtaIntercalibrationModel	0.03	-0.03	0.00
EtaIntercalibrationTotalStat	0.01	0.01	0.00
Pileup_OffsetMu	0.04	0.04	0.01
Pileup_OffsetNPV	0.05	0.03	-0.06
Pileup_Pt	0.04	-0.02	0.05
Pileup_Rho	0.17	-0.17	0.16
SinglePart	0.02	0.01	0.02
Flavor_comp	0.40	-0.42	0.38
Flavor_response	0.29	0.28	-0.29
PunchThrough	0.02	0.00	0.02
JesEffectiveDet1	0.06	0.06	0.03
JesEffectiveDet2	0.07	0.02	0.07
JesEffectiveDet3	0.02	0.02	0.02
JesEffectiveMix1	0.05	0.05	0.02
JesEffectiveMix2	0.03	0.03	0.02
JesEffectiveMix3	0.02	0.01	0.02
JesEffectiveMix4	0.02	0.01	0.02
JesEffectiveModel1	0.21	-0.25	0.16
JesEffectiveModel2	0.03	0.03	0.02
JesEffectiveModel3	0.06	0.06	0.02
JesEffectiveModel4	0.03	0.03	0.02
JesEffectiveStat1	0.06	-0.06	0.05
JesEffectiveStat2	0.01	0.01	0.01
JesEffectiveStat3	0.08	0.08	0.00
JesEffectiveStat4	0.04	0.04	0.04
Total jet energy scale	0.60	0.62	-0.55

Table D.3.: Breakdown of the jet energy scale uncertainty with its 26 components. The uncertainties are calculated by building the average of the absolute difference of the up and down variation. If the up and down variation have the same sign, the larger of the variations is used as systematic. The total uncertainty is calculated from the sum of squares of the individual components.





## F Top quark transverse momentum reweighting

In this chapter additional information concerning the top quark transverse momentum reweighting procedure described in Chapter 8 is given. Table F.1 gives the numbers used for the reweighting to NNLO predictions and the corresponding up and down variations, obtained from Ref. [98]. Figure F.1 shows the influence of the up and down variation on the overall shift of the top quark mass due to the reweighting to NNLO order. Figure F.2 shows the same items as Fig. 6.5(a), 8.2 and F.1 but without any  $\Delta R_{jj}$  requirements.

(anti-)top $p_T$ [GeV]	0-10	10-20	20-30	30-40	40-50	50-60	60-70	70-80	80-90	90-100
Weighting factor	1.212	1.114	1.097	1.090	1.080	1.074	1.078	1.068	1.063	1.061
Up variation	1.299	1.183	1.156	1.146	1.131	1.123	1.127	1.111	1.107	1.101
Down variation	1.094	1.031	1.019	1.015	1.008	1.005	1.007	1.001	0.998	0.995
(anti-)top $p_T$ [GeV]	100-110	110-120	120-130	130-140	140-150	150-160	160-170	170-180	180-190	190-200
Weighting factor	1.060	1.058	1.050	1.052	1.042	1.045	1.036	1.035	1.033	1.031
Up variation	1.099	1.098	1.087	1.090	1.076	1.082	1.069	1.063	1.064	1.062
Down variation	0.997	0.994	0.988	0.988	0.983	0.985	0.977	0.977	0.975	0.972
(anti-)top $p_T$ [GeV]	200-220	220-240	240-260	260-280	280-300	300-320	320-340	340-360	360-380	380-400
Weighting factor	1.026	1.019	1.009	1.001	1.001	0.988	0.973	0.978	0.959	0.958
Up variation	1.053	1.043	1.033	1.023	1.018	1.007	0.981	0.987	0.966	0.967
Down variation	0.970	0.963	0.958	0.949	0.953	0.942	0.932	0.938	0.925	0.925

Table F.1.: Weighting factors, as well as their up and down variations, for the (anti-)top quark as a function of its transverse momentum, used to reweight the MC events to NNLO predictions. The numbers have been extracted from Ref. [98]. For each, the top quark and the anti-top quark, a weighting factor is obtained, depending on its truth  $p_T$ . The overall weighting factor for an event is then calculated as the geometrical mean of these two weights.

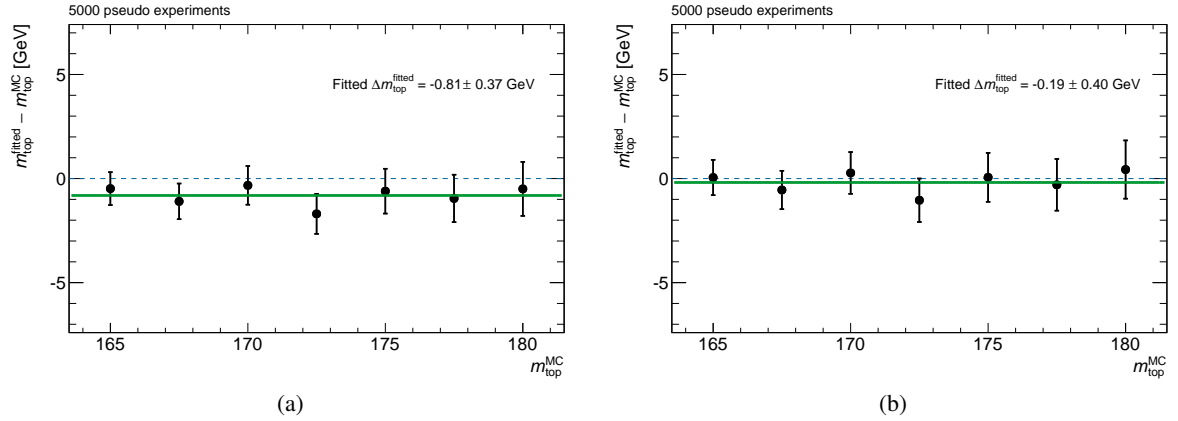


Figure F.1.: Result of 5000 pseudo experiments for the up and down variation of the NNLO reweighting, shown for the different MC top quark mass parameters. The weighting factors are varied up and down according to their uncertainties and the nominal template, used to extract the top quark mass from data, is applied to the reweighted events. In Fig. (a) the result of the up variation and in Fig. (b) the result of the down variation is shown. The uncertainty on the overall shift due to NNLO corrections is calculated as the difference of the fitted shift for the up and down variation and the shift obtained from the nominal NNLO reweighting. In addition, also the error on the shift itself is taken into account.

## F. Top quark transverse momentum reweighting

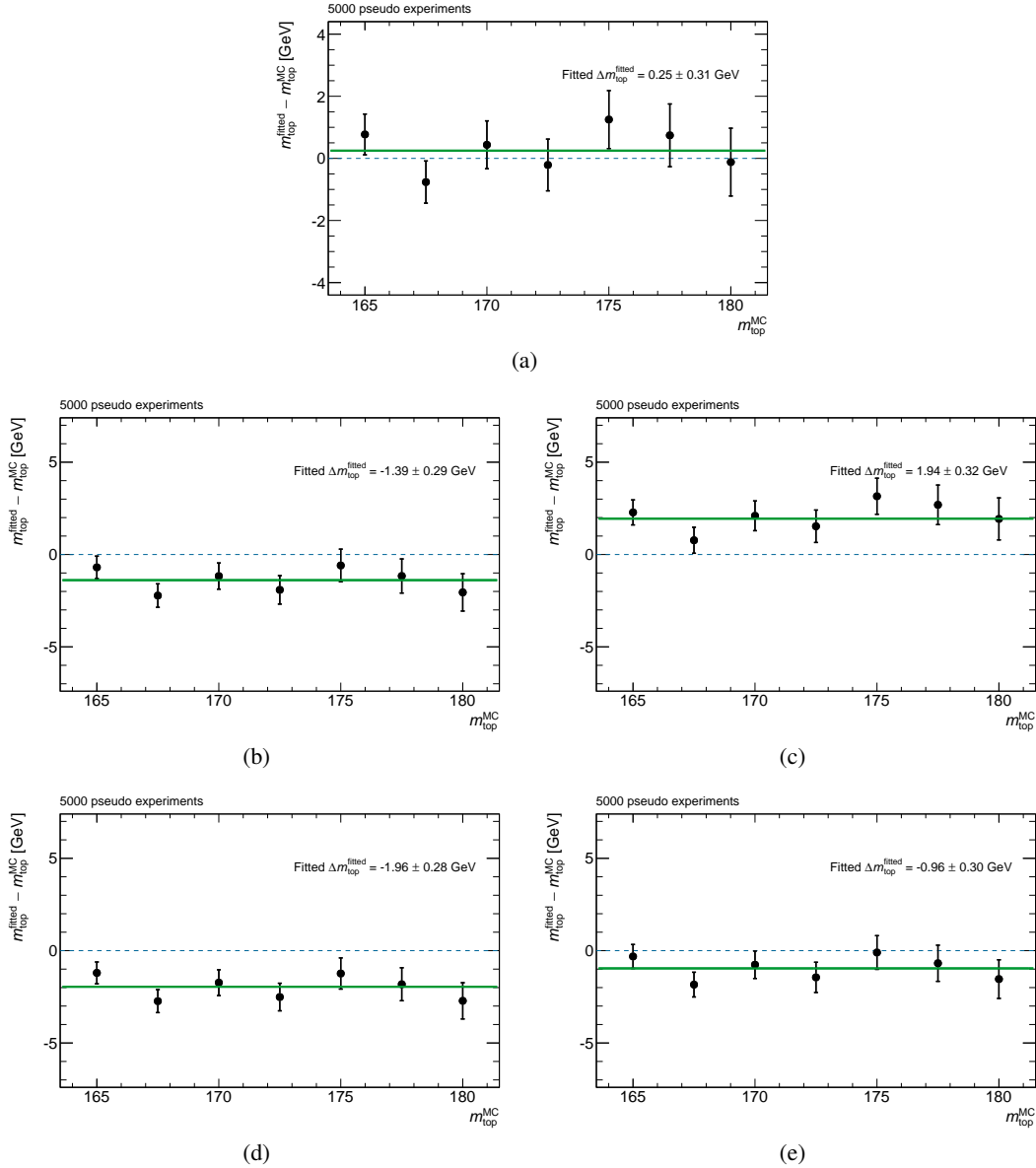


Figure F.2.: Result of 5000 pseudo experiments for the different MC top quark mass parameters without any cut on  $\Delta R_{jj}$ . Figure (a) shows the estimated bias of the top quark mass measurement derived as described in Chapter 6. In Fig. (b) the results of the nominal template, which is used to extract the top quark mass from data, applied to events reweighted to NNLO predictions are shown. In Fig. (c), the template is derived from the reweighted datasets and applied to the unweighted events. Both distributions are fitted by constants, which are shown in green. To estimate the overall influence on the final result of the measured top quark mass due to the reweighting to NNLO predictions, the fit results are compared to the number obtained from Fig. (a). In Fig. (d) the result of the up variation and in Fig. (e) the result of the down variation is shown. According to their uncertainties the weighting factors are varied up and down and the nominal template, used to extract the top quark mass from data, is applied to the reweighted events. The uncertainty on the overall shift due to NNLO corrections is calculated as the difference of the fitted shift for the up and down variation and the shift obtained from the nominal NNLO reweighting. In addition, also the error on the shift itself is taken into account.

## G Investigations due to the comparatively small top quark mass value

Since the measurement of the top quark mass in this analysis yields, compared to other measurements [8, 10–12, 14], a rather small value for  $m_{\text{top}}$ , different studies have been performed to exclude a systematic bias in the measurement. One thing which has been checked, is if the value of the top quark mass returned by the likelihood fit (as described in Chapter 6) corresponds to a global and not just to a local minimum. Therefore the likelihood distribution, obtained from the measured lepton transverse momenta, has been plotted as a function of  $m_{\text{top}}$ . As it can be seen in Fig. G.1 the fitted top quark mass corresponds to the global minimum of the distribution. Another check has been done by

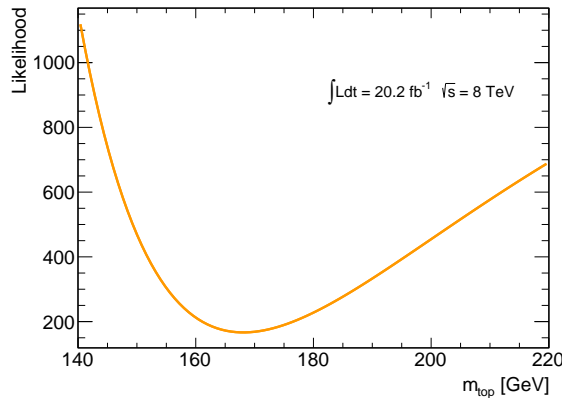


Figure G.1.: Likelihood function as it is obtained from the measured lepton transverse momentum distributions, plotted as a function of the top quark mass. The minimum of the distribution corresponds to the measured top quark mass.

varying some of the event selection requirements (cf. Chapter 5) of the analysis. For each variation in the selection, the analysis was redone (including the derivation of the templates) and the top quark mass has been measured. The following requirements have been changed separately:

- the cut on the 5<sup>th</sup> leading jet  $p_T$  has been omitted
- the jet multiplicity cut has been tightened, requiring exactly four jets in an event
- instead of two it has been asked for at least one  $b$ -tagged jet
- the  $E_T^{\text{miss}}$  requirement has been increased to 60 GeV in both channels

The template fits for these different selections are shown in Figs. G.3 - G.6 and can be compared to the nominal fit shown in Fig. G.2. The resulting values of the top quark mass for the different event selection requirements are shown in Table G.1. Within their uncertainties, the results are all compatible with each other and agree with the nominal result. As a further cross check the events have been split up according to their lepton charge and the analysis has been repeated for the positively and negatively charged lepton events separately. The corresponding template fits yield similar results, both in agreement with the nominal top quark mass result, and are shown in Fig. G.7. Furthermore the influence of the template parametrisation on the measured top quark mass has been studied. Different parametrisation of the lepton  $p_T$  distributions have been investigated, by replacing the Novosibirsk

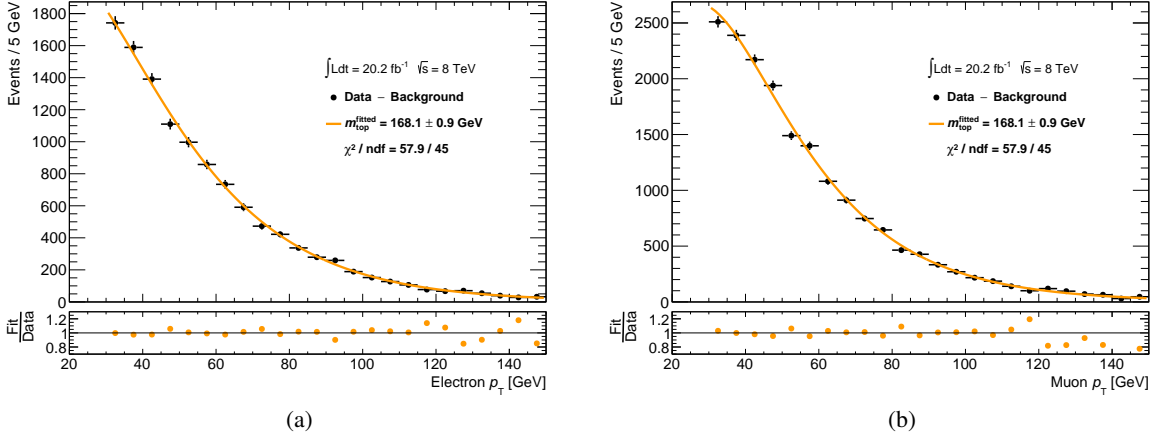


Figure G.2.: Template fit to the measured lepton transverse momentum distributions. Fig. (a) shows the fitted electron transverse momentum and Fig. (b) presents the fitted muon  $p_T$ . The data points are marked in black and the template fit is coloured orange. The measured top quark mass of  $168.1 \pm 0.9$  (stat) GeV is obtained by taking into account the electron and muon distribution simultaneously (and does not include the method calibration). The corresponding  $\chi^2/\text{ndf}$  value of the fit is given in the legend.

Selection requirement	$m_{\text{top}}$ [GeV]
Nominal selection	$168.1 \pm 0.9$
No Cut on the 5 <sup>th</sup> leading jet $p_T$	$168.3 \pm 0.9$
Exactly four jets	$169.0 \pm 1.0$
At least one $b$ -tagged jet	$166.8 \pm 0.7$
$E_T^{\text{miss}} > 60$ GeV	$166.8 \pm 1.7$

Table G.1.: Results for different modifications of the event selection requirements. The changes to the selection have been done separately and the analysis has been repeated for each. The results for the top quark mass are obtained by fitting the template to the measured lepton  $p_T$  distributions.

function with either a Fermi or a Crystal Ball distribution [99], and the impact on the final result has been estimated. The template fits derived with these functions are shown in Fig. G.8 and yield similar results for the measured top quark mass. In addition the impact of different fit ranges has been considered. Instead of taking into account the full range between 30 – 150 GeV for the lepton  $p_T$ , different  $p_T$  regions have been excluded from the fit. The results are shown in Fig. G.9 and the values obtained for  $m_{\text{top}}$  are in well agreement with the nominal result. Since, besides the missing higher order corrections in the simulation of the  $t\bar{t}$  transverse momentum, no systematic shift in the measured top quark mass has been found, it is concluded that the rather small value of  $m_{\text{top}}$  is a downwards fluctuation.

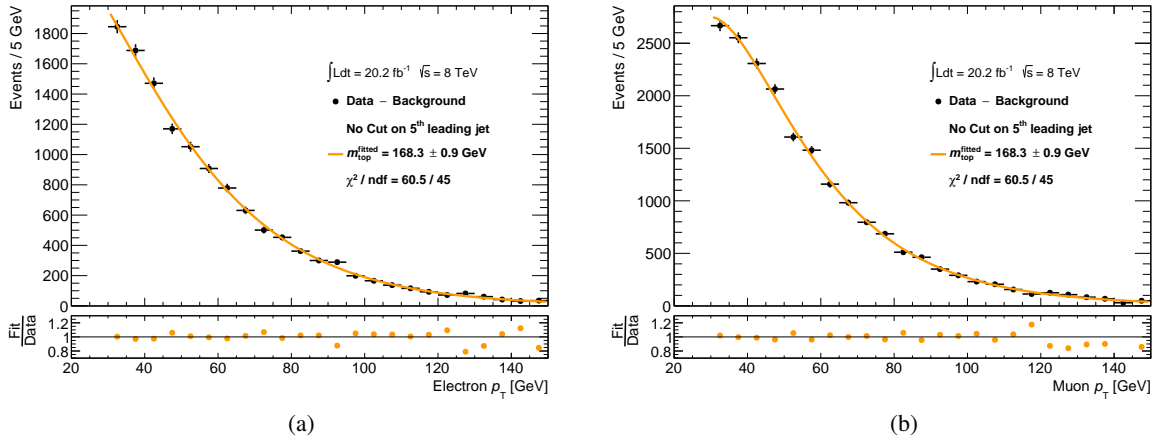


Figure G.3.: Figure (a) and Figure (b) show the fit to the measured electron and muon transverse momentum distribution, respectively. The analysis has been repeated with a modified event selection. Here, the requirement on the transverse momentum of the 5<sup>th</sup> leading jet has been omitted. The template has been optimised for the new selection and is fitted to data. The resulting top quark mass value agrees well with the nominal result (cf. Fig. G.2).

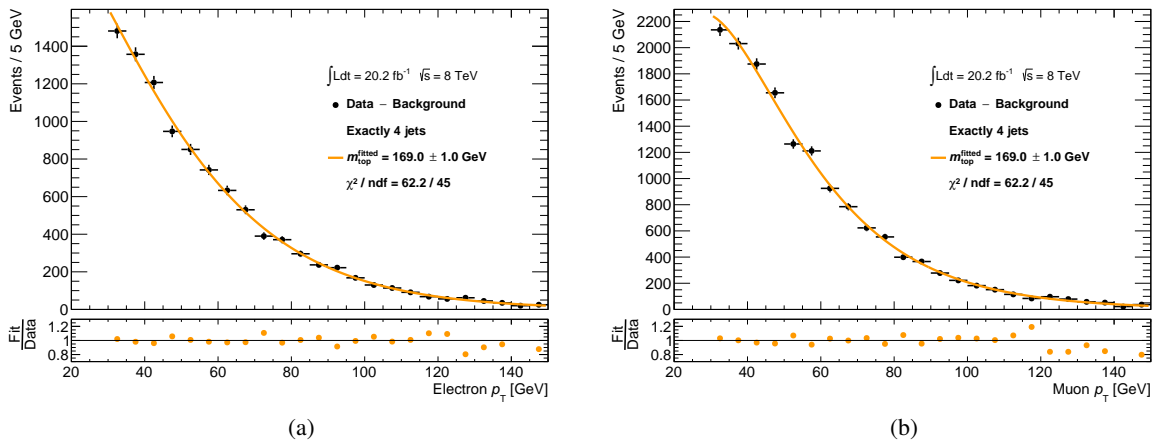


Figure G.4.: Figure (a) and Figure (b) show the fit to the measured electron and muon transverse momentum distributions. The analysis has been repeated with a modified event selection. Instead of requiring at least four jets in an event, only events with exactly four jets are selected. The template has been optimised for the new selection and is fitted to data. The resulting top quark mass value is in good agreement with the nominal result (cf. Fig. G.2).

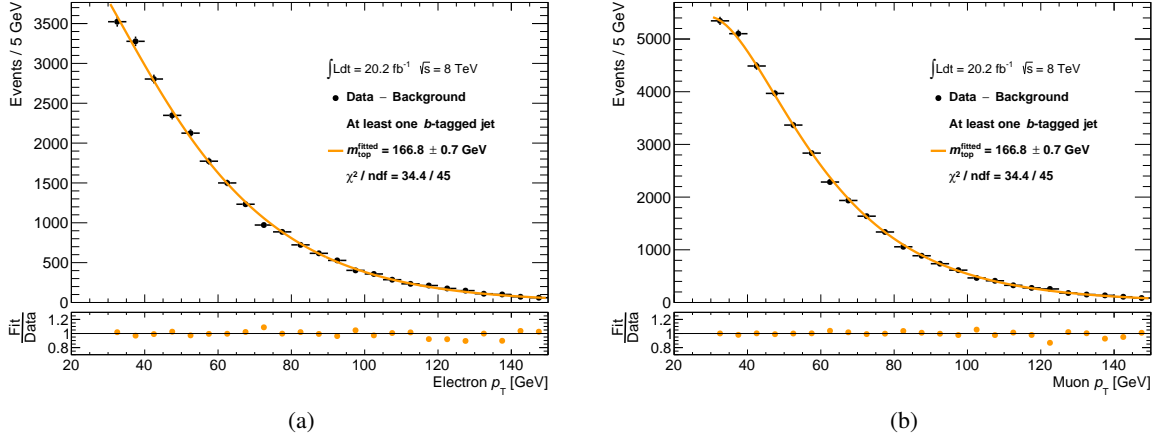


Figure G.5.: Figure (a) and Figure (b) show the fit to the measured electron and muon transverse momentum distributions. The analysis has been repeated with a modified event selection. Instead of asking for at least two  $b$ -tagged jets in an event, the selection requirement is eased to at least one  $b$ -tagged jet. The template has been optimised for the new selection and is fitted to data. The resulting top quark mass value is in agreement with the nominal result (cf. Fig. G.2).

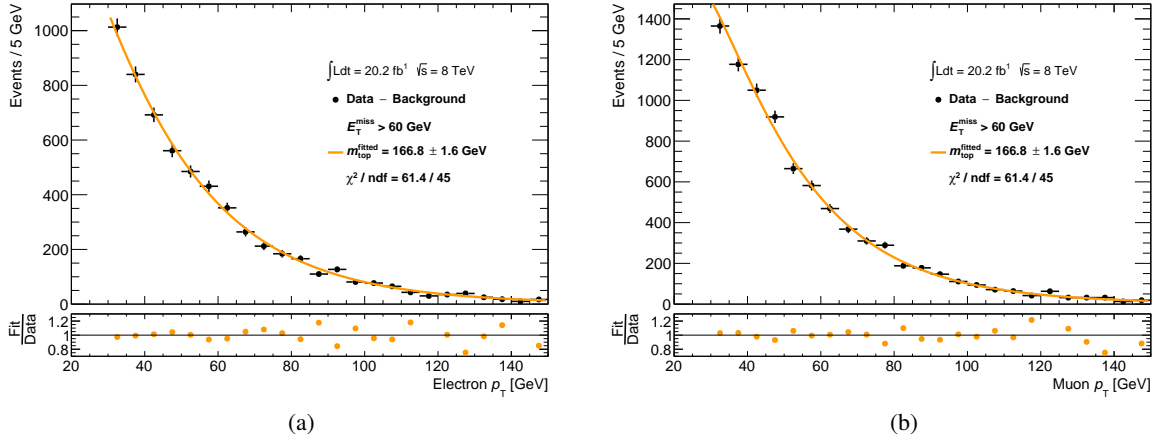


Figure G.6.: Figure (a) and Figure (b) show the fit to the measured electron and muon transverse momentum distributions. The analysis has been repeated with a modified event selection. Here, the  $E_T^{\text{miss}}$  requirement has been tightened and now asks for  $E_T^{\text{miss}} > 60$  GeV in both channels. The template has been optimised for the new selection and is fitted to data. Within its statistical uncertainty, the resulting top quark mass value agrees well with the nominal result (cf. Fig. G.2).

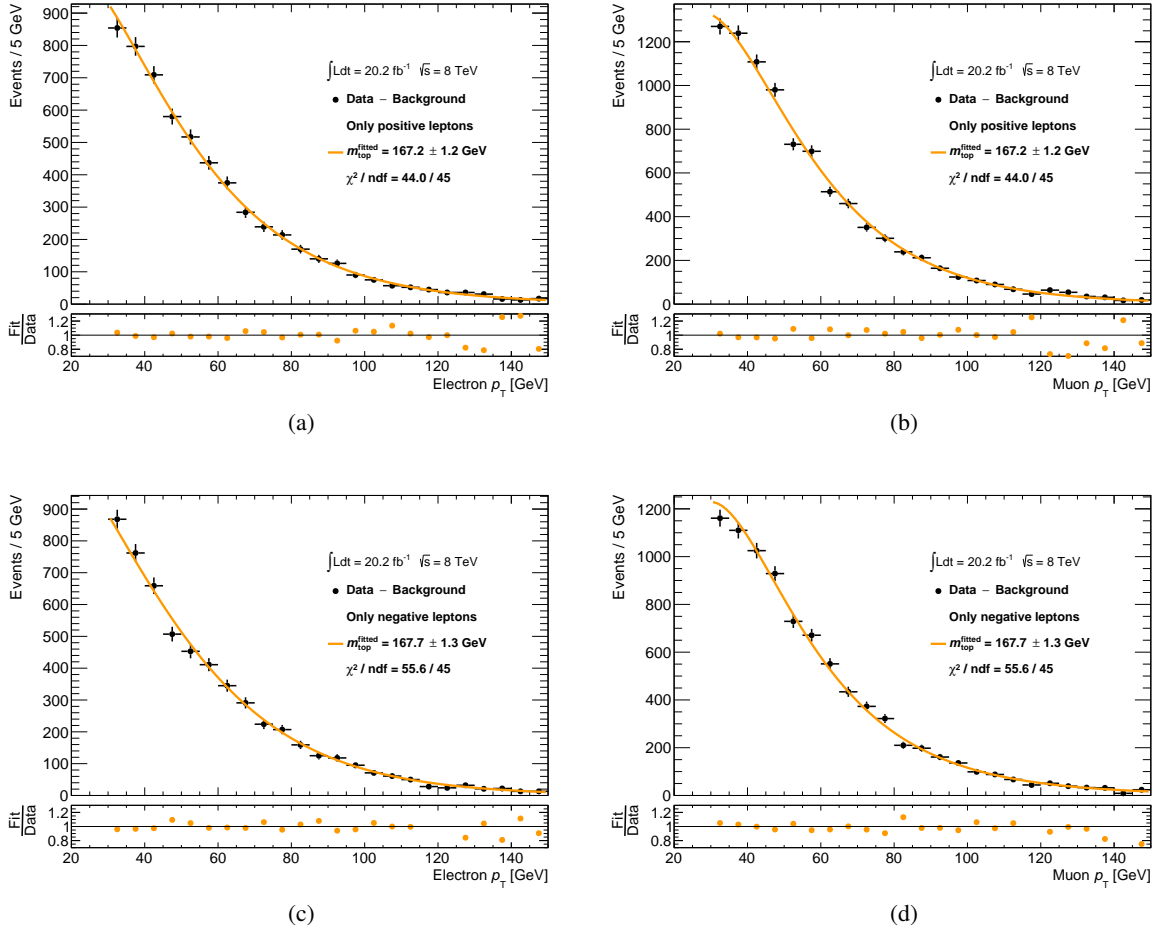


Figure G.7.: Fit to the measured electron and muon transverse momentum distributions. For Fig. (a) and Fig. (b) only events with a positively charged lepton are taken into account in the top quark mass measurement, while for Fig. (c) and Fig. (d) only events with a negatively charged lepton are used. Within their statistical precision, the measured top quark mass values agree well with each other (cf. Fig. G.2).

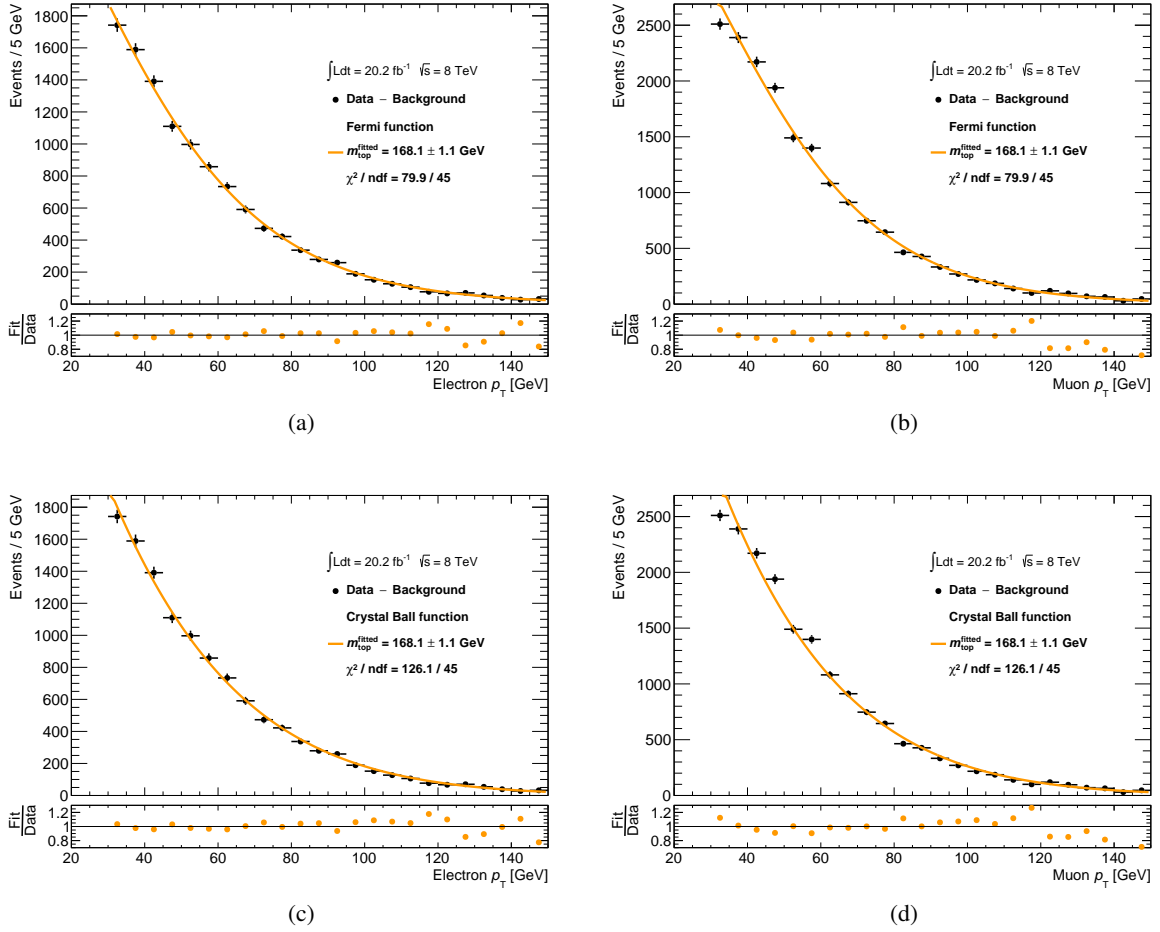


Figure G.8.: Fit to the measured electron and muon transverse momentum distributions with altered parametrisation. In Fig. (a) and Fig. (b) the top quark mass has been measured with a modified template, which has been created by replacing the Novosibirsk function with a Fermi distribution. The same is done in Fig. (c) and Fig. (d) but there a Crystal Ball function is used, instead. The measured top quark mass values are in well agreement with the nominal value (cf. Fig. G.2).

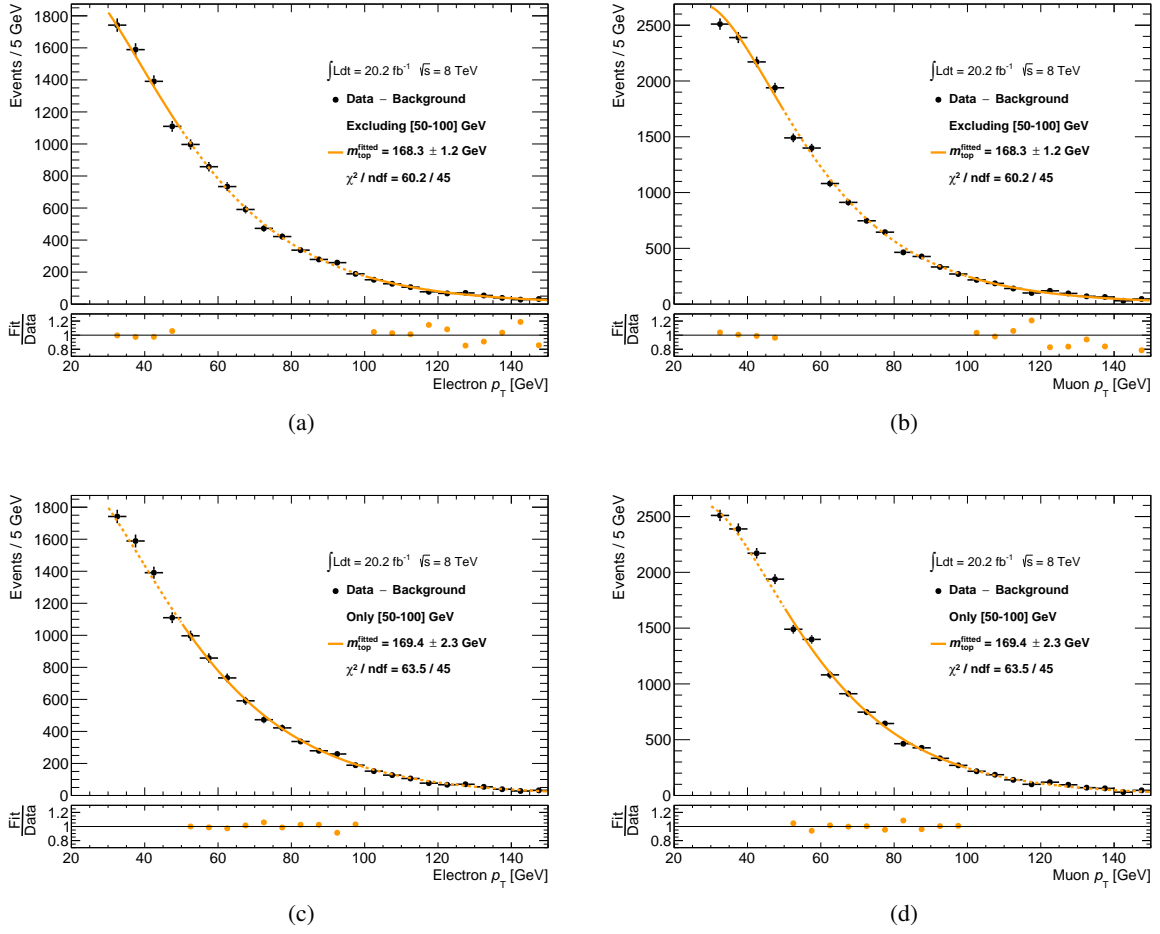


Figure G.9.: Fit to the measured electron and muon transverse momentum distributions with varied fit ranges. In Fig. (a) and Fig. (b) the range between 50 – 100 GeV is excluded in the template fit, while in Fig. (c) and Fig. (d) only this range is included in the fit. The measured top quark mass values agree well within their statistical precision (cf. Fig. G.2).



## Bibliography

- [1] A. Einstein, *Die Grundlage der allgemeinen Relativitätstheorie*, *Annalen der Physik* **354** (1916) 769, URL: <http://dx.doi.org/10.1002/andp.19163540702>.
- [2] LIGO Scientific Collaboration and Virgo Collaboration, B. P. Abbott *et al.*, *Observation of Gravitational Waves from a Binary Black Hole Merger*, *Phys. Rev. Lett.* **116** (6 2016) 061102, URL: <http://dx.doi.org/10.1103/PhysRevLett.116.061102>.
- [3] M. Kobayashi and T. Maskawa, *CP Violation in the Renormalizable Theory of Weak Interaction*, *Prog. Theor. Phys.* **49** (1973) 652, URL: <http://dx.doi.org/10.1143/PTP.49.652>.
- [4] CDF Collaboration, F. Abe *et al.*, *Observation of Top Quark Production in  $\bar{p}p$  Collisions with the Collider Detector at Fermilab*, *Phys. Rev. Lett.* **74** (1995) 2626, URL: <http://dx.doi.org/10.1103/PhysRevLett.74.2626>.
- [5] D0 Collaboration, S. Abachi *et al.*, *Observation of the Top Quark*, *Phys. Rev. Lett.* **74** (1995) 2632, URL: <http://dx.doi.org/10.1103/PhysRevLett.74.2632>.
- [6] M. Baak *et al.*, *The global electroweak fit at NNLO and prospects for the LHC and ILC*, *The European Physical Journal C* **74** (2014) 1, URL: <http://dx.doi.org/10.1140/epjc/s10052-014-3046-5>.
- [7] G. Degrossi *et al.*, *Higgs mass and vacuum stability in the Standard Model at NNLO*, *Journal of High Energy Physics* **2012** (2012) 98, URL: [http://dx.doi.org/10.1007/JHEP08\(2012\)098](http://dx.doi.org/10.1007/JHEP08(2012)098).
- [8] ATLAS Collaboration, *Measurement of the top quark mass in the  $t\bar{t} \rightarrow$  lepton+jets and  $t\bar{t} \rightarrow$  dilepton channels using  $\sqrt{s} = 7$  TeV ATLAS data*, *Eur. Phys. J. C* **75** (2015) 330, URL: <http://dx.doi.org/10.1140/epjc/s10052-015-3544-0>.
- [9] ATLAS Collaboration, *Measurement of the top-quark mass in the fully hadronic decay channel from ATLAS data at  $\sqrt{s} = 7$  TeV*, *Eur. Phys. J. C* **75** (2015) 158, URL: <http://dx.doi.org/10.1140/epjc/s10052-015-3373-1>.
- [10] ATLAS Collaboration, *Measurement of the top quark mass in the  $t\bar{t} \rightarrow$  dilepton channel from  $\sqrt{s} = 8$  TeV ATLAS data*, *Physics Letters B* **761** (2016) 350, URL: <http://dx.doi.org/10.1016/j.physletb.2016.08.042>.
- [11] ATLAS Collaboration, *Top-quark mass measurement in the all-hadronic top-antitop quark decay channel at  $\sqrt{s} = 8$  TeV with the ATLAS detector*, ATLAS-CONF-2016-064, 2016, URL: <http://cds.cern.ch/record/2206204>.
- [12] CMS Collaboration, *Measurement of the top quark mass using proton–proton data at  $\sqrt{s} = 7$  and 8 TeV*, *Phys. Rev. D* **93** (2016) 072004, URL: <http://dx.doi.org/10.1103/PhysRevD.93.072004>.
- [13] M. Bender, *Measurements of the top-quark mass using the ATLAS detector at the LHC*, PoS DIS2016 (2016) 149, URL: <http://inspirehep.net/record/1497397>.

- [14] ATLAS, CDF, CMS and DØ Collaborations, *First combination of Tevatron and LHC measurements of the top-quark mass*, ATLAS-CONF-2014-008, 2014, URL: <http://cdsweb.cern.ch/record/1669702>.
- [15] CDF Collaboration, T. Aaltonen *et al.*, *Measurement of the top quark mass in the channel using the lepton transverse momentum*, *Physics Letters B* **698** (2011) 371, URL: <http://dx.doi.org/10.1016/j.physletb.2011.03.041>.
- [16] ATLAS Collaboration, *Observation of a new particle in the search for the Standard Model Higgs boson with the ATLAS detector at the LHC*, *Phys. Lett. B* **716** (2012) 1, URL: <http://dx.doi.org/10.1016/j.physletb.2012.08.020>.
- [17] CMS Collaboration, *Observation of a new boson at a mass of 125 GeV with the CMS experiment at the LHC*, *Phys. Lett. B* **716** (2012) 30, URL: <http://dx.doi.org/10.1016/j.physletb.2012.08.021>.
- [18] K. Olive and P. D. Group, *Review of Particle Physics*, *Chinese Physics C* **38** (2014) 090001, URL: <http://stacks.iop.org/1674-1137/38/i=9/a=090001>.
- [19] G. Dissertori, I. Knowles and M. Schmelling, *Quantum Chromodynamics*, 1st ed., Oxford University Press, 2003.
- [20] L. Hoddeson *et al.*, *The Rise of the Standard Model*, 1st ed., Cambridge University Press, 1997.
- [21] G. 't Hooft and M. Veltman, *Regularization and renormalization of gauge fields*, *Nuclear Physics B* **44** (1972) 189, URL: [http://dx.doi.org/10.1016/0550-3213\(72\)90279-9](http://dx.doi.org/10.1016/0550-3213(72)90279-9).
- [22] F. Halzen and A. D. Martin, *Quarks and Leptons*, 1st ed., John Wiley and Sons, 1984.
- [23] R. E. Marshak, *Conceptual Foundation of Modern Particle Physics*, 1st ed., World Scientific, 1993.
- [24] D. Griffiths, *Introduction to Elementary Particles*, 2nd ed., Wiley-VCH Verlag GmbH und Co. KGaA, 2008.
- [25] K. Bethge and U. Schroeder, *Elementarteilchen und ihre Wechselwirkungen*, 3rd ed., Wiley-VCH Verlag GmbH und Co. KGaA, 2006.
- [26] S. Mele, *Measurements of the running of the electromagnetic coupling at LEP*, *26th International Symposium on Physics in Collision (PIC 2006)*, 2006, URL: <https://inspirehep.net/record/728976>.
- [27] S. Bethke, *World Summary of  $\alpha_s$  (2012)*, *Nucl. Phys. Proc. Suppl.* **234** (2013) 229, URL: <http://dx.doi.org/10.1016/j.nuclphysbps.2012.12.020>.
- [28] R. Aaij *et al.*, *Observation of  $J/\psi p$  Resonances Consistent with Pentaquark States in  $\Lambda_b^0 \rightarrow J/\psi K^- p$  Decays*, *Phys. Rev. Lett.* **115** (2015) 072001, URL: <http://dx.doi.org/10.1103/PhysRevLett.115.072001>.
- [29] F. Englert and R. Brout, *Broken Symmetry and the Mass of Gauge Vector Mesons*, *Phys. Rev. Lett.* **13** (9 1964) 321, URL: <http://dx.doi.org/10.1103/PhysRevLett.13.321>.

- 
- [30] P. W. Higgs, *Broken Symmetries and the Masses of Gauge Bosons*, *Phys. Rev. Lett.* **13** (16 1964) 508,  
URL: <http://dx.doi.org/10.1103/PhysRevLett.13.508>.
- [31] D. H. Perkins, *Introduction to High Energy Physics*, 4th ed.,  
Cambridge University Press, 2000.
- [32] H. Georgi, *Weak Interactions and Modern Particle Theory*, 1st ed.,  
The Benjamin/Cummings Publishing Company, Inc., 1984.
- [33] N. Cabibbo, *Unitary Symmetry and Leptonic Decays*, *Phys. Rev. Lett.* **10** (12 1963) 531,  
URL: <http://dx.doi.org/10.1103/PhysRevLett.10.531>.
- [34] LHCTopWG, *Summary plots from the ATLAS Top physics group*, 2016,  
URL: <http://atlas.web.cern.ch/Atlas/GROUPS/PHYSICS/CombinedSummaryPlots/TOP/> (visited on 28/11/2016).
- [35] A. D. Martin et al., *Parton distributions for the LHC*, *Eur. Phys. J.* **C63** (2009) 189,  
URL: <http://dx.doi.org/10.1140/epjc/s10052-009-1072-5>.
- [36] N. Kidonakis, *Differential and total cross sections for top pair and single top production*, 20th International Workshop on Deep-Inelastic Scattering and Related Subjects, DESY, 26th2012 831, URL: <http://dx.doi.org/10.3204/DESY-PROC-2012-02/251>.
- [37] ATLAS Collaboration, *Measurement of the Inclusive and Fiducial Cross-Section of Single Top-Quark  $t$ -Channel Events in  $pp$  Collisions at  $\sqrt{s} = 8$  TeV*, ATLAS-CONF-2014-007, 2014, URL: <http://cdsweb.cern.ch/record/1668960>.
- [38] ATLAS Collaboration, *Search for  $s$ -channel single top-quark production in proton–proton collisions at  $\sqrt{s} = 8$  TeV with the ATLAS detector*, *Phys. Lett. B* **740** (2015) 118,  
URL: <http://dx.doi.org/10.1016/j.physletb.2014.11.042>.
- [39] ATLAS Collaboration, *Measurement of the production cross-section of a single top quark in association with a  $W$  boson at 8 TeV with the ATLAS experiment*, *JHEP* **01** (2016) 064,  
URL: [http://dx.doi.org/10.1007/JHEP01\(2016\)064](http://dx.doi.org/10.1007/JHEP01(2016)064).
- [40] ATLAS Collaboration, *Measurement of the  $t\bar{t}$  production cross-section using  $e\mu$  events with  $b$ -tagged jets in  $pp$  collisions at  $\sqrt{s} = 7$  and 8 TeV with the ATLAS detector*, *Eur. Phys. J. C* **74** (2014) 3109,  
URL: <http://dx.doi.org/10.1140/epjc/s10052-014-3109-7>.
- [41] A. H. Hoang, *The Top Mass: Interpretation and Theoretical Uncertainties*, *Proceedings, 7th International Workshop on Top Quark Physics (TOP2014)*, 2014,  
URL: <https://inspirehep.net/record/1333866>.
- [42] C. Lefèvre, *The CERN accelerator complex. Complexe des accélérateurs du CERN*, 2008,  
URL: <http://cds.cern.ch/record/1260465>.
- [43] O. S. Brüning et al., *LHC Design Report*, CERN, 2004,  
URL: <http://cds.cern.ch/record/782076>.
- [44] J.-L. Caron,  
*The first 15m dipole in the SM18 test hall. Premier dipole de 15m dans le hall de tests SM18.*  
AC Collection. Legacy of AC. Pictures from 1992 to 2002., 1998,  
URL: <http://cds.cern.ch/record/842089>.

- [45] ATLAS Collaboration, *Pile-up subtraction and suppression for jets in ATLAS*, ATLAS-CONF-2013-083, 2013, URL: <http://cdsweb.cern.ch/record/1570994>.
- [46] M. Lamont, *Status of the LHC*, Journal of Physics: Conference Series **455** (2013) 012001, URL: <http://stacks.iop.org/1742-6596/455/i=1/a=012001>.
- [47] J. Pequenaο, *Computer generated image of the whole ATLAS detector*, 2008, URL: <http://cds.cern.ch/record/1095924>.
- [48] ATLAS Collaboration, *The ATLAS Experiment at the CERN Large Hadron Collider*, **JINST 3** (2008) S08003, URL: <http://dx.doi.org/10.1088/1748-0221/3/08/S08003>.
- [49] ATLAS Collaboration, *ATLAS magnet system: Technical Design Report, 1*, Technical Design Report ATLAS, CERN, 1997, URL: <http://cds.cern.ch/record/338080>.
- [50] ATLAS Collaboration, *Readiness of the ATLAS liquid argon calorimeter for LHC collisions*, **Eur. Phys. J. C 70** (2010) 723, URL: <http://dx.doi.org/10.1140/epjc/s10052-010-1354-y>.
- [51] ATLAS Collaboration, *ATLAS tile calorimeter: Technical Design Report*, Technical Design Report ATLAS, CERN, 1996, URL: <http://cds.cern.ch/record/331062>.
- [52] ATLAS Collaboration, *ATLAS calorimeter performance Technical Design Report*, Technical Design Report ATLAS, CERN, 1996, URL: <https://inspirehep.net/record/432293>.
- [53] O. Igonkina, *ATLAS Trigger Menu and Performance in Run I and Prospects for Run II*, tech. rep. ATL-DAQ-PROC-2013-042, CERN, 2013, URL: <http://cds.cern.ch/record/1629313>.
- [54] C. Eck et al., *LHC computing Grid: Technical Design Report. Version 1.06 (20 Jun 2005)*, Technical Design Report LCG, CERN, 2005, URL: <http://cds.cern.ch/record/840543>.
- [55] J. Pequenaο, *Computer generated image of the ATLAS inner detector*, 2008, URL: <http://cds.cern.ch/record/1095926>.
- [56] J. Pequenaο, *Computer Generated image of the ATLAS calorimeter*, 2008, URL: <http://cds.cern.ch/record/1095927>.
- [57] J. Pequenaο, *Computer generated image of the ATLAS Muons subsystem*, 2008, URL: <http://cds.cern.ch/record/1095929>.
- [58] M. H. Seymour and M. Marx, *Monte Carlo Event Generators*, *69th Scottish Universities Summer School in Physics: LHC Phenomenology (SUSSP69)*, 2013 287, URL: [http://dx.doi.org/10.1007/978-3-319-05362-2\\_8](http://dx.doi.org/10.1007/978-3-319-05362-2_8).
- [59] P. Nason, *A new method for combining NLO QCD with shower Monte Carlo algorithms*, **Journal of High Energy Physics** (2004) 040, URL: <http://dx.doi.org/10.1088/1126-6708/2004/11/040>.
- [60] S. Frixione, P. Nason and C. Oleari, *Matching NLO QCD computations with parton shower simulations: the POWHEG method*, **Journal of High Energy Physics** (2007) 070, URL: <http://dx.doi.org/10.1088/1126-6708/2007/11/070>.

- 
- [61] S. Alioli et al., *A general framework for implementing NLO calculations in shower Monte Carlo programs: the POWHEG BOX*, *Journal of High Energy Physics* (2010) 1, URL: [http://dx.doi.org/10.1007/JHEP06\(2010\)043](http://dx.doi.org/10.1007/JHEP06(2010)043).
- [62] H.-L. Lai et al., *New parton distributions for collider physics*, *Phys. Rev. D* **82** (7 2010) 074024, URL: <http://dx.doi.org/10.1103/PhysRevD.82.074024>.
- [63] T. Sjöstrand, S. Mrenna and P. Skands, *PYTHIA 6.4 physics and manual*, *Journal of High Energy Physics* (2006) 026, URL: <http://dx.doi.org/10.1088/1126-6708/2006/05/026>.
- [64] P. Z. Skands, *Tuning Monte Carlo generators: The Perugia tunes*, *Phys. Rev. D* **82** (7 2010) 074018, URL: <http://dx.doi.org/10.1103/PhysRevD.82.074018>.
- [65] J. Pumplin et al., *New Generation of Parton Distributions with Uncertainties from Global QCD Analysis*, *Journal of High Energy Physics* (2002) 012, URL: <http://dx.doi.org/10.1088/1126-6708/2002/07/012>.
- [66] B. P. Kersevan and E. Richter-Was, *The Monte Carlo event generator AcerMC versions 2.0 to 3.8 with interfaces to PYTHIA 6.4, HERWIG 6.5 and ARIADNE 4.1*, *Comput. Phys. Commun.* **184** (2013) 919, URL: <http://dx.doi.org/10.1016/j.cpc.2012.10.032>.
- [67] M. L. Mangano et al., *ALPGEN, a generator for hard multiparton processes in hadronic collisions*, *Journal of High Energy Physics* (2003) 001, URL: <http://dx.doi.org/10.1088/1126-6708/2003/07/001>.
- [68] G. Corcella et al., *HERWIG 6: an event generator for hadron emission reactions with interfering gluons (including supersymmetric processes)*, *Journal of High Energy Physics* (2001) 010, URL: <http://dx.doi.org/10.1088/1126-6708/2001/01/010>.
- [69] ATLAS Collaboration, *New ATLAS event generator tunes to 2010 data*, ATL-PHYS-PUB-2011-008, 2011, URL: <http://cds.cern.ch/record/1345343>.
- [70] ATLAS Collaboration, *The ATLAS Simulation Infrastructure*, *Eur. Phys. J. C* **70** (2010) 823, URL: <http://dx.doi.org/10.1140/epjc/s10052-010-1429-9>.
- [71] S. Agostinelli et al., *GEANT4: A Simulation toolkit*, *Nucl. Instrum. Meth.* **A506** (2003) 250, URL: [http://dx.doi.org/10.1016/S0168-9002\(03\)01368-8](http://dx.doi.org/10.1016/S0168-9002(03)01368-8).
- [72] ATLAS Collaboration, *The simulation principle and performance of the ATLAS fast calorimeter simulation FastCaloSim*, ATL-PHYS-PUB-2010-013, 2010, URL: <http://cds.cern.ch/record/1300517>.
- [73] W. Lampl et al., *Calorimeter Clustering Algorithms: Description and Performance*, tech. rep. ATL-LARG-PUB-2008-002, CERN, 2008, URL: <http://cds.cern.ch/record/1099735>.
- [74] M. Cacciari, G. P. Salam and G. Soyez, *The anti- $k_t$  jet clustering algorithm*, *Journal of High Energy Physics* (2008) 063, URL: <http://dx.doi.org/10.1088/1126-6708/2008/04/063>.

- [75] ATLAS Collaboration, *Monte Carlo Calibration and Combination of In-situ Measurements of Jet Energy Scale, Jet Energy Resolution and Jet Mass in ATLAS*, ATLAS-CONF-2015-037, 2015, URL: <http://cdsweb.cern.ch/record/2044941>.
- [76] ATLAS Collaboration, *Selection of jets produced in proton–proton collisions with the ATLAS detector using 2011 data*, ATLAS-CONF-2012-020, 2012, URL: <http://cdsweb.cern.ch/record/1430034>.
- [77] ATLAS Collaboration, *Electron efficiency measurements with the ATLAS detector using the 2012 LHC proton–proton collision data*, ATLAS-CONF-2014-032, 2014, URL: <http://cdsweb.cern.ch/record/1706245>.
- [78] ATLAS Collaboration, *Measurement of the muon reconstruction performance of the ATLAS detector using 2011 and 2012 LHC proton–proton collision data*, *Eur. Phys. J. C* **74** (2014) 3130, URL: <http://dx.doi.org/10.1140/epjc/s10052-014-3130-x>.
- [79] ATLAS Collaboration, *Performance of Missing Transverse Momentum Reconstruction in ATLAS studied in Proton–Proton Collisions recorded in 2012 at  $\sqrt{s} = 8$  TeV*, ATLAS-CONF-2013-082, 2013, URL: <http://cdsweb.cern.ch/record/1570993>.
- [80] ATLAS Collaboration, *Performance of b-Jet Identification in the ATLAS Experiment*, *JINST* **11** (2016) P04008, URL: <http://dx.doi.org/10.1088/1748-0221/11/04/P04008>.
- [81] ATLAS Collaboration, *Estimation of non-prompt and fake lepton backgrounds in final states with top quarks produced in proton–proton collisions at  $\sqrt{s} = 8$  TeV with the ATLAS Detector*, ATLAS-CONF-2014-058, 2014, URL: <http://cdsweb.cern.ch/record/1951336>.
- [82] H. Ikeda et al., *A detailed test of the CsI(Tl) calorimeter for BELLE with photon beams of energy between 20 MeV and 5.4 GeV*, *Nucl. Instrum. Meth. A* **441** (2000) 401, URL: [http://dx.doi.org/10.1016/S0168-9002\(99\)00992-4](http://dx.doi.org/10.1016/S0168-9002(99)00992-4).
- [83] R. Barlow, *Application of the bootstrap resampling technique to particle physics experiments*, Manchester University Preprint, MAN/HEP/99/ (1999), URL: <http://www.hep.man.ac.uk/preprints/1999.html>.
- [84] R. Barlow, *Systematic errors: Facts and fictions*, *Advanced Statistical Techniques in Particle Physics. Proceedings, Conference, Durham, UK, March 18-22, 2002* 134, URL: <http://inspirehep.net/record/590094>.
- [85] S. Frixione and B. R. Webber, *Matching NLO QCD computations and parton shower simulations*, *Journal of High Energy Physics* (2002) 029, URL: <http://dx.doi.org/10.1088/1126-6708/2002/06/029>.
- [86] S. Frixione, P. Nason and B. R. Webber, *Matching NLO QCD and parton showers in heavy flavour production*, *Journal of High Energy Physics* (2003) 007, URL: <http://dx.doi.org/10.1088/1126-6708/2003/08/007>.
- [87] S. Frixione et al., *Single-top hadroproduction in association with a W boson*, *Journal of High Energy Physics* (2008) 029, URL: <http://dx.doi.org/10.1088/1126-6708/2008/07/029>.

- 
- [88] B. Andersson et al., *Parton fragmentation and string dynamics*, **Physics Reports** **97** (1983) 31, URL: [http://dx.doi.org/10.1016/0370-1573\(83\)90080-7](http://dx.doi.org/10.1016/0370-1573(83)90080-7).
- [89] B. Andersson, *The Lund Model*, Cambridge Monographs on Particle Physics, Nuclear Physics and Cosmology (No. 7), 1998, ISBN: 0521017343, URL: <http://lccn.loc.gov/2006274063>.
- [90] B. Webber, *A QCD model for jet fragmentation including soft gluon interference*, **Nuclear Physics B** **238** (1984) 492, URL: [http://dx.doi.org/10.1016/0550-3213\(84\)90333-X](http://dx.doi.org/10.1016/0550-3213(84)90333-X).
- [91] ATLAS Collaboration, *Comparison of Monte Carlo generator predictions for gap fraction and jet multiplicity observables in  $t\bar{t}$  events*, ATL-PHYS-PUB-2014-005, 2014, URL: <http://cdsweb.cern.ch/record/1703034>.
- [92] J. Butterworth et al., *PDF4LHC recommendations for LHC Run II*, **J. Phys.** **G43** (2016) 023001, URL: <http://dx.doi.org/10.1088/0954-3899/43/2/023001>.
- [93] R. D. Ball et al., *A first unbiased global NLO determination of parton distributions and their uncertainties*, **Nucl. Phys.** **B838** (2010) 136, URL: <http://dx.doi.org/10.1016/j.nuclphysb.2010.05.008>.
- [94] ATLAS Collaboration, *Electron and photon energy calibration with the ATLAS detector using LHC Run 1 data*, **Eur. Phys. J. C** **74** (2014) 3071, URL: <http://dx.doi.org/10.1140/epjc/s10052-014-3071-4>.
- [95] ATLAS Collaboration, *Data-driven determination of the energy scale and resolution of jets reconstructed in the ATLAS calorimeters using dijet and multijet events at  $\sqrt{s} = 8$  TeV*, ATLAS-CONF-2015-017, 2015, URL: <http://cdsweb.cern.ch/record/2008678>.
- [96] ATLAS Collaboration, *Determination of the jet energy scale and resolution at ATLAS using  $Z/\gamma$ -jet events in data at  $\sqrt{s} = 13$  TeV*, ATLAS-CONF-2015-057, 2015, URL: <http://cdsweb.cern.ch/record/2059846>.
- [97] ATLAS Collaboration, *Measurements of top-quark pair differential cross-sections in the lepton+jets channel in pp collisions at  $\sqrt{s} = 8$  TeV using the ATLAS detector*, **The European Physical Journal C** **76** (2016) 538, URL: <http://dx.doi.org/10.1140/epjc/s10052-016-4366-4>.
- [98] M. Czakon, D. Heymes and A. Mitov, *High-Precision Differential Predictions for Top-Quark Pairs at the LHC*, **Phys. Rev. Lett.** **116** (8 2016) 082003, URL: <http://dx.doi.org/10.1103/PhysRevLett.116.082003>.
- [99] J. Gaiser, *Charmonium Spectroscopy From Radiative Decays of the  $J/\psi$  and  $\psi'$* , PhD thesis: SLAC, 1982, URL: <http://inspirehep.net/record/183554>.



## List of Figures

2.1	Electron-electron scattering via the exchange of a virtual photon	7
2.2	Running of the coupling constants	8
2.3	Gluon self coupling vertices	9
2.4	The one-dimensional Higgs potential	11
2.5	Direct top quark mass measurements performed by ATLAS and CMS	14
2.6	MSTW parton distribution function	14
2.7	Exemplary production mechanisms of single top quarks	16
2.8	Feynman diagrams for the leading order $t\bar{t}$ pair production mechanisms	17
2.9	Exemplary Feynman diagrams for next-to-leading order $t\bar{t}$ pair production	17
2.10	The dileptonic $t\bar{t}$ -decay	18
2.11	The lepton+jets $t\bar{t}$ -decay	19
2.12	The fully hadronic $t\bar{t}$ -decay	19
2.13	Measurements of $m_{\text{top}}^{\text{pole}}$ performed by ATLAS, CMS and DØ	20
3.1	The CERN accelerator complex	22
3.2	Pictures of a RF cavity and a dipole magnet	22
3.3	The ATLAS detector	24
3.4	The ATLAS magnet system	25
3.5	The ATLAS inner detector	25
3.6	The ATLAS calorimeter system	27
3.7	The ATLAS muon system	28
3.8	Stages of a proton-proton collision	31
5.1	Jet multiplicity, jet angular separation and $E_{\text{T}}^{\text{miss}}$ distributions	40
5.2	Kinematic distributions for jets	41
5.3	Kinematic distributions for $b$ -tagged jets	42
5.4	Kinematic distributions for leptons	43
6.1	Fits to the lepton $p_{\text{T}}$ distributions for $m_{\text{top}}^{\text{MC}} = 172.5$ GeV	46
6.2	Parameters of the Novosibirsk distribution as function of $m_{\text{top}}$	47
6.3	Template shapes for different values of $m_{\text{top}}$	47
6.4	Template fit to the 172.5 GeV signal MC distributions	48
6.5	Results of pseudo experiments	49
8.1	Comparison of the NNLO weighted to the unweighted lepton $p_{\text{T}}$ distributions	57
8.2	Results of pseudo experiments: NNLO reweighted	58
9.1	Template fit to the measured lepton transverse momentum distributions	59
9.2	Separate template fit to the measured lepton transverse momentum distributions	60

B.1	Jet multiplicity, jet angular separation and $E_T^{\text{miss}}$ distributions: $m_{\text{top}} = 167.5$ GeV	67
B.2	Kinematic distributions for jets: $m_{\text{top}} = 167.5$ GeV	68
B.3	Kinematic distributions for $b$ -tagged jets: $m_{\text{top}} = 167.5$ GeV	69
B.4	Kinematic distributions for leptons: $m_{\text{top}} = 167.5$ GeV	70
C.1	Fits to the electron $p_T$ distributions for different $m_{\text{top}}^{\text{MC}}$	72
C.2	Fits to the muon $p_T$ distributions for different $m_{\text{top}}^{\text{MC}}$	73
C.3	Fits to the electron $p_T$ distributions for different $m_{\text{top}}^{\text{MC}}$ : separate fit	74
C.4	Fits to the muon $p_T$ distributions for different $m_{\text{top}}^{\text{MC}}$ : separate fit	75
C.5	Parameters of the Novosibirsk distribution as function of $m_{\text{top}}$ : separate fit	76
C.6	Template fit to the 172.5 GeV signal MC distributions: separate fit	76
C.7	Results of pseudo experiments drawn from the template	77
E.1	Uncertainties on $m_{\text{top}}$ for different requirements on $\Delta R_{jj}$ and jet multiplicity	81
F.1	Results of pseudo experiments: NNLO up and down variations	83
F.2	Results of pseudo experiments: NNLO reweighted without $\Delta R_{jj}$ requirement	84
G.1	Likelihood distribution plotted as a function of $m_{\text{top}}$	85
G.2	Template fit to the measured lepton $p_T$ distributions	86
G.3	Template fit: no $p_T$ requirement on 5 <sup>th</sup> leading jet	87
G.4	Template fit: exactly 4 jets	87
G.5	Template fit: at least 2 $b$ -tagged jets	88
G.6	Template fit: $E_T^{\text{miss}} > 60$ GeV	88
G.7	Template fit: charge separated	89
G.8	Template fit: altered parametrisation	90
G.9	Template fit: varied fit ranges	91

## List of Tables

2.1	The fundamental particles of the Standard Model	4
2.2	Single top quark production cross sections for the LHC at $\sqrt{s} = 8$ TeV	15
2.3	Branching fractions for the $W$ boson	18
5.1	Event yields after final selection requirements	38
7.1	Summary of the uncertainties evaluated in the analysis	52
C.1	Template parameters	71
C.2	Separate template parameters	71
D.1	Breakdown of the lepton uncertainty	79
D.2	Breakdown of the jet energy resolution uncertainty	79
D.3	Breakdown of the jet energy scale uncertainty	80
E.1	Uncertainties on $m_{\text{top}}$ for different requirements on $\Delta R_{jj}$ and jet multiplicity	81
F.1	NNLO weighting factors and their up and down variations	83
G.1	$m_{\text{top}}$ results for different modifications of the event selection requirements	86



## Acknowledgement

I'd like to take the opportunity to thank all those people who have accompanied me so far!

In addition, I want to particularly name:

- my family, who has always supported me without hesitation
- my supervisor Prof. Dr. Otmar Biebel, who, despite not having any, took always the time to discuss and answer my questions
- Prof. Dr. Dorothee Schaile, for her continuous support

My special thanks go to my friends, powpow!